

BRNO UNIVERSITY OF TECHNOLOGY

VYSOKÉ UČENÍ TECHNICKÉ V BRNĚ

FACULTY OF MECHANICAL ENGINEERING

FAKULTA STROJNÍHO INŽENÝRSTVÍ

INSTITUTE OF PHYSICAL ENGINEERING

ÚSTAV FYZIKÁLNÍHO INŽENÝRSTVÍ

PLASMONICS OF NON-NOBLE METALS

PLAZMONIKA NEUŠLECHTILÝCH KOVŮ

MASTER'S THESIS

DIPLOMOVÁ PRÁCE

AUTHOR

Bc. Michael Foltýn

AUTOR PRÁCE

SUPERVISOR

Ing. Michal Horák, Ph.D.

VEDOUCÍ PRÁCE

BRNO 2024



Assignment Master's Thesis

Institut: Institute of Physical Engineering

Student: Bc. Michael Foltýn

Degree programm: Physical Engineering and Nanotechnology

Branch: no specialisation

Supervisor: Ing. Michal Horák, Ph.D.

Academic year: 2023/24

As provided for by the Act No. 111/98 Coll. on higher education institutions and the BUT Study and Examination Regulations, the director of the Institute hereby assigns the following topic of Master's Thesis:

Plasmonics of non-noble metals

Brief Description:

Traditional plasmonic materials are gold and silver. However, especially in the UV region, it is necessary to look for their possible alternatives, for example among non-noble metals.

Master's Thesis goals:

Explore the possibilities of non–noble metals (e.g. aluminium, bismuth, lead,...) in plasmonics. Prepare nanostructures from the selected material and characterize their functional properties in the field of plasmonics using analytical transmission electron microscopy.

Recommended bibliography:

HORÁK, Michal. Elektronová mikroskopie a spektroskopie v plazmonice. Brno, 2019. Dostupné také z: https://www.vutbr.cz/studenti/zav-prace/detail/122351. Dizertační práce. Vysoké učení technické v Brně Středoevropský technologický institut VUT. Vedoucí práce Tomáš Šikola.

SANZ, J. M.; ORTIZ, D.; ALCARAZ DE LA OSA, R.; SAIZ, J. M.; GONZÁLEZ, F. et al. UV Plasmonic Behavior of Various Metal Nanoparticles in the Near- and Far-Field Regimes: Geometry and Substrate Effects. The Journal of Physical Chemistry C. 2013, roč. 117, č. 38, s. 19606-19615. ISSN 1932-7447. Dostupné z: https://doi.org/10.1021/jp405773p.

MCMAHON, Jeffrey M.; SCHATZ, George C. a GRAY, Stephen K. Plasmonics in the ultraviolet with the poor metals Al, Ga, In, Sn, Tl, Pb, and Bi. Phys. Chem. Chem. Phys. 2013, roč. 15, č. 15, s. 5415-5423. ISSN 1463-9076. Dostupné z: https://doi.org/10.1039/C3CP43856B.

Deadline for submission Master's Thesis is gi	ven by the Schedule of the Academic year 2023/2
In Brno,	
	L. S.
prof. RNDr. Tomáš Šikola, CSc. Director of the Institute	doc. Ing. Jiří Hlinka, Ph.D. FME dean

Abstract

This master's thesis investigates the possibilities of non-noble metals in plasmonics. I have numerically calculated the expected plasmonic properties of various non-noble metals and based on the results chose bismuth as the material of focus. I fabricated bismuth plasmonic antennas by focused ion beam lithography of polycrystalline bismuth layers deposited by magnetron sputtering. Three types of plasmonic antennas have been fabricated, bar-shaped antennas with widths of 40 and 80 nm and bowtie antennas with a 20 nm wide gap between their wings. I analysed the plasmonic properties of the fabricated antennas by electron energy loss spectroscopy and found bismuth a good plasmonic material. Furthermore, bismuth proved to be a cost-effective alternative to gold, offering a broader range of usable wavelengths. Additionally, I synthesised monocrystalline bismuth nanoparticles by pyrolysis of bismuth acetate and tested various cleaning methods needed for removal of surfactant layers from their surface. I examined the plasmon resonances in the synthesised nanospheres and found an optimal method for collecting electron energy loss spectra of nanoparticles surrounded with thick layer of contaminants.

Key Words

bismuth, plasmonic antennas, nanoparticles, EELS

Abstrakt

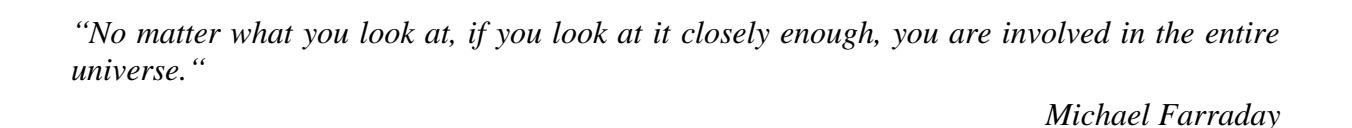
Tato diplomová práce se zabývá možnostmi použití neušlechtilých kovů v plazmonice. Provedl jsem numerické simulace plazmonických vlastností různých neušlechtilých kovů a na základě dosažených výsledků jsem za materiál studovaný v této práci zvolil bismut. Vyrobil jsem bismutové plazmonické antény za pomoci litografie fokusovaným iontovým svazkem z bismutových polykrystalických vrstev deponovaných magnetronovým naprašováním. Byly vyrobeny tři typy plazmonických antén, tyčinkovité anténky o šířkách 40 a 80 nm a antény typu bowtie s 20 nm širokou mezerou mezi křidélky antény. Studoval jsem plazmonové rezonance v těchto anténách za pomocí spektroskopie energiových ztrát elektronů a shledal jsem bismut dobrým plazmonickým materiálem, který má potenciál stát se levnější alternativou k doposud používanějšímu zlatu, která navíc nabízí širší interval použitelných vlnových délek. Dále jsem syntetizoval monokrystalické bismutové nanočástice za pomocí pyrolýzy octanu bismutitého a otestoval a porovnal různé čistící metody vyžadované pro odstranění vrstev surfaktantů z povrchu vyrobených nanočástic. Studoval jsem plazmonové rezonance těchto nanočástic a našel metodu pro měření energiových ztrát elektronů z nanočástic obklopených tlustou vrstvou kontaminantů.

Klíčová slova

bismut, plazmonické antény, nanočástice, EELS

FOLTÝN, Michael. *Plasmonics of non-noble metals*. Brno, 2024. Available also at: https://www.vut.cz/studenti/zav-prace/detail/158023. Master's Thesis. Brno University of Technology, Faculty of Mechanical Engineering, Institute of Physical Engineering. Supervisor Ing. Michal Horák, Ph.D.





My sincere thanks belong to Ing. Michal Horák, Ph.D. for the 4 years long guidance as well as the time and care he has invested in me. His extensive knowledge and experience, generously shared with me, along with his unconventional ideas, have been among the most valuable assets I've gained during my studies. I'm thankful for the welcoming and friendly atmosphere during our collaboration and for the patient tutoring on operating transmission electron microscopes. I would also like to thank him for the EELS analysis of the nanostructures fabricated in this thesis, which allowed me to explore the plasmonic properties of bismuth.

I would like to acknowledge and thank Ing. Jan Prášek, Ph.D. for his instructions and assistance during the deposition of bismuth layers. My thanks also belong to Bc. Marek Patočka for the AFM analysis of the deposited bismuth layer and to RNDr. Ivana Pilátová, CSc. for the provision of the magnetic stirring hotplate used for the syntheses of bismuth nanoparticles.

I would further like to thank my dearest friends Jakub Urban and Štěpán Pikna for the support and enjoyable time spent during the shared 13 years of studying together. It has been an unforgettable experience and a source of many fond and wacky memories.

Most importantly, I am grateful to my family and girlfriend. I could finish my master's studies only thanks to the support and encouragement they have provided me. Special thanks belong to my mother, who has been the only relative willing to listen to the mundane electron microscopy-related knowledge dropped by me whenever possible.

CzechNanoLab project LM2023051 funded by MEYS CR is gratefully acknowledged for the financial support of the measurements/sample fabrication at CEITEC Nano Research Infrastructure.

Contents

1	Intro	troduction				
2	Plasi	nonic antennas	15			
	2.1	Surface plasmon polaritons	15			
	2.2	Localised surface plasmons and their characterisation	16			
	2.3	Analytical scanning transmission electron microscopy	17			
	2.4	Fabrication of plasmonic antennas	20			
	2.5	FIB lithography of plasmonic antennas	22			
	2.6	Chemical synthesis of plasmonic antennas	24			
	2.7	Suitable non-noble plasmonic materials	26			
	2.8	Plasmon resonances in bismuth antennas	27			
3	Bism	nuth	30			
	3.1	Introduction to bismuth	30			
	3.1.1	Bulk bismuth	30			
	3.1.2	Bismuth polycrystalline layers	31			
	3.1.3	Bismuth nanoparticles	32			
	3.2	Fabrication of bismuth plasmonic antennas	33			
	3.2.1	Deposition and structural analysis of the bismuth layer	33			
	3.2.2	Ion beam lithography of plasmonic antennas	40			
	3.2.3	Thickness of the bismuth antennas from EELS	44			
	3.3	Plasmonic properties of fabricated bismuth antennas	45			
	3.3.1	Plasmonic properties of 40 nm bar antennas	46			
	3.3.2	Plasmonic properties of 80 nm bar antennas	49			
	3.3.3	Plasmonic properties of bowtie antennas	52			
	3.3.4	Comparison of bismuth and gold bowtie antennas	55			
	3.3.5	Influence of temperature on plasmon resonances in bismuth	57			
	3.4	Preparation of bismuth nanoparticles	58			
	3.4.1	Chemical synthesis	58			
	3.4.2	Removal of ligands	63			
	3.5	Plasmonic properties of bismuth nanospheres	66			
4	Conc	clusion	71			
R	eference	es	73			
т	C - 1-	Lucyications	02			

1 Introduction

Plasmonics is a field of science studying the surface plasmon polaritons and localised surface plasmons. The surface plasmon polariton is an electromagnetic wave propagating along an infinite metal-dielectric interface. These evanescent waves can be excited through the interaction of an incident electromagnetic wave with the free electrons in the metal, resulting in induced oscillations of the free electron gas. However, if the boundary is of finite character, the surface polaritons can be reflected at the edge of the interface thus forming standing waves called localised surface plasmons. Any metallic nanoparticle surrounded by a non-conductive medium can be considered as a finite metal-dielectric interface. These plasmonically active metallic nanoparticles are in their behaviour not that different from the common macroscopic radio antennas. For this reason, we call the metallic nanoparticles plasmonic antennas. The plasmonic antennas allow the enhancement and confinement of the local electromagnetic field, even below the diffraction limit [1]. These unmatched properties are the reason behind the rich applications of metallic nanoparticles in optics, communication technologies and medicine [2], [3].

Plasmonic antennas can be fabricated in numerous ways. The two most common fabrication techniques are the chemical synthesis of free-standing metallic nanoparticles and the fabrication of plasmonic antennas by a lithography of a metal layer deposited on a substrate. While the first approach is prevalent in medical applications, the second approach is more fitting for optical applications. The fabricated antennas can be characterised for example by transmission electron microscopy and their plasmonic behaviour can be analysed by electron energy loss spectroscopy. This spectroscopic technique is based on measuring the energy loss of electrons transmitted through the sample. These energy losses correspond to various excitations in the sample, among these, the localised surface plasmons.

This work freely follows on from the preceding rigorous research in the field of plasmonics carried out at the Institute of Physical Engineering FME BUT. At the institute, the plasmonic material of focus had for years been gold. The gold plasmonic antennas and the influence of the used fabrication method have been studied by electron energy loss spectroscopy (EELS) and cathodoluminescence [4]. EELS has been the primary tool for studying the impact of the lithographic method on the plasmonic properties of fabricated antennas [5]. This work was soon followed by a study focused on the crystallinity of gold plasmonic antennas and the influence of their morphology on their plasmonic performance [6]. Further on, the dependence of the field enhancement on the antenna shape has been thoroughly examined as well [7], [8]. Although gold proved to be an ideal plasmonic material, the damping of plasmon resonances in gold antennas at higher energies related to intraband transitions, along with gold's relatively higher price led to a search for other suitable plasmonic materials, such as silver and non-noble metals aluminium and gallium [9], [10], [11]. The promising results further encouraged us to delve deeper into the plasmonics of non-noble metals.

The objectives of this master's thesis are to explore the possibilities of non-noble metals in plasmonics, to prepare nanostructures from the selected material and to characterise the functional properties of the fabricated nanostructures by analytical transmission electron microscopy.

In Chapter 2, an introductory overview of plasmonics is followed by a discussion of the fabrication and characterisation techniques employed in preparation and analysis of plasmonic antennas. Further on, an assessment regarding the applicability of different non-noble metals

for plasmonic purposes is made, culminating in the selection of bismuth as the primary material of investigation in this study. Additionally, the chapter includes a numerical analysis of the plasmon resonant modes expected in bismuth antennas.

Chapter 3 is dedicated to bismuth. First, the physical properties of bismuth in the form of bulk material, thin polycrystalline layers and monocrystalline nanoparticles are explored and from the findings, recommendations for the fabrication are drawn. In Section 3.2, the fabrication of bismuth plasmonic antennas by focused-ion-beam lithography out of bismuth polycrystalline thin films deposited by magnetron sputtering is described and evaluated. Section 3.3 describes the plasmonic properties of fabricated antennas analysed by EELS. The chemical syntheses of monocrystalline bismuth nanoparticles and the process of cleaning the nanoparticle solutions are both described in Section 3.4. The plasmonic properties of fabricated and cleaned bismuth nanoparticles are then studied by EELS in Section 3.5.

2 Plasmonic antennas

Plasmonics is a field of science focusing on the light-metal interactions. Although such interactions have been used for centuries [12], the principles of these historical applications as well as a multitude of promising new ones have been discovered only recently with the introduction of new analytical techniques and advances in this field [13]. Surface plasmon polaritons (SPP), the main subject of interest in plasmonics, is a quasiparticle coupling the oscillations of free electron gas to the electromagnetic wave bound to the metal-dielectric interface [14].

2.1 Surface plasmon polaritons

The interaction between a metal-dielectric interface and an incoming electromagnetic wave is governed by the Maxwell equations

$$\nabla \cdot \vec{D} = \rho_{\text{ext}} \,, \tag{2.1}$$

$$\nabla \cdot \vec{B} = 0 \,, \tag{2.2}$$

$$\nabla \times \vec{E} = -\frac{\partial \vec{B}}{\partial t} \,, \tag{2.3}$$

$$\nabla \times \vec{H} = \vec{J}_{\text{ext}} - \frac{\partial \vec{D}}{\partial t}, \qquad (2.4)$$

where the electric displacement \vec{D} and electric field \vec{E} characterize the electric part of the macroscopic field while the magnetic field \vec{H} and magnetic induction \vec{B} describe the magnetic part of the macroscopic field. $\rho_{\rm ext}$ marks the external charge density and $\vec{J}_{\rm ext}$ marks the external current density. A solution of the Maxwell equations for the metal-dielectric interface is found in the form of a transverse magnetic (TM) wave propagating along the interface. Such wave has a non-zero component of magnetic field $H_{\rm y}$ and non-zero components of electric field $E_{\rm x}$ and $E_{\rm z}$. Such a wave is then described as

$$\vec{H} = (0, H_y, 0) = (0, A, 0)e^{ik_x x}e^{-k_z^{d,m}z},$$
 (2.5)

$$\vec{E} = (E_{x}, 0, E_{z}) = (iAk_{z}^{d,m}, 0, -Ak_{x}) \frac{1}{\varepsilon_{0}\varepsilon_{r}} e^{ik_{x}x} e^{-k_{z}^{d,m}z},$$
 (2.6)

where A is the wave amplitude obtained from initial conditions, $(k_z^{d,m})^2 = k_x^2 - \frac{\omega}{c} \varepsilon_r$, with the relative permittivity in the volume of the dielectric being $\varepsilon_r = \varepsilon_d$ and in the case of metal $\varepsilon_r = \varepsilon_m$. The component of a wave vector parallel to the x-axis, k_x , can then be described as

$$k_{x} = \frac{\omega}{c} \sqrt{\frac{\varepsilon_{\rm m} \varepsilon_{d}}{\varepsilon_{\rm m} + \varepsilon_{d}}},\tag{2.7}$$

which is the dispersion relation of the propagating wave called SPP, tied to the oscillations of free electron gas. The equation describing SPP tells us that the wave is damped exponentially with the increasing distance from the interface in both dielectric and metal. A simplified diagram of the SPP propagating along the dielectric is shown in Figure 1. Although this theoretical foundation of plasmonics is extremely brief, it covers the cornerstone of plasmonics. More detailed information regarding the theory of plasmonics can be found for example in References [4], [14], [15].

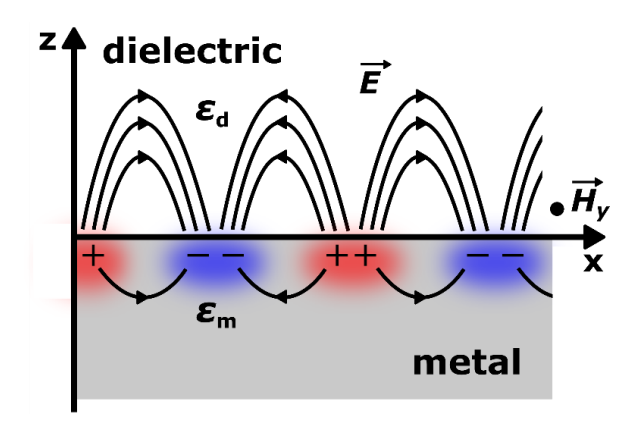


Figure 1: Schema of a SPP propagating along the metal-dielectric interface. The non-zero component of magnetic field H_y is perpendicular to non-zero components of electric field E_x and E_z . The SPP penetrates deeper into the dielectric, which is a crucial characteristic used in sensing applications. The figure has been taken and modified from [4].

2.2 Localised surface plasmons and their characterisation

When the metal-dielectric interface supporting SPPs is limited in size (as in the case of metallic nanoparticles), the SPPs are reflected at the end of the interface and lead to the creation of localised surface plasmons. These LSP resonances can enhance the electric field in the vicinity of the surface. Due to this enhancement of the electric field, the nanoparticle supporting the LSP is then called a plasmonic antenna. More detailed information regarding the field enhancement as well as the nature and properties of LSPs can be found for example in [16], [17].

The plasmonic properties of antennas can be analysed by optical and electron microscopies and spectroscopies. One of the oldest and simplest techniques is optical spectroscopy, where the spectra of transmitted and reflected light are recorded and analysed [18], [19]. For its ability to study both the intensity and phase of the electromagnetic field in the vicinity of the antenna, coherent holographic microscopy is frequently employed to analyse the influence of antennas on the incident light [20], [21], [22]. To study individual antennas and their plasmon resonances, dark-field optical microscopy and spectroscopy can be employed as well [23]. We can also characterise plasmonic antennas by scanning near-field optical microscopy (SNOM). For the detection of a near field in the visible region of spectra, a tip fabricated from an optical fibre with an aperture covered by a metallic layer is used. Such a technique is then called aperture SNOM (a-SNOM for short) [24]. Similarly, a method based on the scattering from a simple aperture-less tip can be utilised as well. This technique is called s-SNOM (scattering SNOM). To further enhance the near field of studied antennas, the s-SNOM tip is frequently patterned with nanostructures [25]. Further information regarding these two experimental techniques is available in [26].

One of the tools for characterisation of plasmonic antennas is scanning transmission electron microscopy (STEM) and various analytical techniques tied to it. When the beam of swift electrons passes through the sample, the energy of electrons is lost. These energy losses are caused by interactions with the sample and are tied to various excitation mechanisms, among these also localised surface plasmons. The technique based on measuring these energy losses of the primary electron beam is called electron energy loss spectroscopy (EELS). EELS allows measuring the energy of each individual mode of plasmon resonances with an accuracy below 100 meV while maintaining the spatial resolution in the range of units of nanometres. Another method suitable for the characterisation of plasmonic antennas in STEM is cathodoluminescence, which is based on collecting photons emitted from the sample after the impact of the electrons. This spectroscopic method enables us to measure the energy of plasmonic resonant modes with a resolution of around 10 meV [4], [27]. However, for the characterisation of plasmonic antennas by STEM-related techniques, it is necessary that the nanostructures are fabricated on thin membranes.

The diffraction-limited spatial resolution of far-field optical microscopy and spectroscopy allows the characterisation of large ensembles of plasmonic antennas. The weakness in the form of limited spatial resolution is outweighed by high spectral resolution, which can reach units of milli-electron volts [28]. SNOM-related techniques overcome the diffraction limit, offering a spatial resolution of around 3–20 nm [29]. Although the spectral resolution of STEM EELS is not as high as in the case of optical spectroscopies, it is outweighed by its superior spatial resolution below 1 nm. Further on, EELS allows to measure the thickness of an analysed plasmonic antenna. The accuracy of such a method is conditioned by using a correct inelastic mean free path of electrons in the sample. STEM also allows to determine the chemical composition of individual nanostructures with the analysis of characteristic X-rays created through the interaction of primary electrons with the electron shells of atoms [30]. For these reasons, I choose analytical transmission electron microscopy as the main tool for the characterisation of nanostructures and their plasmonic properties.

2.3 Analytical scanning transmission electron microscopy

In STEM, the convergent electron beam scans over an imaged area of the sample point by point. As the beam of electrons passes through the sample, some of the electrons get scattered, either elastically or inelastically. The transmitted electrons are then collected by a semiconductor detector, or a camera and the transmitted signal is integrated and assigned to the corresponding beam position on the sample.

The contrast in the formed image comes from various contributions (all related to scattering) and can be distinguished based on its origin. The diffraction contrast arises from collecting the primary beam (containing unscattered electrons) and diffracted beams. The diffraction contrast gives qualitative information about the crystallography of the sample and is useful for imaging grains, lattice defects and grain boundaries [30]. The material contrast (also called Z-contrast) is based on the Rutherford elastic scattering of beam electrons on atomic nuclei. The Rutherford scattering cross-section is proportional to the square of the atomic number of the scattering atom. Therefore, the material contrast is quantitative and is the cornerstone of advanced STEM techniques, such as atom-counting [31]. Besides these two main sources of contrast in STEM imaging, there are also other contributions from the variations in sample thickness, inelastically scattered electrons and other factors.

By changing the camera length of the microscope projection system, the collection angle of the detector or camera changes. This allows us to select the main source of contrast and collect different signals. The schematic depiction of STEM detectors and their geometry is in Figure 2. The three most commonly collected signals are the bright-field (BF), annular dark-field (ADF) and high-angle annular dark-field (HAADF). The BF and ADF signals contain diffraction contrast and thickness contrast. These are characteristic with lower scattering semi-angles, usually below 50 mrad [32], [33]. The HAADF signal contains primarily material contrast and contrast from the variations of sample thickness. Since it is free of the diffraction contrast, the HAADF signal is used for an accurate determination of the dimensions and shape of structures and features in the sample.

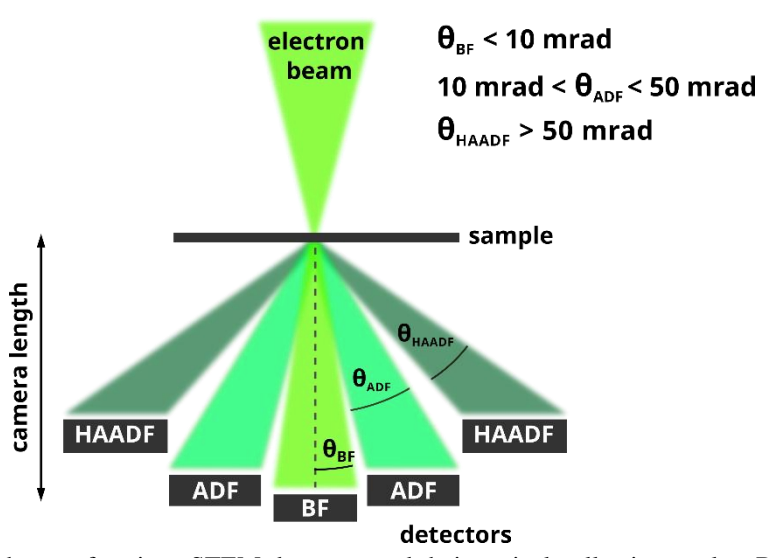


Figure 2: A simplified schema of various STEM detectors and their typical collection angles. By changing the camera length of the microscope projection system (originally a distance of the detector from the sample), the collection angles of the detectors can be changed and with it, the collected signal. For example, by increasing the camera length, the edges of the signal originally collected by BF detector overlap to the ADF detector, giving rise to a Z-contrast dependent linearly on the atomic number of the material. Such signal collected by the ADF detector is then called annular bright-field (ABF). Adapted from [33].

During the inelastic scattering, some of the electron's energy is transferred to an inner-shell electron in the atom. If the transferred energy is sufficiently high, the inner-shell electron can be ejected either into a vacuum or into an unoccupied state above the Fermi level. The empty state in the inner-shell can be filled by an electron from an outer-shell, with the simultaneous emission of characteristic photons with the energy equal to the energy difference of the inner- and outer-shell. Such emitted X-ray photon is characteristic for the material atom and can be collected by a semiconductor detector placed above or below the sample. The collected photon creates electron-hole pairs inside the semiconducting region of the detector. The number of created electron-hole pairs depends on the photon's energy. By counting these pairs, the energy of the characteristic photon is identified. This analytical technique is called energy dispersive X-ray spectroscopy (EDX) [34]. Collection of the characteristic X-rays emitted during scanning of an electron beam over the sample allows for a quantitative analysis of the elemental composition inside the sample [35].

The transmitted electron's energy lost in an inelastic scattering event can be measured by a spectroscope containing a magnetic prism. The magnetic force disperses the electrons travelling through the prism based on their energy. The dispersed electrons are then detected by a scintillator coupled to a camera and an electron energy loss (EEL) spectrum is recorded.

The simplified schema of the EEL spectroscope is in Figure 3. The EEL spectrum is dominated by the zero-loss-peak (ZLP) corresponding to the intensity of inelastically unscattered electrons. In the low-loss region of the EEL spectra, energy losses connected with the excitations of both bulk and surface phonons and plasmons, as well as the band transition and relativistic effects are present and can be observed (if the energy resolution determined by full-width-half-maximum of ZLP is sufficiently low). Therefore, low-loss EELS gives information about the response of the material to the incoming electromagnetic wave and through the Kramers-Kronig analysis a dielectric function of the material can be extracted as well. In the core-loss region of the EEL spectra, energy losses corresponding to excitations of inner-shell electrons are present in the form of so-called absorption edges or material edges. These energy losses are specific for each different material. The material edges also contain energy-loss-near-edge-structure (ELNES) which are characterised by minor intensity fluctuations around the edge energy and correspond to the oxidation states of the excited electrons. Therefore, core-loss EELS not only allows the quantitative chemical analysis of the sample but can also be used for the determination of the chemical bonds between atoms. A more detailed description of EELS can be found in [30], [36], [37], [38].

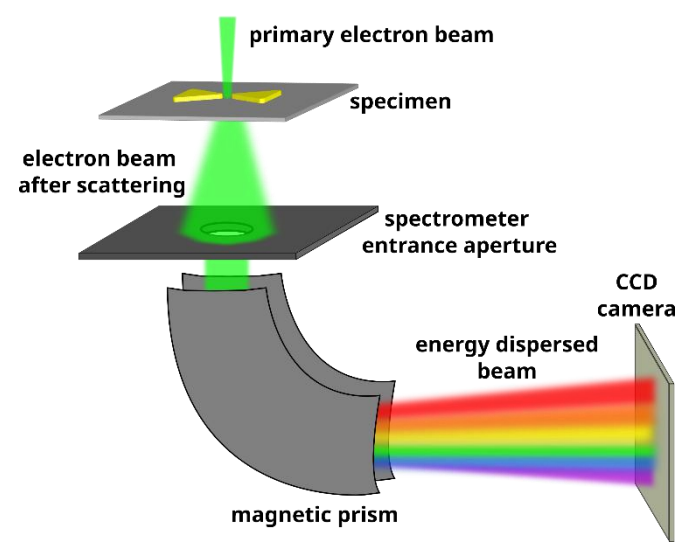


Figure 3: A simplified schema of an image filter used as a spectrometer in STEM. The spectrometer entrance aperture defines the collection angle of the spectrometer and with it, the collected signal. The transmitted beam is dispersed by a magnetic prism and the energy loss spectrum is recorded by a CCD camera. Adapted from [4].

Since the inelastic scattering is governed by a Poisson statistic, a relative thickness of the sample can be extracted from the EEL spectrum [4], [30]. The ZLP intensity corresponds to the intensity of electrons which did not undergo an inelastic scattering when passing through the sample with a thickness *t*. The relative thickness can then be calculated as

$$\frac{t}{\lambda_{IMFP}} = \ln \frac{I_{\text{total}}}{I_{\text{ZLP}}},\tag{2.8}$$

where $I_{\rm ZLP}$ is the intensity of ZLP, the $I_{\rm total}$ is the total intensity of transmitted electrons and $\lambda_{\rm IMFP}$ is the inelastic mean free path of an electron in the sample material. If a correct $\lambda_{\rm IMFP}$ is known, we can calculate the absolute thickness t of the sample and even create a thickness map of the analysed area. The determination of thickness can be useful when evaluating the morphology of fabricated nanostructures.

2.4 Fabrication of plasmonic antennas

The plasmonic properties of any plasmonic antenna depend on a number of factors. One of the predominant factors is the method used for the fabrication of the antennas. The two most common methods used for the fabrication of plasmonic antennas out of thin metallic layers are the electron beam lithography (EBL) and focused ion beam lithography (FIB lithography).

The EBL fabrication consists of spin coating the sample with electron-sensitive resist, patterning the resist by an electron beam, development, and removal of residual resist from the sample's surface. Although the EBL method offers a reliable way of producing large amounts of plasmonic antenna arrays, it is relatively time-consuming and the different behaviour of each resist after the electron beam exposure requires fine-tuning of the recipe for each different set of materials [39]. EBL fabrication may also lead to the contamination of samples by chemical compounds and solvents used during the development and removal of resist. For these reasons, I will not use the EBL lithography approach in this work.

The FIB lithography has exactly the opposite characteristics. Compared to EBL lithography, it is a straightforward method with the downside of a small fabrication throughput. In FIB lithography, the desired nanostructures are created by the removal of surface material from a certain area by ion bombardment. Fabrication by FIB lithography results in an unwanted modification of the sample, such as ion implantation, amorphization, and other undesired effects.

Both methods allow the fabrication of various types of nanostructures with dimensions below 10 nm. The influence of used fabrication method on the plasmonic properties of fabricated nanostructures has been studied and evaluated here [5]. Individual steps of both fabrication methods can be seen in Figure 4. Although the FIB lithography is quite straightforward, it is necessary to find an optimised milling strategy and beam setup for each individual material and desired structure.

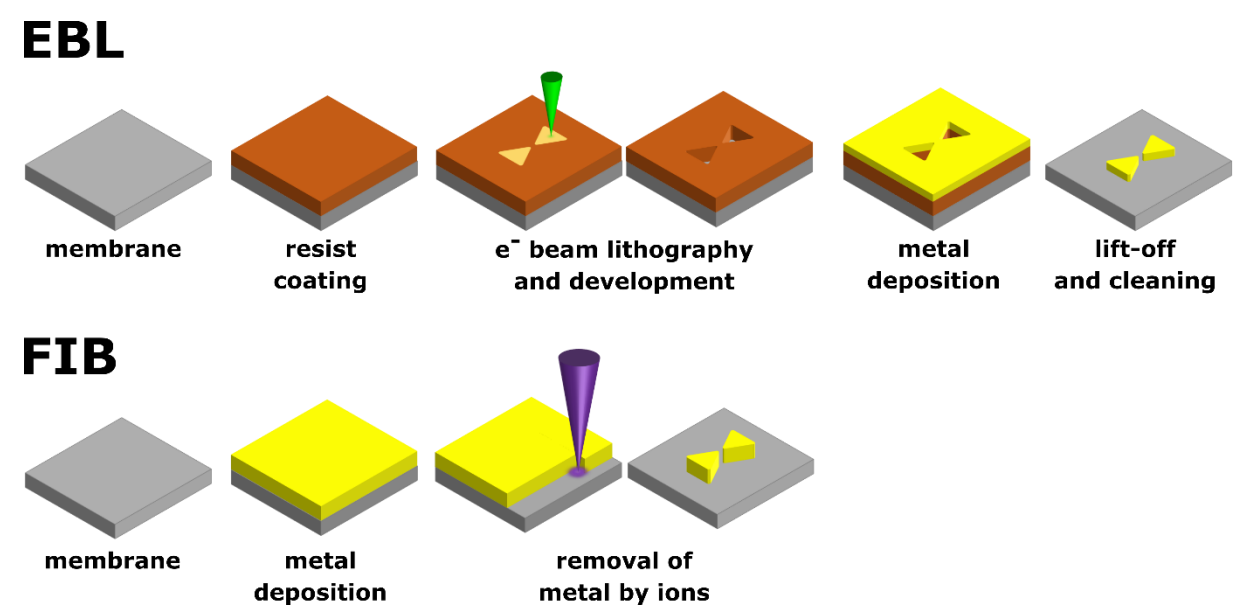


Figure 4: Simplified schema of EBL and FIB methods used for fabrication of plasmonic antennas. Clearly, the FIB lithography requires fewer steps compared to EBL. On the other hand, EBL fabrication yields higher fabrication throughput.

Besides the two lithographic methods, a large variety of other approaches can be used when fabricating metallic nanoparticles for applications in plasmonics. All of them can be divided into two categories based on the principle of creating the nanoparticles. These are the top-down and bottom-up methods [40]. Both approaches are schematically visualized in Figure 5. In the top-down methods, the bulk material is broken down into individual nanoparticles. In contrast, during the bottom-up approach, the nanoparticles are formed from individual atoms or ions, most frequently through the reduction of metal-organic reactants [41].

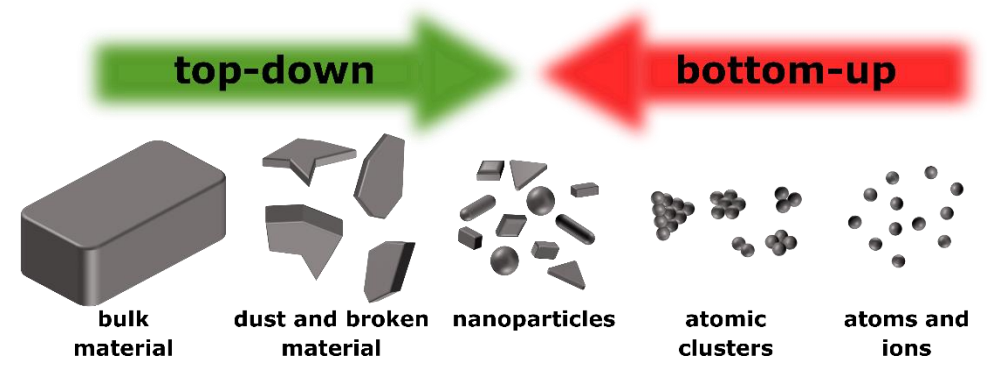


Figure 5: Schematic depiction of two approaches for fabrication of nanoparticles. The top-down method relies on destructive methods like laser ablation, mechanical grinding, or etching. Bottom-up methods are based mostly on chemical reduction, molecular condensation, and pyrolysis.

The most frequently used top-down methods are mechanical milling, laser ablation and PVD (physical vapour deposition) methods, such as sputtering or evaporation onto liquid substrates. The main advantage of the mechanical milling or grinding method is its simplicity, reliability, and versatility, as it allows the fabrication of nanoparticles of nearly any material. It is based on mechanical breakage of material through friction and abrasion by grinding objects, most often balls or sand. The heat and pressures connected with the friction of the grinding balls lead to an alternation of material through defects, creation of intermetallic phases and frequent elimination of ordered crystal lattice. Various setups for mechanical milling and a more detailed study of its properties can be found in [42], [43]. A similarly versatile top-down method is laser ablation. It is based on the ablation of the target material immersed in liquid media by laser pulses followed by the coalescence of individual atoms into clusters and nanoparticles. It is easily reproducible, reliable, and clean method that ensures the highly uniform size of created nanoparticles. The only disadvantages are the low fabrication throughput limiting the use of this method in industrial applications, and the high cost of the pulsed laser sources. A more detailed review of laser ablation and its applications can be found in [44], [45]. Nanoparticles fabricated by PVD deposition onto a liquid substrate are also uniform in size, and usually not contaminated by foreign reagents. The main disadvantage of these PVD methods is the inability to fabricate nanoparticles of alloys and multiphase materials [46]. All described top-down methods share the downside of difficult control over the final shape of created nanoparticles.

On the contrary, the bottom-up methods, usually based on wet chemical syntheses, allow synthesising nanoparticles with exact shapes and sizes. For this reason, the bottom-up approaches are preferred for the fabrication of nanoparticles used as plasmonic antennas. These techniques are usually based on the chemical reduction of precursors or their decomposition through the breakage of chemical bonds by an outside energy source [41]. The disadvantage of these chemical syntheses is their sensitivity to foreign contaminants introduced during the synthesis. Further on, various conditions during the synthesis can have severe impacts on the

synthesised nanoparticles. For these reasons, chemical syntheses are highly time-consuming and require tuning of the synthesis conditions. Fortunately, the control over the size of fabricated nanoparticles compensates for these difficulties.

Within this work, I use chemical synthesis to fabricate monocrystalline metallic nanoparticles. I also employ the FIB lithography to fabricate polycrystalline plasmonic antennas out of thin metallic layers.

2.5 FIB lithography of plasmonic antennas

For the fabrication of plasmonic antennas by the FIB lithography, achieving the smallest diameter of the ion beam is imperative for obtaining the highest resolution needed for the fabrication of uniform, precisely shaped antennas. To achieve the smallest beam diameter possible, the highest energy of ions and the lowest possible beam currents are used. The high ion energy is beneficial for eliminating the ion implantation inside the sample because ions with higher energy have a lower interaction cross-section. Luckily, during FIB lithography of thin layers, the ions get implanted primarily in the membrane or substrate material, as the usual depth of ion implantation is in the order of tens of nanometres [47]. On the other hand, higher ion beam energy leads to increased knock-on damage of the sample and increased thickness of the amorphized layer on top of the sample. Lowering the beam energy not only lowers the resolution but also leads to lower sputter yield (number of removed atoms per incoming ion), consequently slowing down the entire milling process. The sputter yield does not increase with higher beam energy interminably. Instead, the sputter yield of most materials culminates for a beam energy of approximately 30 keV, and for higher energies starts to decrease again [48]. The sputter yield depends on the ions used for the lithography (most frequently used ions are Ga, Ar, Xe, Ne, and He), ion energy, impact angle of the incoming ions and most importantly, the material being removed.

Sputter yield is the decisive parameter if the fabrication will be successful or not. For example, on a sample with a thin metallic layer on a thin membrane, which has a higher sputter yield than the metal layer itself, the lithography will most likely fail. The reason is, that during the removal of the top metallic layer, some areas of the layer will get removed (membrane will be uncovered), while other areas will remain covered with the metal layer. Due to the higher sputter yield of the membrane, the areas with the membrane visible will get sputtered away faster than the residual metal in other areas. Consequently, instead of a clean membrane with a metallic structure in the middle, we will end up with a perforated area with residual metal spots. A typical example of a sample where FIB lithography will fail is an aluminium layer on a thin SiN_x membrane. For this reason, it is important to consider beforehand, whether the material has a higher sputter yield, than the thin membrane. Just in such a case, it will be possible to fabricate nanostructures out of this material. Interestingly, the sputter yield is connected to the melting temperature of the material. Materials with low melting temperatures have usually higher sputter yield. The graph of sputter yields for various elements is in Figure 6. A simple calculator of sputter yield for different materials, impacting ions and their energies can be found in [49].

The sputter yield also affects the amount of redeposition. The higher the sputter yield, the faster the milling process will be, thus lowering the amount of redeposited material. In some cases, the redeposition can regenerate fabricated antennas and even the irregularities of the antenna's shape out. However, the redeposited material contains a larger number of implanted ions, and its structure is completely different from the original layer [50]. The best way of reducing

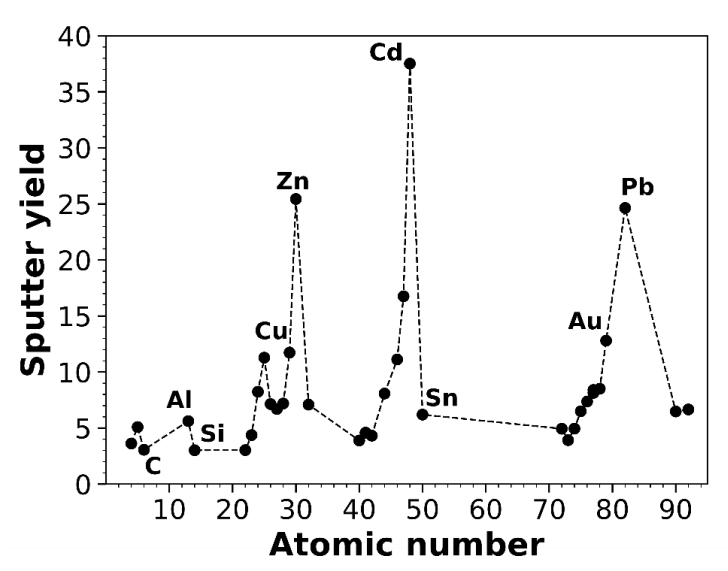


Figure 6: Sputter yield (number of removed atoms per incoming ion) of various materials for bombardment by Ga ions with the energy of 30 keV. Various common elements are marked for easier comprehension. The sputter yields were calculated by Simple Sputter Yield Calculator [49].

excessive redeposition is through the optimisation of milling strategy, dwell time and number of passes. The milling strategy defines in which fashion the ion beam passes over the area, whether in serpentine, raster, or other mode. The dwell time is the time for which the FIB mills one point and is usually tied to the number of passes of the ion beam over the milled area. Longer dwell times lead to an increased redeposition. Unfortunately, there are no optimal parameters that would suit all materials. Therefore, a thorough testing of optimal parameters for each different material, sample setup and fabricated structure is needed.

The usage of different ions can significantly affect the fabrication results as well. Using lighter ions, such as neon ions allows better resolution leading to more precisely fabricated structures. On the other hand, the sputter yield for lighter ions is lower, and the implantation of noble gas ions can lead to the creation of blisters and gas pockets inside the sample. For this reason, fabrication by such noble gas ions usually requires subsequent annealing to allow the gas to escape [51]. The implanted ions can also alter the sample through the creation of new metallic phases or altering the physical properties of the sample material. In the case of lithography by gallium ions, damaging the sample by the so-called liquid metal embrittlement (LME) is a common phenomenon. The LME is based on the weakening of solid metal bonds by adsorbed liquid metal atoms. The occurrence of LME is usually conditioned by the presence of strain or tensile stress. One of the exceptions to this rule is the aluminium, which undergoes the LME immediately as the gallium ions are introduced. The results of the fabrication of antennas from the aluminium layer can be seen in Figure 7. More information regarding the liquid metal embrittlement induced by gallium bombardment can be found in [52]. To verify whether the sample will be altered by the creation of metallic phases, it is essential to find and examine the corresponding binary phase diagram.

To achieve the best antennas, the following steps should be taken. First, it is necessary to verify that the layer material has a higher sputter yield than the substrate layer. The next step is to study the binary phase diagram of the element of the FIB and the layer material, to ensure that no significant changes in the layer material will appear during the lithography. For the lithography itself, the highest ion beam energy and lowest beam currents should be used, to

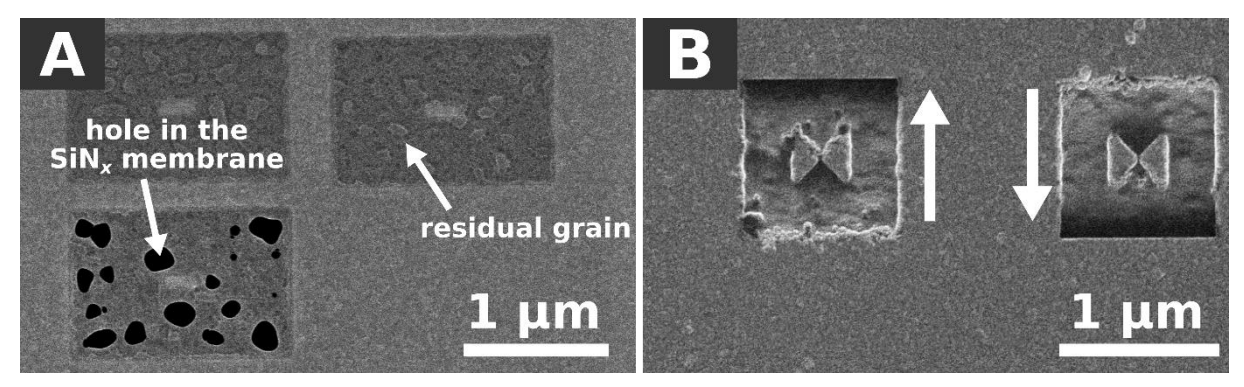


Figure 7: SEM micrographs of aluminium structures fabricated by Ga FIB. **A:** Structures fabricated with two passes of the beam over the milled area. The higher sputter yield of the supporting SiN_x membrane and low sputter yield of the aluminium lead to the creation of holes in the membrane before the residual aluminium grains can be removed. Further on, the low sputter yield of aluminium leads to a longer total milling time and results in a lower quality of fabricated structures and higher redeposition rates. **B:** Redeposition of aluminium is mostly visible in the part of the milled area, where the beam was starting. The arrows mark the direction in which the ion beam rastered horizontally over the milled area. Structures were fabricated with one pass of the ion beam over the milled area. By comparing structures in panels A and B, it is apparent that a higher number of passes (leading to lower dwell time) limits the redeposition.

achieve the highest resolution possible. The dwell time should be lowered by using more than one passing of the ion beam over the milled area. The number of passes should be kept low, to allow the regeneration of antennas by a slight redeposition and to obtain a smoother surface in the milled area. The exact number of passes and milling strategy should be tested for each material. If possible, different ion beams can be used. The most sophisticated practice is to pre-mill the area with gallium ions and finish the structures with Ne or He ions for sharper edges of fabricated antennas and finer details. More information regarding the optimal ion beam setup for the fabrication of plasmonic antennas, along with the description of the parameter optimization can be found in [53].

2.6 Chemical synthesis of plasmonic antennas

Three basic components are required for the chemical fabrication of nanoparticles. The precursor, which is the source of the desired material atoms or ions, the reduction agent or energy used for splitting the precursor, and the surfactant or capping agent limiting the coalescence and excessive clustering of synthesised nanoparticles. The precursors are usually inorganic metal salts, acetates, or more complex metal-alkyls. The choice of the precursor and its redox potential (proportional to its reactivity) affects the size and shape of synthesised nanoparticles. The more reactive the precursor, the faster the synthesis, leading to smaller synthesised nanoparticles [46].

A similar relation applies to the reducing agents. The most frequently used reducing agents are the sodium tetrahydridoborate (NaBH₄), sodium citrate, and ascorbic acid. The concentration and method of adding the reduction agent into the solution both affect the reaction kinetics and the final shape and size of nanoparticles. Strong reduction agents are required for synthesising small and symmetrical nanoparticles, used as seeds during the fabrication of core-shell nanoparticles. On the contrary, for fabricating larger nanoparticles with an anisotropic shape, weak reducing agents are used [41]. Once the precursor is broken down either through absorbed energy or through a chemical reduction, the now loose metal atoms or ions form atomic clusters by atomic addition and first nanoparticles begin to form. These would continue to grow in size through further aggregation and Ostwald ripening. If such process was not stopped or at least

controlled, the nanoparticles would aggregate and form microparticles in the form of precipitated sediment at the bottom of the reaction vessel.

To stop the aggregation of nanoparticles, surfactants are added to the solution. Most frequently used surfactants are long polymer chains, such as polyvinylpyrrolidone (PVP), (poly)ethylene glycols, oleic acid, or stearates. Surfactants cover the surface of metallic clusters and nanoparticles, thus preventing any further coalescence. The surfactants are adsorbed on the nanoparticle surface through various mechanisms, such as covalent bonding, simple Coulomb interaction between polar molecules, or steric effect, based on the hydrophobic nature of the used surfactant [54], [55]. The surfactant is arguably the most important factor determining the resulting shape and size of nanoparticles. For example, through the preferential adsorption of ionic surfactants on certain crystal orientations, large nanotriangles can be formed. Similarly, hydrophobic surfactants in aqueous solutions tend to form long nanoribbons. The size of the surfactant molecule, proportional to its molecular weight, affects the adsorption mechanism too. For example, longer PVP chains tend to be adsorbed through the steric effect and form a thick amorphous multilayer around the nanoparticle. Shorter PVP chains with lower molecular weight are used for controlling the nanoparticle shape, as they adsorb primarily on preferential crystal orientation. Unfortunately, the shorter PVP chains form a thinner surface layer, resulting in a lower stability of the nanoparticle solution over time. Further on, the concentration of surfactant directly influences the size of synthesised nanoparticles. Generally, the higher the concentration of surfactant molecules in the solution, the smaller nanoparticles are obtained [56].

The nanoparticle size can be also controlled through a number of subsidiary parameters, such as the solution temperature and stirring speed during the synthesis. The effects of temperature are not simple to interpret. Higher temperature increases the diffusion of atoms and clusters, leading to a faster and easier coalescence of clusters and the formation of larger nanoparticles. On the other hand, the higher diffusion leads to a faster chemical reaction, which usually results in smaller nanoparticles obtained. There is a general agreement that higher temperature leads to larger nanoparticles with wider size distribution [46], [57], [58], however there are cases of the opposite relation as well [59]. Larger nanoparticles can be obtained by lowering the stirring speed of the solution during synthesis. Slower stirring rates lead to uneven concentrations of reactants in volume, consequently slowing down the reaction, which gives more time to clusters to aggregate and form larger nanoparticles [60].

Although the wet bottom-up methods allow for the precise tailoring of nanoparticles' shape and sizes, these advantages come at a cost of a lower fabrication throughput and concentrations of nanoparticles in obtained solutions. Furthermore, such methods are extremely sensitive to any contaminants and even the slightest alternations of the fabrication process. Far greater concern should be given to the presence of residual chemical substances in the nanoparticle solution, left after the synthesis. These chemical residues, along with the residual surfactant layer on the surface of nanoparticles limit their applications, as these undesired side products minimize the reactivity of synthesised nanoparticles and influence the plasmonic behaviour of studied nanoparticles. Finally, it is not possible to synthesize nanoparticles out of any material. While the optimisation and development of syntheses of gold, silver and palladium nanoparticles were driven by their promising applications and advances in plasmonics, other less popular materials are yet to be studied. For this reason, finding a functional procedure for synthesising nanoparticles of different non-noble materials is needed.

2.7 Suitable non-noble plasmonic materials

Gold, silver and to a lesser extent copper and aluminium were found to be ideal plasmonic materials for their availability, relative chemical stability, non-toxicity, and ease of production in the industry. The only issue regarding the aluminium and silver is the instability of antennas due to the oxidation, which with time changes the structure and with it, the plasmonic behaviour. Furthermore, these metals (with the exception of aluminium) can be used for plasmonic applications only in the visible and near-infrared parts of the spectrum [61]. Therefore, it is vital to find other non-noble plasmonic materials, which can be used in visible (1.5–3 eV) to near ultraviolet (3–6 eV) wavelengths.

Metal is considered a good plasmonic material in a certain part of the spectrum if two following conditions regarding the real and imaginary parts of metal's dielectric function ε_m are fulfilled

$$Re[\varepsilon_m] < 0$$
 , (2.9)

$$|Im[\varepsilon_m]| < |Re[\varepsilon_m]|, \tag{2.10}$$

while the first condition is a necessary condition for the metal to support SPPs and consequently LSP resonances, the second condition describes that the losses, which are related to the $Im[\varepsilon_m]$ must be sufficiently small. In the range from 1.5 eV to 6 eV, some of the materials which fulfil the conditions above have already been studied in papers focusing on theoretical calculations of their plasmonic properties. These materials are aluminium (Al), gallium (Ga), indium (In), magnesium (Mg), tin (Sn), thallium (Tl), lead (Pb) and bismuth (Bi) [62], [63]. I decided to exclude thallium for its acute toxicity. In the case of Sn, a different problem appeared. Although Sn seems to be a good plasmonic material in the spectral region of interest, its instability connected with the phase transition close to room temperature (known as tin pest) might cause the disintegration of fabricated nanostructures. For these reasons, I decided to give up on tin and exclude it as well. Further on, materials whose plasmonic properties in the VIS-UV range have already been studied experimentally were excluded as well, namely magnesium [64], aluminium [65], and gallium [11]. Consequently, I focused on three possible candidates, which are Pb, Bi and In.

One of the main factors deciding which material should I study is whether our instruments are sensitive enough to measure the plasmonic resonances in antennas of the chosen materials. To verify that, I turned to the numerical simulations of loss probabilities using the boundary element method (BEM) in the Matlab computational package MNPBEM [66]. I calculated the loss probabilities of each material and compared the loss probability maxima of their LSP resonances to those calculated for gold. Since we commonly measure the LSP resonances in gold antennas, if the loss probability maxima of different metals are comparable to those of gold, the LSP resonances should be measurable with our system [67]. For these calculations, I used the following dielectric functions: lead [68], bismuth [69], indium [70], gold [71], and aluminium [72]. Finally, I calculated the loss probabilities of a 150 nm wide bowtie antenna on a glass substrate, with the electron beam passing in the middle of the antenna's gap, as can be seen in Figure 8. For gold, the antenna supports an antibonding longitudinal dipole mode [4] at the energy of 2.04 eV with the loss probability maximum being 2.9·10⁻² eV⁻¹. Out of the three tested new plasmonic materials, the lowest loss probability maximum was achieved for In, where the calculated maximal loss probability was $0.6 \cdot 10^{-2} \text{ eV}^{-1}$. Further on, the LSP resonance peak was broad. Such peak broadening is related to losses in material. These losses were expected, since in the spectral range of interest, the imaginary part of In dielectric function has

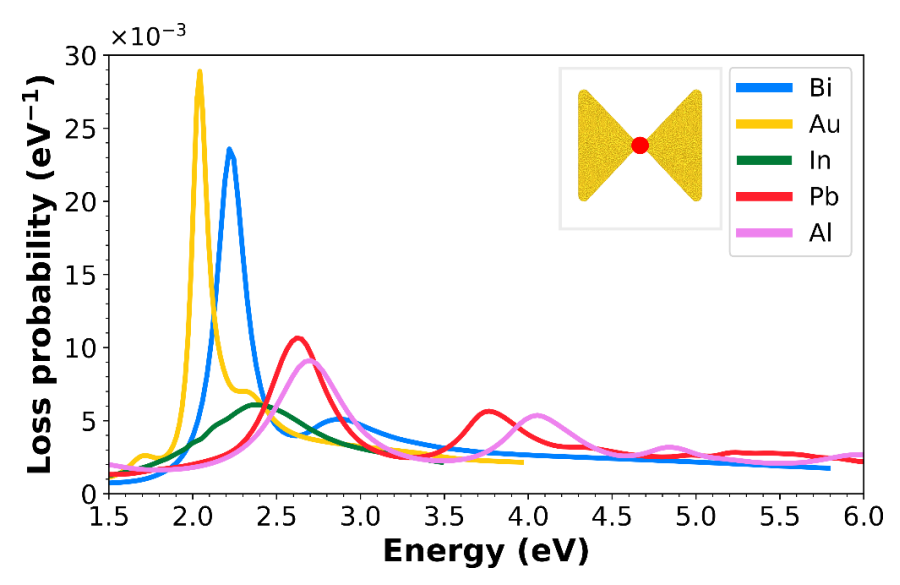


Figure 8: Loss probability spectra of 150 nm wide bowtie antenna with 20 nm gap between its wings calculated using the boundary element method for various antenna materials. The red dot in the middle of the bowtie antenna marks the position of the electron beam.

similar values as the real part [62], [70]. The LSP resonances of Pb were at 2.6 eV with the loss probability maximum of $1.1 \cdot 10^{-2} \, \text{eV}^{-1}$ and $3.8 \, \text{eV}$ with the loss probability maximum of $0.6 \cdot 10^{-2} \, \text{eV}^{-1}$. Although Pb promises possible rich applications in UV plasmonics, the material itself is considered toxic and obtaining Pb layers and nanoparticles is nearly impossible due to the safety regulations involved. The LSP resonances in bismuth had the loss probability maxima closest to those of gold. The loss probability in bismuth peaked at $2.3 \cdot 10^{-2} \, \text{eV}^{-1}$. Although both calculated Bi resonant modes were deep in the visible part of the spectrum, their relatively high loss probabilities make bismuth an attractive plasmonic material. Therefore, Bi will be the main subject of my focus.

2.8 Plasmon resonances in bismuth antennas

Within this thesis, I focus on three main types of plasmonic nanostructures. These are bar-shaped antennas, bowtie-shaped antennas and metallic nanospheres. The lowest resonant mode in a bar-shaped antenna is the longitudinal dipole mode, where the highest probability of LSP resonance excitation is at the edges of the antenna. The second lowest mode, the longitudinal quadrupole mode, has the highest probability of LSP resonance excitation in the middle of the antenna. At higher energies, higher modes like the transverse dipole and longitudinal hexapole, as well as higher order modes can be seen. The loss probability spectra of a bar-type antenna along with the loss probability maps of the lowest two modes and their normalised charge distribution calculated by the MNPBEM is shown in Figure 9. More information regarding the LSP resonances in bar-shaped antennas can be found, for example, in [73].

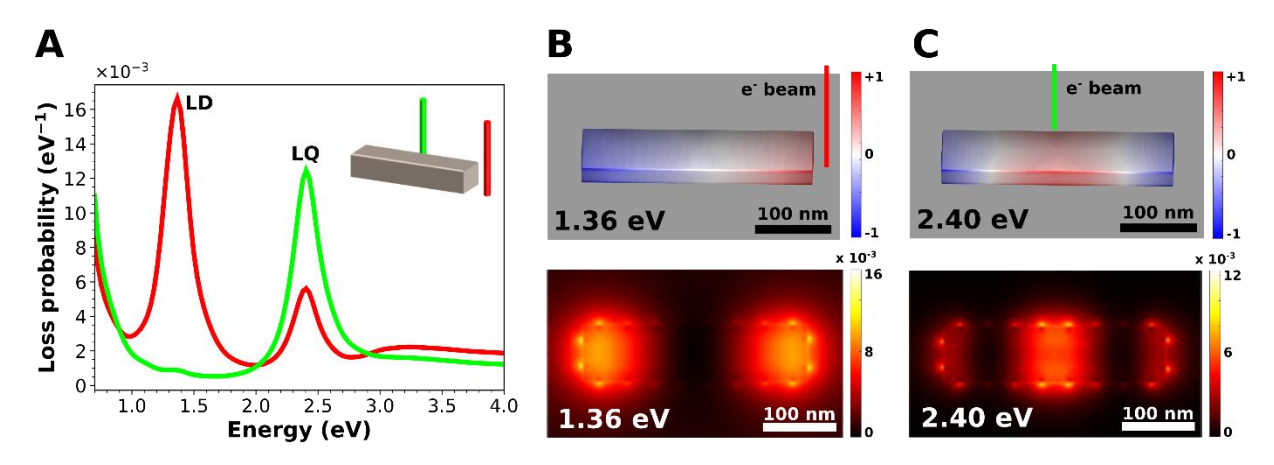


Figure 9: LSPR modes in a 300 nm long 80 nm thick bar-shaped bismuth antenna in vacuum calculated by the calculation package MNPBEM. **A:** Loss probability spectra of the electrons passing next to the edge and centre of the antenna. Two peaks corresponding to the longitudinal dipole (LD) mode at the energy of 1.36 eV, and the longitudinal quadrupole mode at the energy of 2.4 eV. **B:** Normalised surface charge distribution of the LD mode in the bar antenna, along with the loss probability map of the LD mode in the bar antenna.

Bowtie antennas are made of two triangular wings with a non-conductive gap in between them. The lowest resonant modes are the bonding and antibonding transverse dipole (TD) modes. At higher energies, the antibonding longitudinal dipole (LDA) mode can be seen. In well-fabricated antennas made of good plasmonic material, higher resonant modes can be identified too. The loss probability spectra of a 450 nm tall bismuth bowtie antenna with a 20 nm gap on a SiN_x membrane, along with the loss probability maps of individual LSPR modes are depicted in Figure 10. The loss probability is proportional to the out-of-plane electric field. For this reason, we see the loss probability maxima in the vicinity of the accumulated surface charge. More detailed studies of LSPR modes in bowtie antennas can be found in References [4], [74].

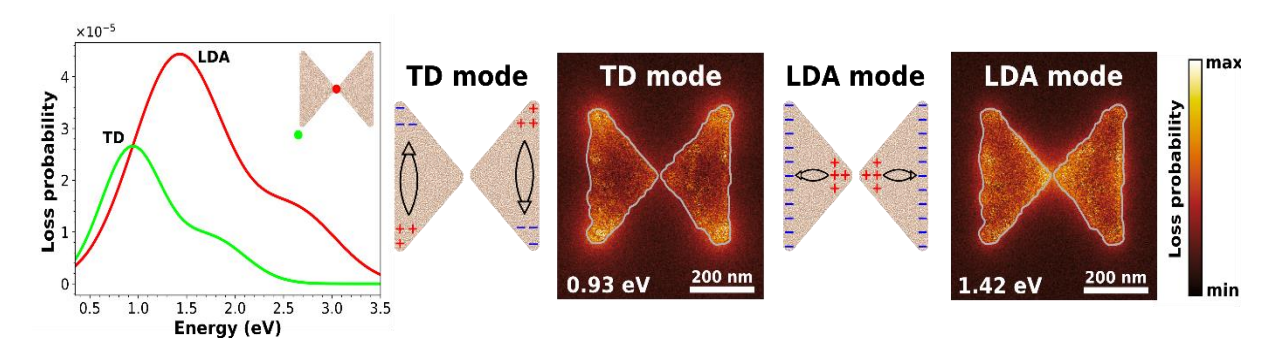


Figure 10: LSPR modes in a 450 nm tall bismuth bowtie with a 20 nm gap measured by STEM-EELS. In the measured spectra, the two lowest resonant modes, transverse dipole and antibonding longitudinal dipole modes are distinguishable. The peaks of the antibonding and bonding transverse dipole modes are at similar energy positions and in the measured EEL spectra appear as one peak [4]. For this reason, I decided to collectively call both a transverse dipole (TD) mode. The simplified depictions show the surface charge distribution of transverse dipole antibonding (TD) and longitudinal dipole antibonding (LDA) modes. The surface charge distribution diagrams have been taken and modified from [4].

The number of observable LSPR modes in spherical nanoparticles depends on the nanoparticle size. The lowest mode, which can be observed in metallic nanoparticles of nanometre scale, is the dipole mode. Based on the BEM calculations, in the case of a 100 nm bismuth sphere, the

dipole mode seems to be the only observable mode. When the diameter of nanosphere increases, higher resonant modes can be observed as well. Calculated energy loss spectra, normalised surface charge distribution, and loss probability map of the dipole mode excited in a spherical bismuth 100 nm wide nanoparticle can be seen in Figure 11. A more detailed study of the LSPR modes in spherical nanoparticles can be found in [75].

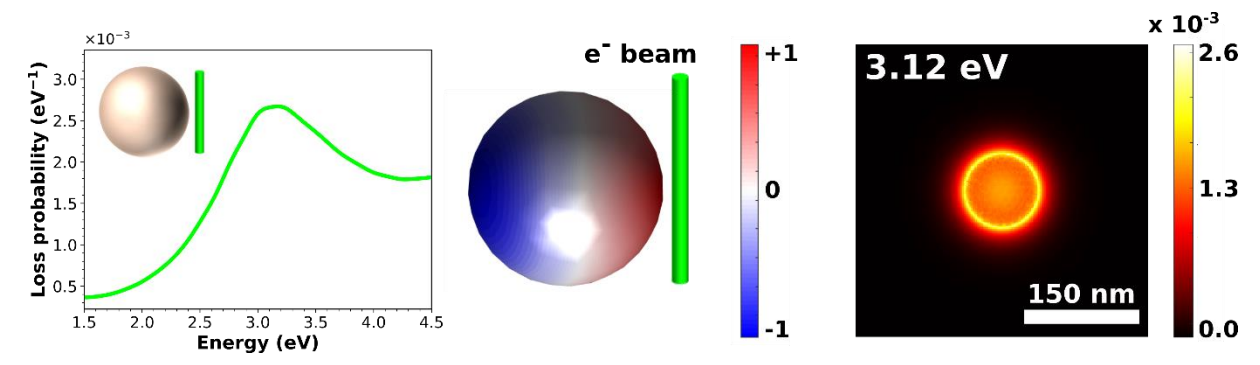


Figure 11: Loss probability spectra of spherical nanoparticle with the diameter of 100 nm calculated by MNPBEM package. The peak at the energy of 3.12 eV corresponds to the dipole mode. The position of the electron beam exciting the mode was 10 nm next to the nanosphere. The calculated normalised surface charge distribution proves the mode is a dipole mode. The map on the right shows the loss probability map of the dipole mode.

3 Bismuth

Bismuth is a material with a number of unusual properties, which differ for bulk material, layers and nanoparticles. In the following sections, I discuss the unusual properties of bismuth and summarise recommendations for the preparation of bismuth layers and nanoparticles obtained from various studies.

3.1 Introduction to bismuth

3.1.1 Bulk bismuth

Bismuth is a dense semimetal with extraordinary properties. For a long time, it has been considered the heaviest stable element, despite the theoretical calculations claiming that bismuth is a subject of an alpha decay. These predictions have only recently been verified by an experiment [76]. Luckily, the half-life of Bi is so long, that it is still considered safe even for medical and biological applications and the material is considered biocompatible. Bismuth has the lowest thermal conductivity of all elements, and it is also the strongest diamagnetic material to exist. Further on, it has a low melting temperature of 271 °C. Bismuth is a semimetal, which means that the valence and conduction bands are divided by an energy gap, except for a few points in the band diagram, where the bands overlap, with an overlapping energy of approximately 40 meV [77]. This is caused by the not-so-common rhombohedral crystal structure. Due to the small effective mass of electrons $(0.003m_e)$ compared to the mass of holes, a Baber scattering is the main source of electrical resistivity in bismuth [78], [79]. The high mobility of electrons does not significantly differ for polycrystalline and monocrystalline bismuth [77].

Thanks to the rhombohedral structure and its affinity to the formation of puckered bilayers, bonds in an atomic layer are far stronger than bonds between two atomic layers. Therefore, bismuth is a van der Waals material and is brittle and easily cleavable along the (111) orientation. Interestingly, bismuth can change its structure to pseudocubic when exposed to moderate temperatures and pressures, for example during annealing or when a lattice mismatch is introduced by a careful choice of substrate during a deposition [80]. Monocrystalline bismuth exhibits both de Haas-van Alphen (oscillations of magnetic susceptibility with the increasing external magnetic field) and Shubnikov-de Haas (oscillations of electrical resistivity with increasing magnetic field) effects [81].

As the volume of bismuth decreases, more interesting phenomena occur, with not all of them being explained up to now. The transition from semimetal to semiconductor in thin bismuth films is one of them. According to the calculations, the transition was expected to occur for films with thicknesses below 32 nm in the case of monocrystalline films. However, although such a tendency has been observed in monocrystalline samples, a different interesting property of bismuth, the high conductivity at the surface, somewhat suppresses the semiconducting behaviour. The increased electrical conductivity at the surface is caused by surface electron energy states created through the spin-orbital splitting of bismuth bands [77].

Further on, it is expected that bismuth layers below 10 nm in thickness do not behave as a plasmonic material at all, because of the de Broglie wavelength of electrons at the Fermi energy level. Since the Fermi energy is temperature dependent, this offers the opportunity of tuning and switching between the plasmonic and non-plasmonic transition of a sufficiently thin layer. A more detailed description of bismuth and its properties can be found in [81].

Some of the properties listed above apply only to the case of monocrystalline bismuth. When it comes to polycrystalline bismuth thin layers and nanoparticles, the properties can differ heavily. Therefore, in the following subchapters, I focus on the properties of polycrystalline bismuth thin layers and nanoparticles, together with various techniques for their fabrication.

3.1.2 Bismuth polycrystalline layers

One of the most significant characteristics of thin bismuth layers is the existence of surface electronic states, which ensure good electrical conductivity. The density of these states does not depend on the film thickness, as long as the substrate coverage is sufficient. However, the surface states strongly depend on the layer's surface roughness. It is essential, for these states to exist, that the surface roughness is as low as possible [82]. Unfortunately, nearly all physical vapour deposition (PVD) related deposition techniques yield similar or the same texture and structure of the final layer, along with comparable surface roughness values, except for layers deposited by pulsed laser deposition (PLD), which yield the lowest surface roughness [83]. Interestingly, polycrystalline bismuth layers have higher concentrations of holes, than electrons [84].

Generally, a bismuth layer deposited by PVD techniques contains round grains with an average diameter of around 100 nm and higher. Some of the grains appear to be faceted. On top of these grains are large bismuth boulder-looking structures, which can be up to hundreds of nanometres wide. Originally, these were seen as oxidized bismuth structures, but elemental analysis, along with electron diffraction proved these structures to be pure bismuth [85]. A typical example of the deposited bismuth layer from literature can be seen in Figure 12.

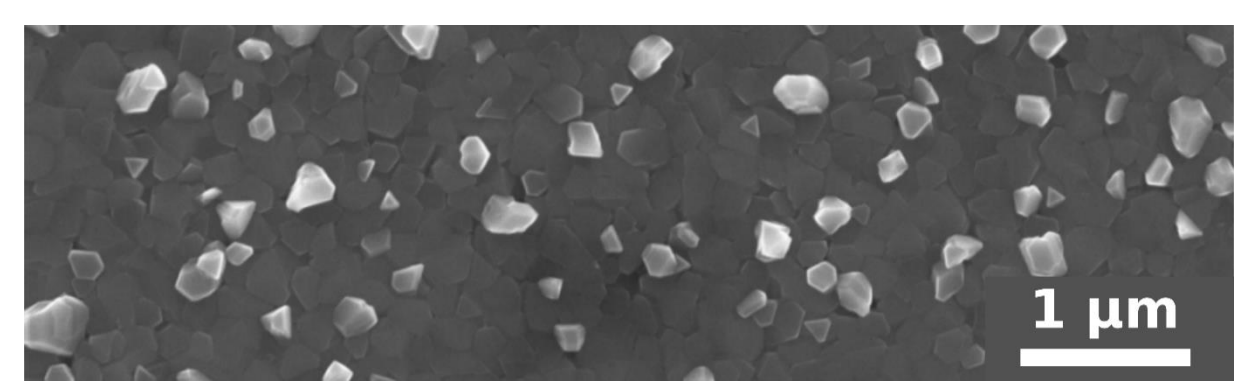


Figure 12: SEM micrograph of a typical polycrystalline bismuth layer deposited by electron beam evaporation. The layer contains polygonal grains with large protrusions on the surface (bright grains). The micrograph was taken and modified from [88].

Annealing, one of the most common methods for improving the structure and surface roughness of thin films, is quite complicated in the case of bismuth. Reaching temperatures above 250 °C leads to the desorption of bismuth atoms from common substrates and leads to a complete destruction of the deposited layer [86]. Further on, while in some studies, a growth of grains connected with annealing has been reported, in others, the growth of grains was found to be negligible [87]. The low melting temperature of bismuth leads to a belief, that low-temperature long-term annealing might ensure the survival of the bismuth layer, while the long annealing time would compensate for the lower diffusion coefficients. Unfortunately, such an annealing strategy fails to change the structure of bismuth layers as well [88].

An alternative approach for increasing the grain size, lowering the surface roughness, and eliminating large surface bismuth structures is pre-heating the substrate during deposition. The biggest grain growth and the lowest surface roughness were achieved for substrates pre-heated

to temperatures from 50 °C to 80 °C. For temperatures above 100 °C, the layer becomes porous and discontinuous [85], [86]. The elevated substrate temperature during the deposition leads to lowered resistivity of deposited films. Further on, the density of charge carriers lowers, and their mobility increases with the increased substrate temperature. Strangely, the crystallography of bismuth layers seemed to remain similar for all substrate temperatures.

The thickness of polycrystalline bismuth layers affects its properties heavily too. The thinner the deposited layer, the higher the concentration of charge carriers, while their mobility is lower [89]. Generally, thinner deposited layers have higher resistivity, smaller grains and with it, lower magnetoresistance [90]. Furthermore, very thin layers with thicknesses below 20 nm suffer from microstrain, which increases as the layer gets thinner. Layers above 20 nm have almost no microstrain. Although microstrain depends heavily on the type of the used substrate, the same strain-thickness dependencies have been found for copper and glass substrates, which suggests the same behaviour might be found for various other substrates [91]. Based on calculations, strain in metallic nanostructures affects the absorption probability of incoming light and the near-field enhancement [92].

Polycrystalline bismuth layers exhibit a strange behaviour, where neighbouring grains have nearly identical crystallographic orientation with respect to the substrate surface, with only slight orientation misalignment. Such structure is known as mosaic structure and leads to difficulties in the evaluation of grain size in a TEM or a STEM, as the diffraction contrast differences are minimal. To find the true grain size, the X-ray diffraction (XRD) analysis is often necessary [91].

In conclusion, based on the literature, the optimal approach is to deposit bismuth on a pre-heated substrate with a temperature of around 65 °C to achieve lower surface roughness and larger grains. Since the deposition methods yield similar results, sputtering, evaporation, and PLD are all viable options. It is beneficial to keep the layer thickness above 20 nm, to avoid the presence of microstrain, which can negatively affect the plasmonic behaviour of fabricated structures.

3.1.3 Bismuth nanoparticles

Bismuth nanoparticles (NPs) are mostly used in medical applications. They serve as cancer-tissue-sensitisers, which increase the absorption of X-rays in tumours during their treatment by radiotherapy. The NPs are also used as a contrast medium during computer tomography imaging [93]. The medical applications usually require nanoparticles with diameters below 100 nm, to increase the mobility of the NPs in the patient's body. Therefore, most of the fabrication approaches have been optimised for synthesising small NPs. Such small nanoparticles are usually synthesised from the three most common precursors, bismuth nitrate (Bi(NO₃)₃), bismuth dodecyl-mercaptide, and bismuth chloride (BiCl₃). Syntheses based on the chemical reduction of these three precursors result in small nanoparticles with diameters up to 30 nanometres. Larger NPs can be fabricated by thermolysis of reagents with low decomposition temperatures, such as bismuth acetate. A common approach is to use bismuth's low melting temperature to obtain liquid droplets of Bi in the solution. The sudden solidification of the droplets by injection of cold ethanol ensures that Bi NPs will keep their round shapes. No matter the approach used, all the created NPs are monocrystalline, in a typical rhombohedral structure. The rhombohedral structure can be changed by electron irradiation into a cubic structure or cubic core with a rhombohedral shell. Such mixed-structure NPs then experience large strain [94].

One of the interesting characteristics of Bi NPs is their high Seebeck coefficient. During the Seebeck effect, heat gradient results in an electric potential difference. The higher the Seebeck

coefficient, the higher the voltage difference will be between the cold and warm parts of the material. Smaller Bi NPs have a higher Seebeck coefficient due to the quantum confinement effects and induced semiconducting behaviour. The semiconducting behaviour was observed even in NPs with a diameter of 210 nm [95]. In chemically synthesised nanoparticles however, the semiconducting behaviour appears only for far smaller diameters below 100 nm [96]. Therefore, it is probable, that the fabrication approach affects the behaviour of Bi NPs. The semiconducting behaviour of fabricated NPs can be verified by measuring their resistivity at different temperatures. If the resistivity in the low-temperature region is constant and lowers at higher temperatures, the fabricated nanoparticles are semiconducting. Based on the resistivity curves, the energy of the forbidden gap $E_{\rm g}$ can be obtained. For nanoparticles with a diameter of 160 nm, the $E_{\rm g}$ was found to be 0.06 eV [95].

Another peculiar attribute of Bi NPs is their anisotropic conductivity [97]. The anisotropy causes an interesting plasmonic effect, where the observed LSPR peaks are twinned. For example, the absorption peaks attributed to the LSPRs of 15 nm spherical NPs were at wavelengths of 282 and 277 nm (difference of 0.08 eV) [98]. The same twinning of LSPR absorption peaks has been recorded in other works as well [99]. Although the plasmonic behaviour of bismuth nanoparticles has already been studied on large ensembles, a study of the plasmonic properties of individual nanoparticles is missing.

The thermolytic fabrication approach appears to be the best technique for obtaining nanoparticles with diameters in the range of hundreds of nanometers. NPs with these sizes are conductive and thus ideal for studying the plasmonic behaviour of bismuth. The size during thermolytic synthesis can be controlled by the stirring speed, maximum achieved temperature of the solution and concentrations of surfactant [95], [100]. Surfactant is required during the synthesis at all times. Without the presence of a surfactant, bismuth nanoparticles oxidize even during the synthesis itself and Bi₂O₃ NPs are formed instead of pure Bi nanoparticles [98].

3.2 Fabrication of bismuth plasmonic antennas

Based on the recommendations for the deposition of bismuth, as well as optimal FIB lithography strategies, I deposited bismuth layers and fabricated plasmonic antennas. In the following section, I will describe the experimental details during the deposition of bismuth layers and the FIB lithography. Further on, I analysed the structure of deposited layers and studied the fabrication yields and morphology of fabricated bismuth antennas.

3.2.1 Deposition and structural analysis of the bismuth layer

I deposited bismuth simultaneously on three SiN_x TEM membranes by DC magnetron sputtering in the Bestec Magnetron deposition chamber at CEITEC [101] under the supervision of Ing. Jan Prášek, Ph.D., who also aligned the sputtering source and prepared the chamber for the deposition. The SiN_x membranes were held in place by Kapton tape on the sample holder. For this reason, bismuth was deposited at room temperature, without any heating of the substrate, to prevent possible loss of adhesion of the Kapton tape and subsequent loss of the sample. The sample was approximately 200 mm from the target and the incidence angle of deposited bismuth atoms was less than 90° with respect to the sample surface. Although the non-normal incidence angle of deposited atoms during sputtering usually leads to an increased surface roughness and defects, the confocal geometry of targets does not allow deposition under a normal incidence angle. Furthermore, according to the instructions of Ing. Jan Prášek, Ph.D., the sample was placed in the middle of the sample holder. Because of the misalignment of the

sputter sources, the sample was slightly off-centre of the beam of deposited atoms. The optimal position is 1.6 cm away from the sample holder's edge. Our sample positioning during the deposition leads to uneven deposition of the material and increased roughness. To compensate for the uneven deposition, the sample was rotating at 5 rpm during the deposition. The simplified schema of the sample placement during the deposition can be seen in Figure 13.

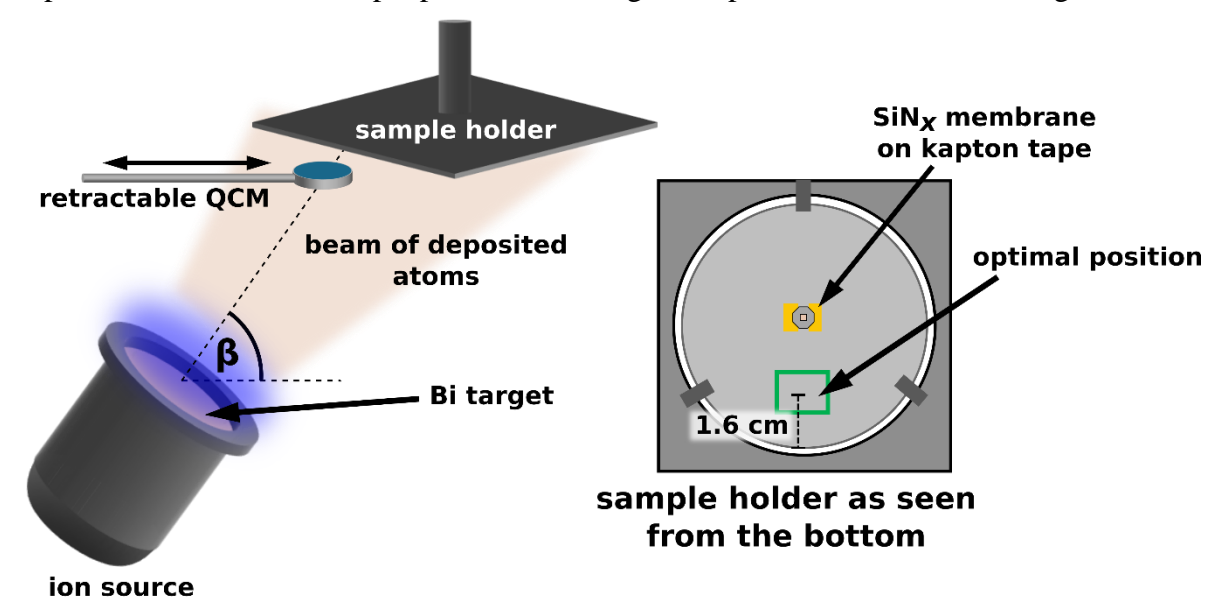


Figure 13: Simplified schema of deposition geometry inside the Bestec Magnetron. The ion source with a target on top is inclined under the angle β . Although the angle can be changed, it is not possible to deposit material with normal incidence on the substrate. Further on, the misalignment of the ion source and the sample holder requires placement of the sample approximately 1.6 cm from the sample holder's cutout edge, as marked by the green rectangle. The sample placement used during our deposition is symbolised by the SiN_x membrane in the sample holder's centre. The deposition rate can be measured only before and after the deposition itself, as the retractable quartz crystal microbalance shields the sample holder and sample if inserted.

The pressure inside the chamber during the deposition of bismuth was $8 \cdot 10^{-4}$ mbar, with an argon gas flux of 15 sccm. The bismuth target was bombarded by argon ions with an energy of 310 eV. The total current of argon ions was 25 mA. According to the quartz crystal microbalance, the deposition rate measured at the start and after the deposition was in both cases approximately 0.45 Ås^{-1} and the thickness of the deposited bismuth layer was 30 nm.

Initial investigation of the deposited layer surface by SEM confirmed it to be nearly identical to evaporated layers (see Figure 12). The surface is covered with protrusions and the layer itself is polycrystalline with relatively large polygonal grains (Figure 14A). A closer examination of the layer surface in SEM revealed a high number of dark dots (Figure 14B). These dark dots were visible only in the signal of secondary electrons, which gives information about the sample's surface.

Subsequent STEM analysis of the layer in Figure 15 not only verified the presence of dots inside the grains, but revealed a large amount of different, even smaller dots, at the grain boundaries. Since, the deposition itself was conducted immediately after a periodic cleaning of the chamber, connected with the exchange of targets, the possibility of contaminating the sample during the deposition is low. For this reason, I believe the dots to be pores or lattice defects in the deposited layer and not a precipitated contaminant. I measured the average grain size from STEM micrographs obtained from three different areas. The average grain size

is (74 ± 28) nm. The uncertainty interval is large because the layer contains grains with 15 nm in diameter as well as grains with a diameter of 217 nm.

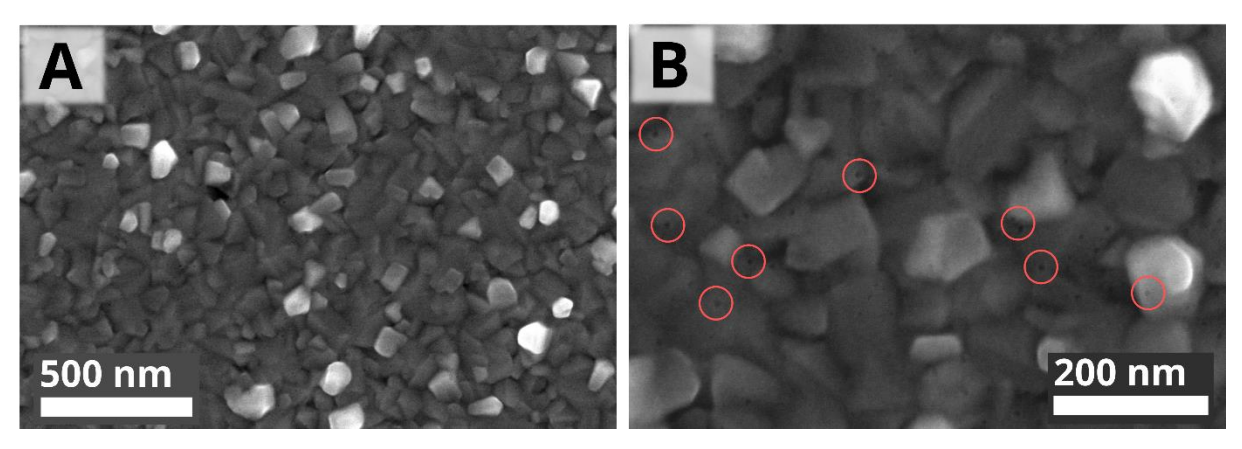


Figure 14: SEM micrographs (SE signal) of the deposited Bi layer. **A:** The deposited layer is in morphology clearly comparable with layers deposited by evaporation (Figure 12). It has mostly polygonal grains. **B:** Detail of individual grains with marked observed dots.

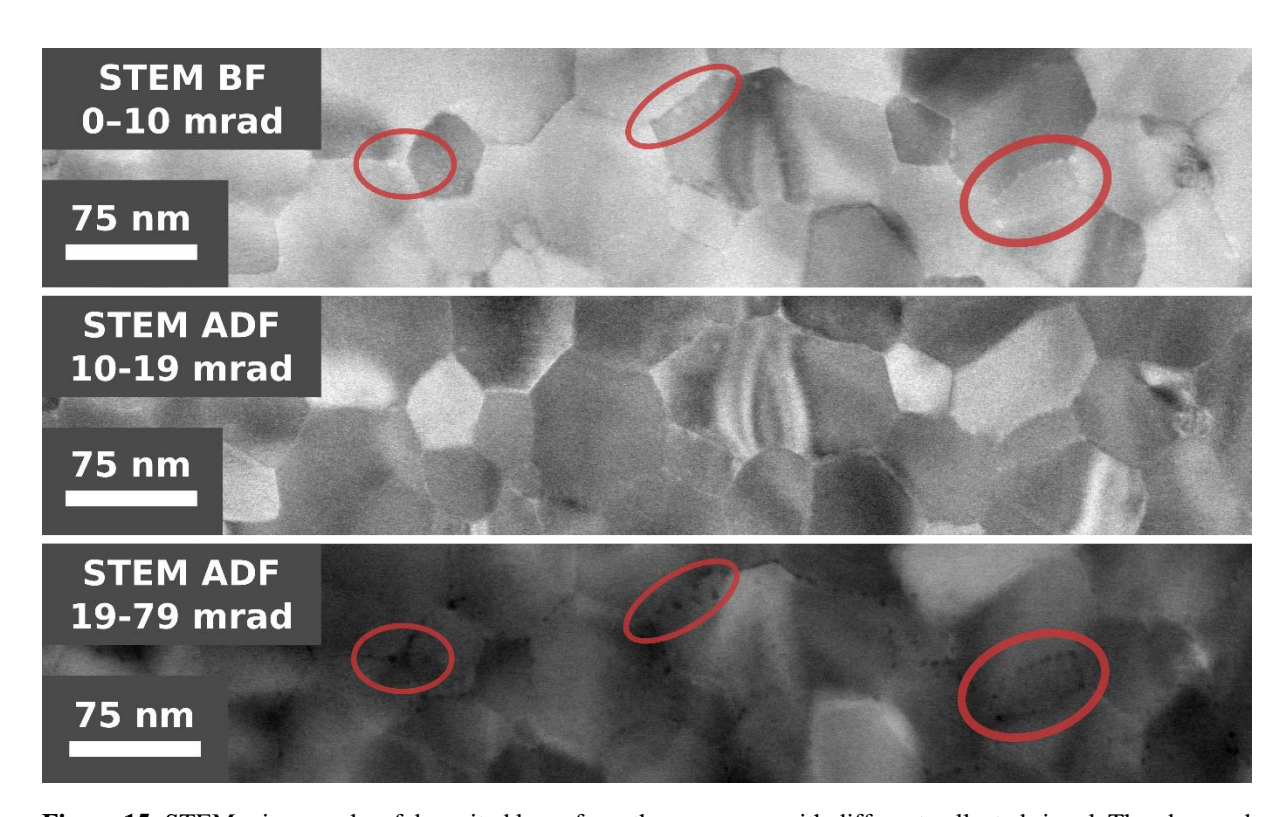


Figure 15: STEM micrographs of deposited layer from the same area with different collected signal. The observed dots are visible most clearly in ADF signal with collection angles between 19 and 79 mrad. We suspect these dots to be either pores or lattice defects, as they were visible in BF, ADF and HAADF signal. We evaluated the grain size based on STEM-ADF signal because the grain boundaries are clearly visible in the signal with collection angles from 10 to 19 mrad.

While the STEM micrographs of the layer allowed us to measure the lateral grain size, it does not give us any information about the vertical morphology of the layer. To examine the vertical grain size, a cross-section of the layer is needed. Therefore, I cut out a lamella from the part of the membrane where it is supported by a silicon frame. Since the SiN_x layer covers the entire membrane, the bismuth layer structure should be identical on both the silicon-supported and unsupported parts of the membrane. The thickness of the bismuth layer measured on the lamella was (42 ± 11) nm. The layer itself is very rough, which is the reason behind the large uncertainty interval of the measured layer thickness. The deposited bismuth film does not have any grains stacked on each other and consists of a single-grain layer, as can be seen in Figure 16. Therefore, the local thickness of the layer depends on the grain diameter. Such attributes are typical for layers grown in an island mode.

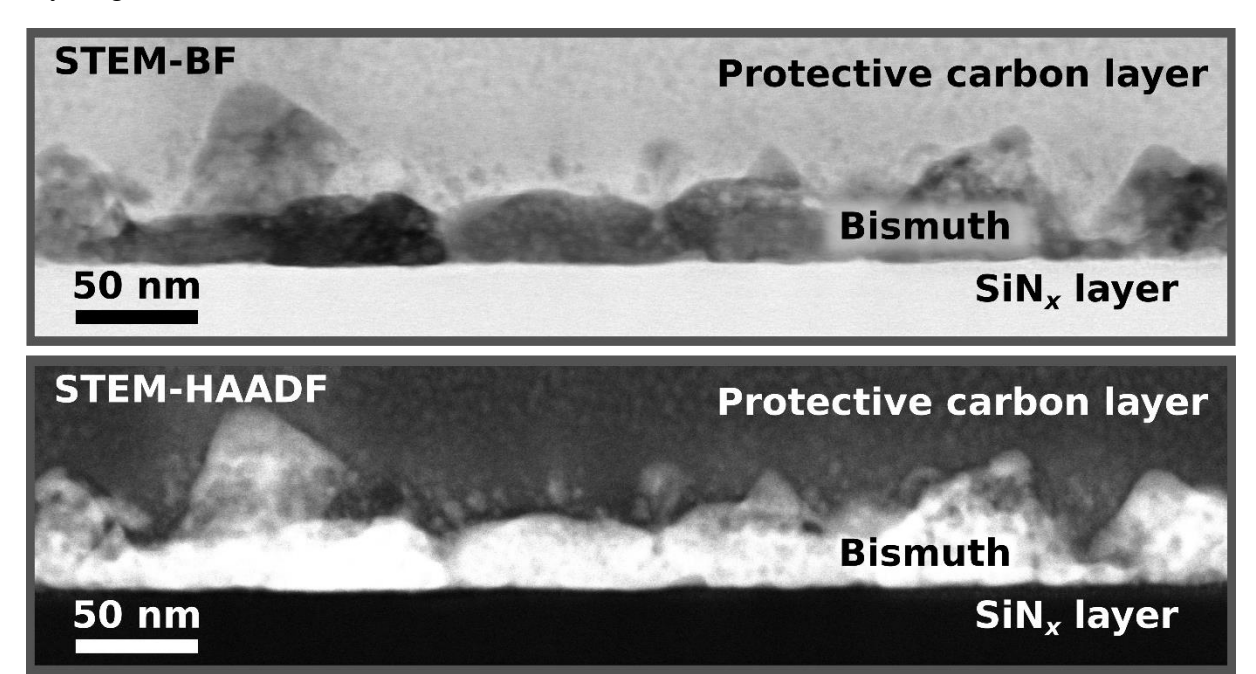


Figure 16: STEM-BF and STEM-HAADF micrographs of the lamella. Based on the BF signal, it appears the layer grew in an island mode. From the cross-section, we can see two imperfections of the layer, which might negatively impact the plasmon resonances in antennas. One is the high roughness of the layer, the second is the presence of imperfections of the layer at grain boundaries and SiN_x -bismuth interface. Both of these come from the island growth mode during the deposition and might be solved by using a different substrate.

To verify the purity of the deposited bismuth layer, I used an energy-dispersive X-ray spectroscopy (EDX) analysis on the lamella. The EDX revealed an oxygen layer on the interface between the bismuth and SiN_x layers. Although I expected the presence of oxygen in the bismuth layer (caused by oxidation), I did not anticipate it to be on the boundary of the SiN_x layer. However, this oxygen-rich layer has likely been present prior to the bismuth deposition and likely originates from the fabrication process of the commercially produced membranes. This conclusion is further supported by the presence of yet another oxygen-rich interface present between the SiN_x layer and the supporting silicon. Fortunately, no other contaminants (besides gallium introduced during the lamella polishing, and carbon, an omnipresent contaminant) were detected. The EDX maps can be seen in Figure 17.

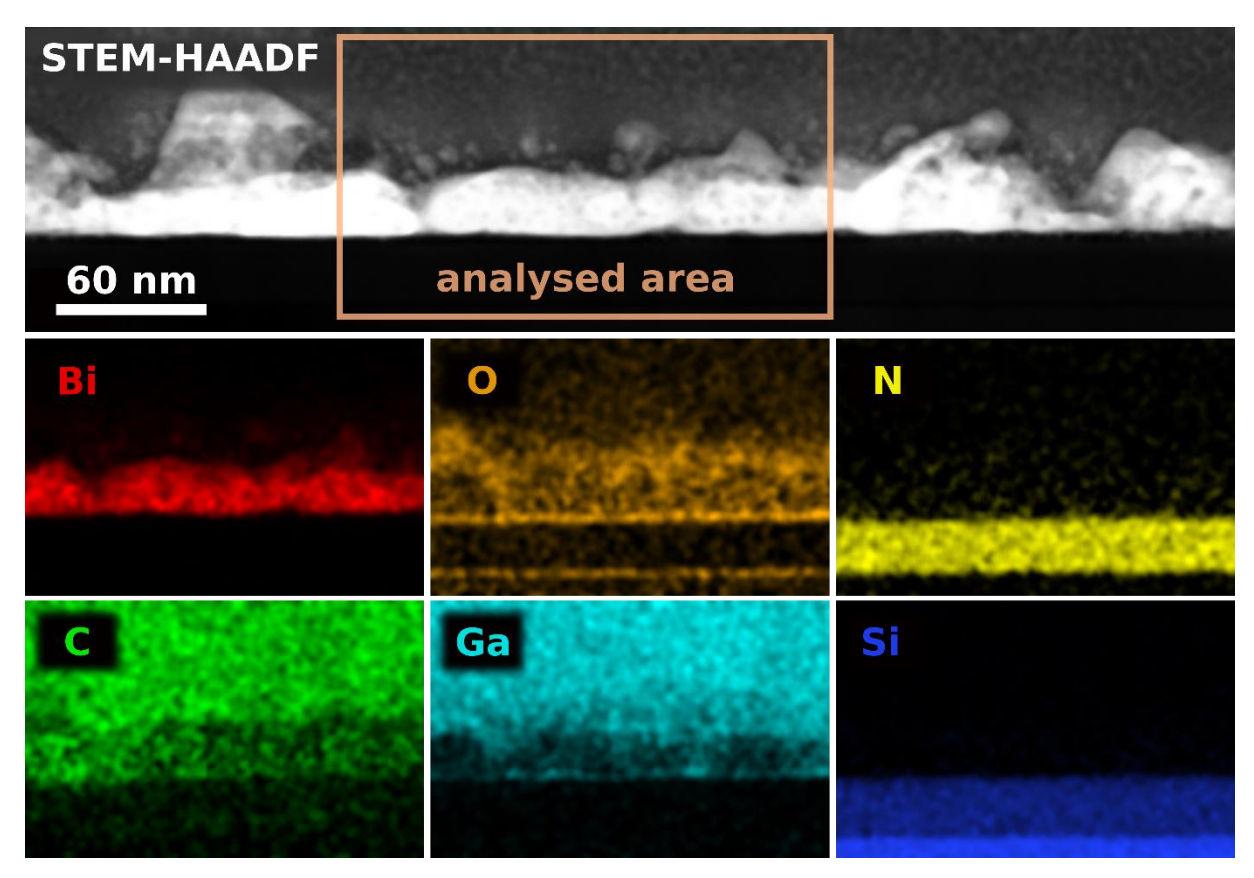


Figure 17: Elemental maps obtained by EDX analysis of the bismuth layer on lamella. The gallium was introduced by implantation of gallium ions during the lamella polishing. It is evident, that gallium precipitates primarily in bismuth grain boundaries. In an amorphous carbon protective layer, the gallium concentration is clearly uniform. Besides the gallium, carbon and oxygen, no other contaminants were found. There is clearly visible layer of oxygen on the interface of bismuth and SiN_x layers.

The grain size of the deposited layer can further be increased and somewhat unified by annealing. To get a less polycrystalline layer with larger grains and lower roughness, I tried annealing one of the bismuth layers. I left the sample to anneal at 145 °C for 30 minutes and then cool down at the rate of 1.5 °C/min. Unfortunately, the analysis of the layer in SEM, revealed no visible difference. For this reason, during the second annealing attempt, I decided to anneal the sample at the temperature of 260 °C for 5 hours and let it cool down at the same rate. The pressure in the furnace during both annealing processes was 2·10⁻¹ Pa. The bismuth layer changed colour, from the originally slightly gold to metallic grey with a blue hue. The investigation of the layer in SEM revealed distinct changes in the morphology. Each individual membrane along with SEM micrographs of their surface can be seen in Figure 18. The SEM micrograph of the annealed layer in Figure 18 shows large patches of material, which were charging when illuminated by the scanning electron beam, visible on the surface of the layer. In the gaps between these charging patches were the remains of the original bismuth layer, which looked very similar to the original deposited layers and were conductive. It was clear, that the bismuth layer partially oxidised during the annealing and the observed charging patches are probably made of bismuth oxide.

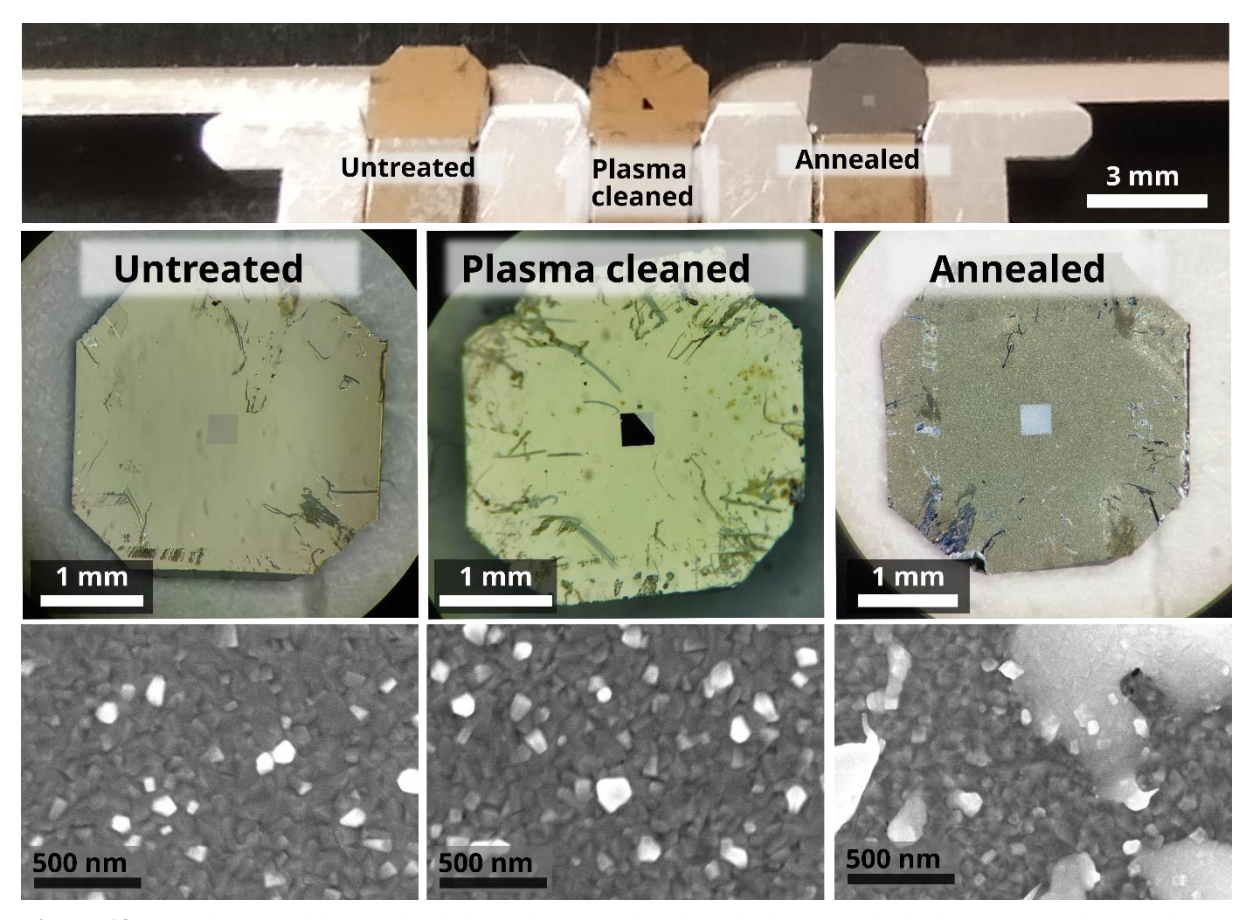


Figure 18: Membranes with deposited bismuth as seen by the naked eye, optical microscope and SEM (in SE signal). Annealing of the bismuth layer resulted in a change of colour from original slightly gold to metallic grey with a blue hue. Observation of the layer in SEM revealed large patches of charging material on the surface of the residual bismuth layer. Subsequent XRD analysis of the membrane identified the charging material as Bi₂O₃. Although multiple plasma cleanings of the Plasma-cleaned membrane also resulted in a slight colour change, no alternations of the layer surface were found in SEM.

Later XRD analysis of both the annealed and untreated layers (Figure 19) verified our expectations. The untreated layer contained only the bismuth crystal orientations, which were (003), (015), (112), (208), and (006) parallel to the sample surface. The annealed layer contained both bismuth and bismuth oxide grains. The bismuth orientations in the annealed layer were (012), (015), (112) and (208). The bismuth oxide was identified as a tetragonal-Bi₂O₃ phase. Only two orientations of the bismuth oxide were observed in the annealed layer, the dominant (201) and (423) orientations. I believe the annealing caused the transformation of bismuth (003) orientation into bismuth (012) orientation, as well as the oxidation of such oriented grains and the creation of bismuth oxide. The intensity of the bismuth (015) peak is nearly the same in both layers. That means the (015) orientation is resistant to oxidation. Since the (015) orientation is the dominant orientation in our layers, I believe it to be the reason behind the excellent stability of our layers, despite bismuth's notorious oxidation effects.

I also analysed a layer which underwent plasma cleaning treatment multiple times before various STEM and TEM measurements. This layer suffered a cumulative cleaning dose of 50 seconds in oxygen-argon (1:3 ratio) plasma. Based on the XRD analysis in Figure 19, it is clear the plasma cleaning caused minor oxidation of the bismuth layer. The bismuth (003) and (006) peaks are smaller, and a small bismuth (012) peak is present. Next to it is a very small bismuth oxide peak. Generally, the plasma-cleaned layer appears to be in a stage between the

clean untreated and the annealed layer. The broadening of observed peaks in XRD diffractograms verified the nanocrystallinity of all three layers.

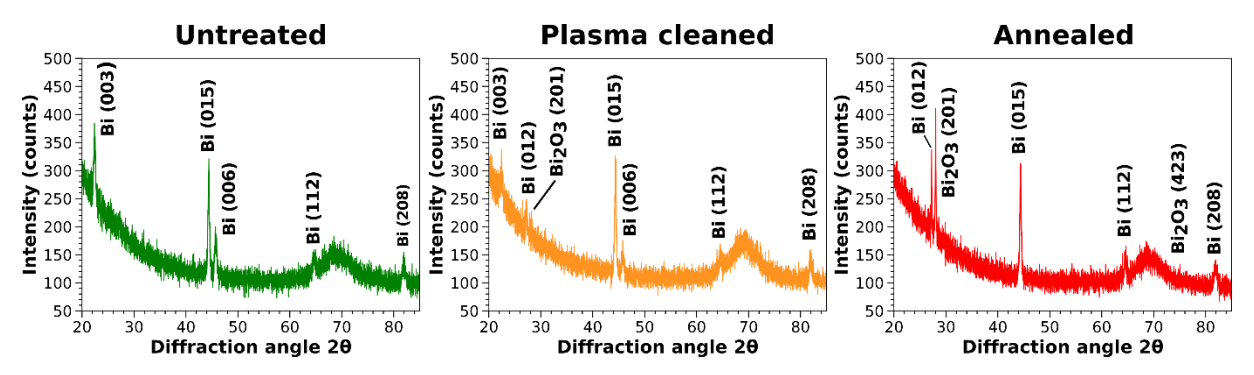


Figure 19: XRD diffractograms of untreated layer left on air for 6 months (green), layer which underwent multiple plasma cleanings throughout the 6 months (orange) and annealed layer measured after its annealing (red). Although bismuth is known for its susceptibility to oxidation, it remained stable on air. I believe it's caused by the dominant (015) orientation, which appears to resist the oxidation. Unfortunately, the plasma cleaning leads to oxidation and changes in the crystal structure of bismuth layers. All three diffractograms were obtained at the same time, with exactly the same optical setup. This allows us to compare the relative proportion of individual crystal orientations. The broad peak at the diffraction angle of 69° comes from the amorphous SiN_x substrate.

To quantify the surface roughness of the deposited layer, my colleague Bc. Marek Patočka measured the layer profile on 5 randomly chosen areas in the vicinity of the membrane window. It revealed how rugged the surface is. In all studied areas were large and tall protrusions reaching up to around 90 nm above the layer surface. The mean squared surface roughness (RMS) was found to be (11.2 ± 0.8) nm. Naturally, such extreme surface roughness will lead to large damping of plasmon resonances and might pose a difficult challenge during the lithography process. A layer profile measured by atomic force microscopy (AFM) can be seen in Figure 20.

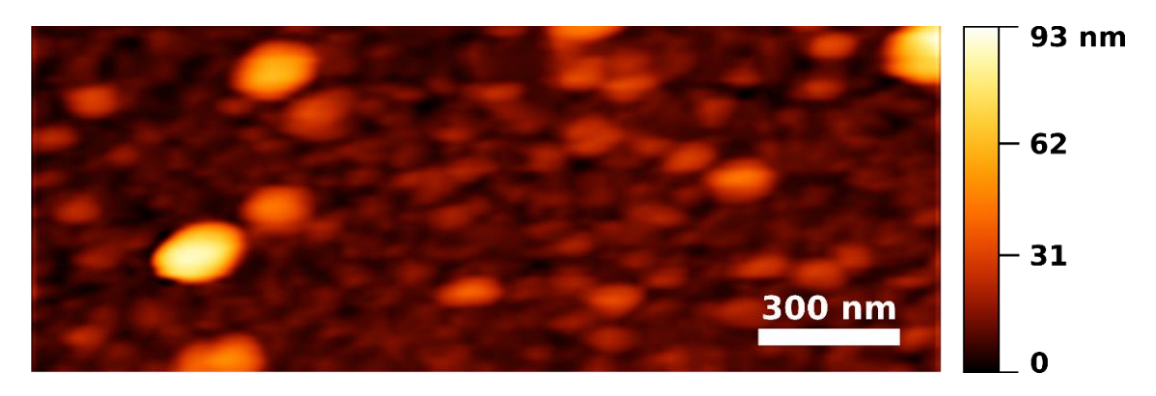


Figure 20: Surface profile of deposited bismuth layer measured by Bc. Marek Patočka using the AFM Litescope. The AFM measurement once again verified the island growth of bismuth during the deposition. The visible protrusions on the surface can sometimes reach up to nearly 100 nm in height.

Based on the structural analysis of bismuth layers, it is obvious that the fabrication of antennas by FIB lithography will be affected by the rough surface of the layer. I expect the presence of large residual grains where the surface protrusions are. On the other hand, the preferential crystallographic orientation of Bi (015) along with the large grain size might somewhat limit the preferential milling of certain crystallographic orientations and lead to antennas with more even edges.

3.2.2 Ion beam lithography of plasmonic antennas

Since the FIB lithography was done on the layer without any preceding plasma cleaning, I am confident, that the layer was not oxidated, and the structure remained unchanged at the time of the lithography. For the lithography, I used a SEM/FIB microscope FEI Helios [102]. Before the lithography, I cleaned the microscope chamber by three twenty-minute long plasma cleaning cycles, with 10 minutes of pumping between each cycle. Although such a cleaning process is highly time-consuming, it ensures that no carbon contamination will be created by the illumination of the surface by electron or ion beam. Such precaution is critical, as any created contaminating layer can affect the plasmonic behaviour of final plasmonic antennas. For the fabrication of the plasmonic antennas, I used gallium ions with an energy of 30 keV. The ion beam current during the lithography was 1.95 pA. The milling of the bismuth layer was extremely fast, due to the high sputter yield of bismuth. I found the optimal milling depth to be equivalent to 3 nm of silicon, as the milling depth parameter in the Helios microscope software stands for the total depth of material removed if silicon was milled. This means, that the removal of 30 nm of bismuth is equivalent to the removal of 3 nm of silicon. Based on the milling depth, the software calculates the ion dose needed and from it, the dwell time for which the ion beam will mill one point. The number of passes can be chosen. This means that double the passes will result in half the dwell time. In the case of bismuth, the best results were obtained for one pass of the ion beam over the milled area, which resulted in a dwell time of 12 us. For a higher number of passes, the milled area was covered by tiny residual grains. The comparison for different number of passes is in Figure 21.

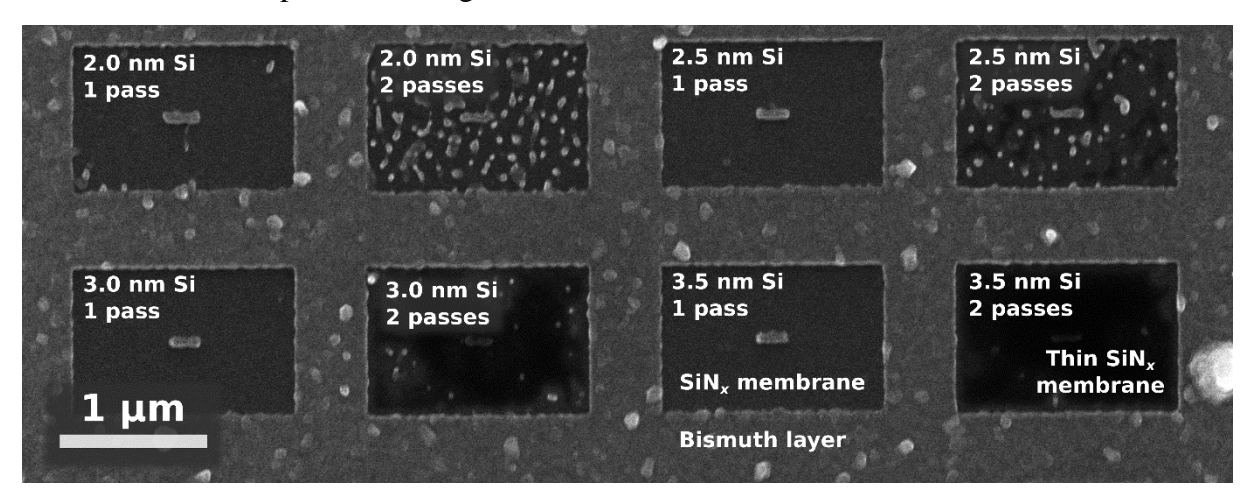


Figure 21: SEM micrograph of antennas fabricated with different milling depths (given in nm of removed Si) and number of passes over the milled area. The black-coloured areas mark where the thin residual SiN_x membrane is. It is a sign of an over-milled area. On the contrary, white dots in the milled area are caused by redeposition on residual grains. Both undesired effects, the over-milling and redeposition were worse for a higher number of passes.

Once I found the optimal milling depth and number of passes, an ideal milling strategy needs to be found too. The milling strategy is used to eliminate redeposition and to obtain structures with more even edges. The software on Helios offers two types of rastering and four options for the direction of milling. All of these are schematically depicted in Figure 22. The rastering types decide if the milling area is rastered line-by-line, or in serpentine. The milling directions decide where the milling of the area starts and where it ends. Usually, the area where the milling starts will suffer more redeposition as new lines will be milled and part of the newly removed material will redeposit on previously milled areas. To find the optimal milling strategies,

I fabricated 10 antennas for each of the raster types and milling directions and picked the raster type and milling direction with the highest number of antennas without any shape imperfections. For bismuth, the optimal milling strategy was the raster type named Raster with the direction of milling Right to left (this milling direction yields the same results as the Left to right milling direction). For the comparison, for gold, the best results were obtained with a raster type named Serpentine and Top to bottom milling direction. Therefore, it is clear that each different layer material requires an optimisation of the FIB lithography approach.

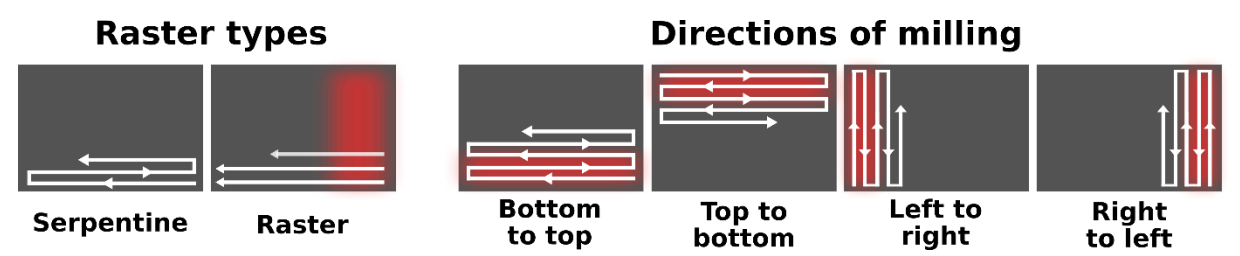


Figure 22: A schema of two raster types and 4 milling directions available in Helios software. The red hue marks the areas which will likely suffer higher redeposition. The Serpentine raster type usually limits the amount of redeposition and is thus the most frequently used raster type.

After the optimisation process, I could start the fabrication process. I fabricated three types of antennas, two bar-shaped antennas and bowtie antennas. The bitmaps used for the fabrication of these antennas are in Figure 23.

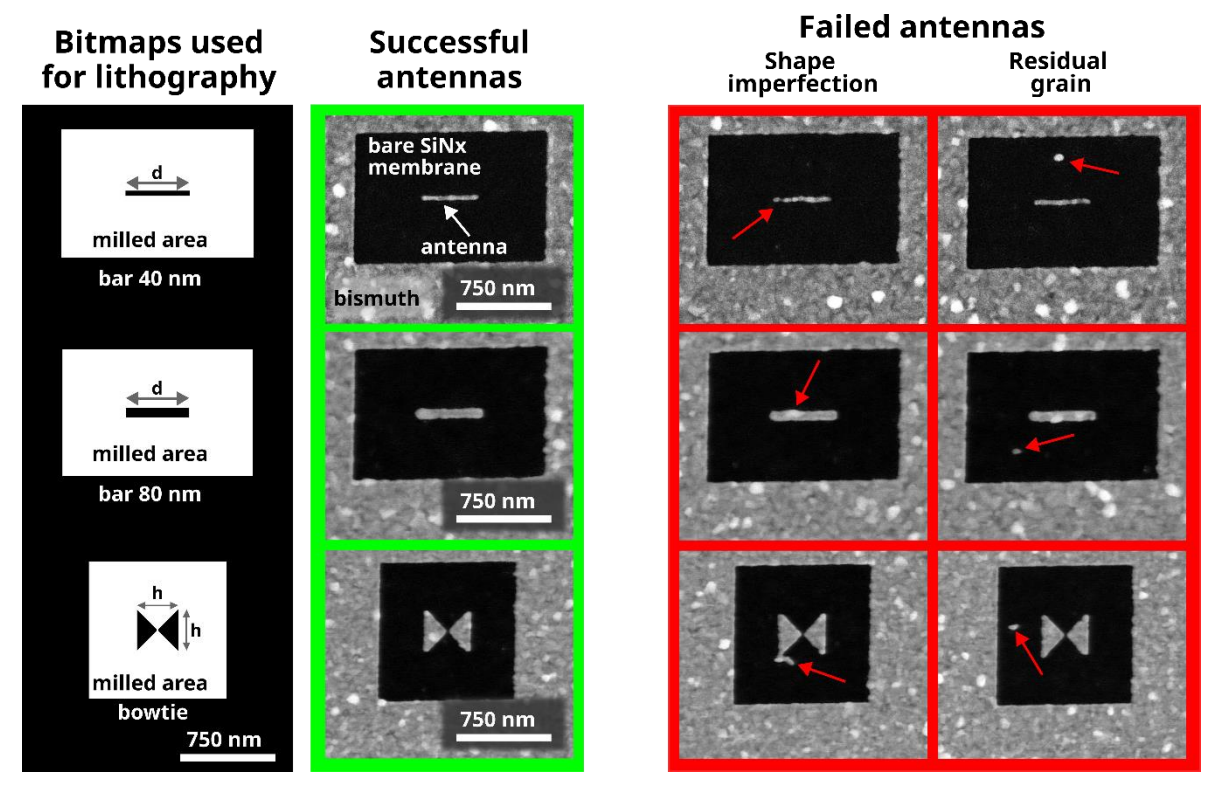


Figure 23: On the left are bitmaps used for the lithography of three antenna types, the 40 and 80 nm wide bar antennas with the length d being from 80 to 550 nm and bowtie antennas with the 20 nm gap and wing width h being from 200 to 700 nm. The STEM-HAADF micrographs of the successful antennas are marked green. The failed antennas are marked red. Even a minor shape imperfection or small residual grain within the milled area cause the antenna to be considered failed. The examples of antenna imperfections are marked by the red arrows.

The bar-shaped antennas were 40 and 80 nm wide. I fabricated the 80 nm bar-shaped antennas with lengths from 100 to 550 nm. The 40 nm bar-shaped antennas were from 80 to 350 nm long. The bowtie antennas have a 20 nm gap between their "wings". The wing width of the bowtie antennas was from 200 to 700 nm with a step of 50 nm. I fabricated 25 antennas for each set of dimensions and antenna type. To compare the ease of fabrication of each antenna type and size, I use the ratio of successful antennas divided by the total number of antennas (25 antennas). The antenna is considered successful if there are no shape imperfections and no residual grains in its vicinity. This ratio is further called the fabrication yield. Examples of both the failed and successful antennas are shown in Figure 23. The fabrication of antennas from the bismuth layer was far easier than from a gold layer studied within my bachelor thesis [53]. For this reason, I applied more strict rules for distinguishing between successful and failed antennas. If the antenna had any residual grain within the area of bare SiN_x membrane, or if the antenna was not perfectly rectangular (in the case of bar antennas) or triangular (in the case of bowtie antenna wings), it was considered failed. In my previous work, when evaluating the fabrication of gold plasmonic antennas, I was more benevolent [53]. The fabrication yields for each antenna type and antenna dimensions are in Figure 24.

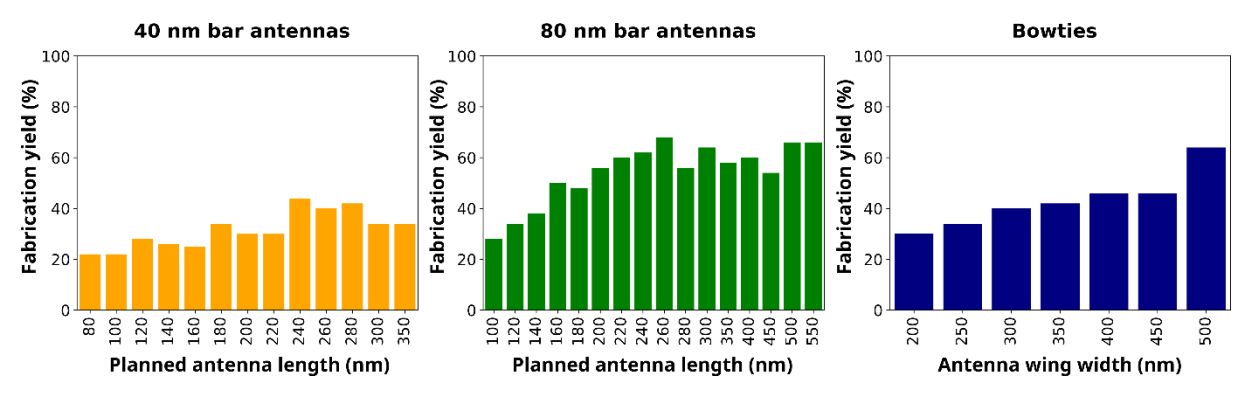


Figure 24: The fabrication yields of 40 nm and 80 nm wide bar antennas, and bowtie antennas. The antennas suffered primarily from shape imperfections. The residual grains were rare. For this reason, bigger antennas with its larger surface area tend to have higher fabrication yield.

On average, for the 40 nm wide bar antennas, the highest fabrication yield was achieved for antennas around 260 nm long. The fabrication yield of 40 nm bars is comparable for all antenna lengths. This means that the fabrication of these antennas is similarly difficult for all antenna lengths. It seems that the 40 nm dimension of any antenna is near the fabrication limit of the used SEM/FIB microscope. The fabrication yield of the 80 nm wide bars also culminates around the length of 260 nm, but on average, the fabrication yield of longer 80 nm bars is higher than the yield of the shorter antennas. The same trend is seen in bowtie antennas, where increasing the antenna dimensions leads to a higher fabrication yield as well. Usually, if the antennas suffer primarily from shape imperfections, a lower fabrication yield is observed for smaller antennas. Contrariwise, if the antennas suffer primarily from residual grains (caused mostly by redeposition or preferential milling of grains with different crystallographic orientations), the fabrication yield is higher for smaller antennas. Therefore, for our bismuth layer, residual grains are not an issue.

Besides the total fabrication yield, I also evaluated the average difference between the planned and real dimensions of successful antennas. Most of the time, the fabricated antennas are smaller compared to the size of the antenna shape in the used bitmap. This is because of the larger beam diameter in the focus plane. As the beam scans and removes the material, the edge of the beam mills also neighbouring areas, which leads to unplanned milling of the antenna. For

this reason, the real antenna dimensions are nearly always smaller than planned. For the evaluation, I use the Antenna length deviation, which is calculated by subtracting the planned antenna length from the average real length measured from STEM-HAADF micrographs. In the case of bowtie antennas, with the identical approach, I calculate the Antenna wing width deviation. The obtained antenna deviations of both the bar and bowtie antennas are in Figure 25.

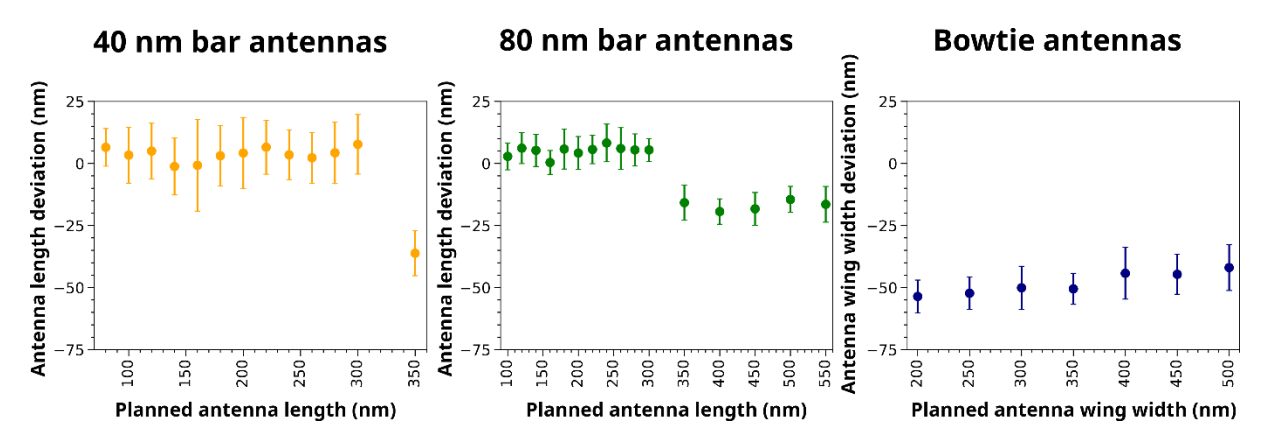


Figure 25: The bar antenna length deviation from the planned length and bowtie antenna wing width deviation from the planned wing width. The sudden transition from positive deviation to negative for bar antennas longer than 350 nm is not caused by the temporal instability of the ion beam. I believe it is a software issue, where for a certain critical nanostructure dimension or ratio of milled and unmilled areas, the milled pixel density is increased, which leads to an unintentionally increased milling of the antenna edges by the tail of the ion beam. This theory appears to be consistent, as all bowtie antennas (with their far larger ratio of milled and unmilled area) suffer from this phenomenon even more than the smaller bar antennas.

The bar antennas with a planned length below 350 nm were not much deviating from the desired size. Most of them were slightly larger than planned (by up to 8 nm). This is most probably caused by the redeposition of material, which deposits mainly on the protrusions of the surface, such as the fabricated antenna itself, and the residual grains. However, for the bar antennas longer than 350 nm, the length deviation suddenly increased and became negative, which means the fabricated antennas were far smaller than planned.

At first, I suspected that I might have accidentally changed either the stigmation or the focus values of the ion beam by nudging into the control panel buttons. However, such a change in the beam parameters would affect the width of bar antennas. When changing focus, the ion beam would spread a bit and both the length and width of the antenna would decrease. If the stigmator values were changed, the elliptical ion beam would mill one dimension more than the other, leading to the fabrication of wider and shorter antennas. The width of the bar antennas remained the same for antennas above 350 nm in length. Therefore, the issue must be caused by something else.

My second guess was, that the temporal instability of the ion beam might have changed the ion beam characteristics. This theory was disproved by the following facts. I fabricated 40 nm wide antennas first. After that, I followed with the fabrication of 80 nm wide bar antennas. If the issue was caused by temporal instability, it would have influenced the 80 nm wide antennas as well, as they were fabricated right after the 40 nm antennas which suffered the sudden drop in real length. Furthermore, the same sudden shift of the length deviation towards negative values was observed in 80 nm antennas as well.

Therefore, my final theory behind such a sudden increase in the antenna deviation is that it was caused by the Helios user interface software. When fabricating a batch of antennas, I had to

import a 24-bit bitmap of the structure. The software then computes the necessary ion dose for the structure milling, along with the density of beam positions, which will be milled. I believe that when the ratio of milled and unmilled areas exceeds a certain threshold, the density of milled spots increases, which leads to an increased milling of the antenna by the beam tail. This theory is consistent, as for the bowtie antennas, which have an even higher milled-to-unmilled area ratio, the antenna wing width deviation is higher as well. Interestingly, the other analysed antenna dimensions, the width of bar-shaped antennas and the gap size of bowtie antennas

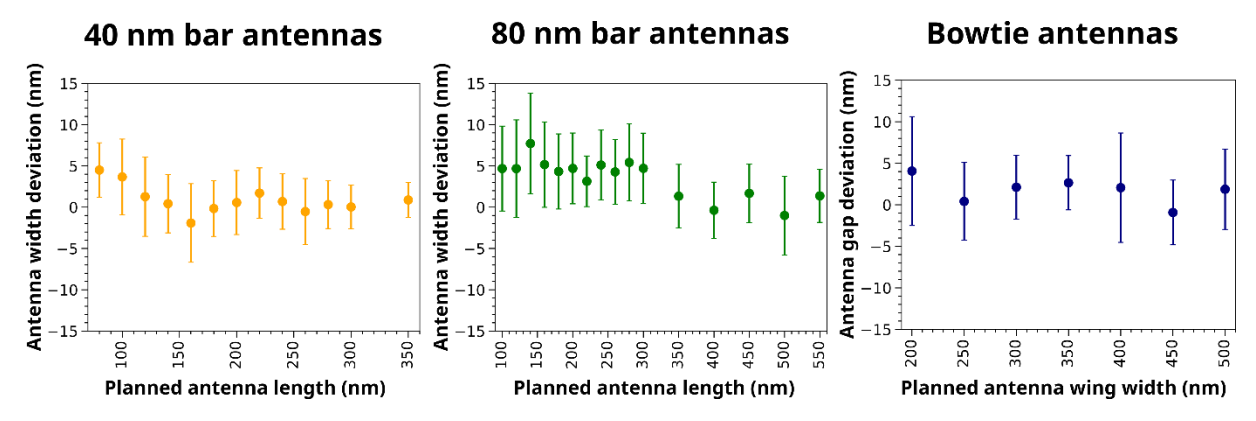


Figure 26: The bar antenna's average width deviation and the bowtie antenna gap width deviation. The planned widths for the bar antennas were 40 and 80 nm. The planned gap width in bowtie antennas was 20 nm. All of these deviations remained similar for all antenna lengths and bowtie wing widths.

remained similar for all bar antenna lengths and bowtie wing widths. Individual width and gap size deviations of various antennas are in Figure 26.

Later on, I also tried fabricating additional batches of bowtie antennas with a wing width from 550 to 700 nm with a step of 50 nm. Unfortunately, during the manipulation with the membrane after the lamella lift-out, the membrane ruptured, as can be seen in Figure 18. This prevented me from obtaining STEM micrographs needed for the size and fabrication yield evaluation of the additionally fabricated antennas.

3.2.3 Thickness of the bismuth antennas from EELS

As described in Section 2.3, it is possible, if a correct inelastic mean free path of an electron in the sample material is known, to measure the thickness of the sample by EELS. This allows me to create thickness maps of fabricated antennas and to evaluate the morphology of their edges, which can affect the plasmon resonances inside the antennas.

I extracted the thickness maps of bowtie antennas with wing widths of 620, 288 and 134 nm. For the inelastic mean free path of electrons with an energy of 120 keV in bismuth, I have used the value of 105 nm obtained from [103]. I used an inelastic mean free path of gold from the same source in my bachelor thesis and it was proved to be accurate [53]. Therefore, I consider the value for bismuth accurate as well. The thickness maps of the three bowtie antennas, along with thickness profiles spanning over their gaps are shown in Figure 27.

The thickness profiles reveal that the antenna edges are steep, uniform and nearly vertical, meaning that the unintentional milling of the antenna by the tails of the gaussian-shaped ion beam was minimal. The sloped edges of antenna gaps are caused by a redeposition, which is characteristic for FIB lithography of narrow features with a high aspect ratio [104]. Since the surface of the antenna is not affected by unintentional milling during the lithographic process, we can safely assume that the thickness of the antenna is equal to the thickness of the original

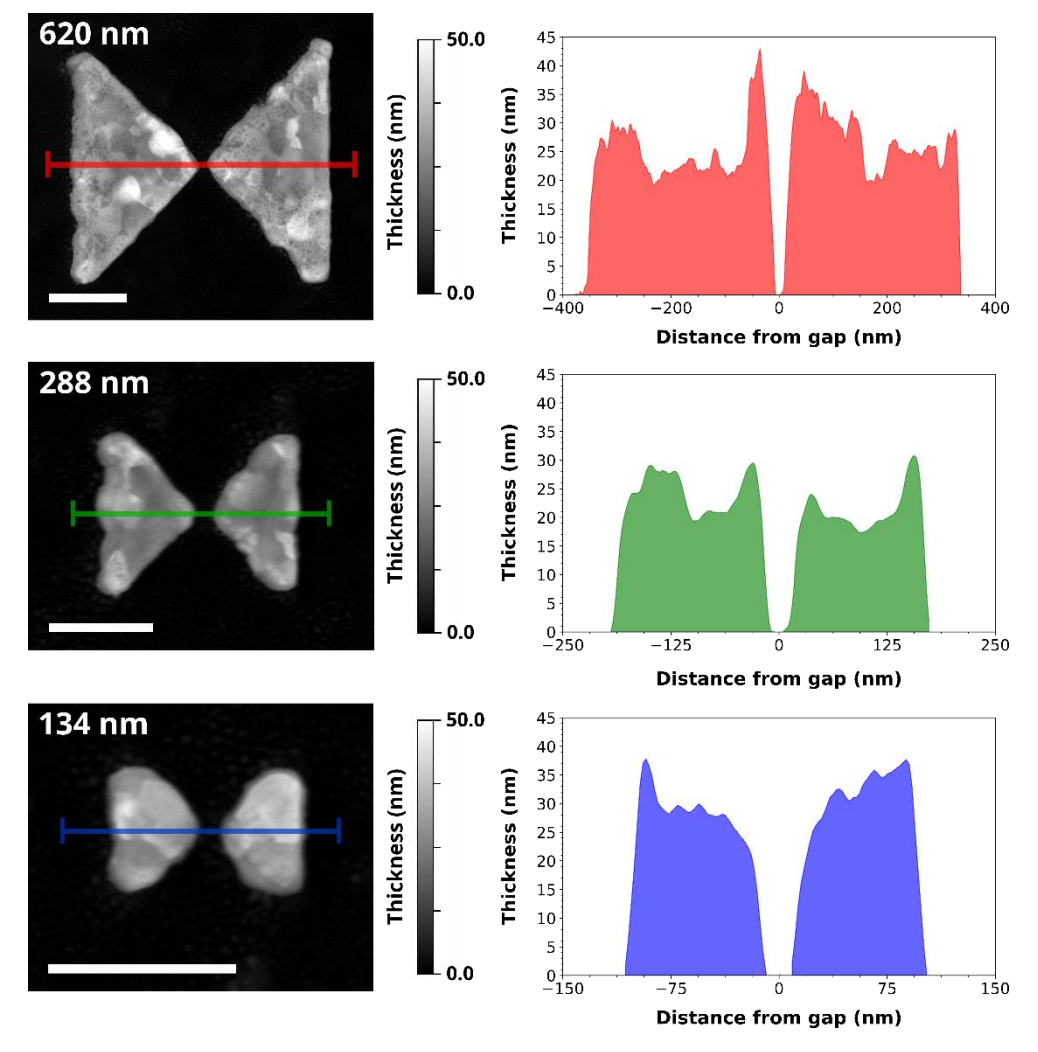


Figure 27: Thickness maps of bowtie antennas with wing widths of 620, 288 and 134 nm. The scale bars in all three maps correspond to 200 nm. The three coloured lines mark the distance and positions from which the thickness profiles of the antennas were extracted. The profiles were integrated over the line width of 3 pixels, which corresponds to a line width of 6 nm. The edges of all three antennas are nearly vertical, which means that the ion beam was well-focused and stigmatic, and that the used milling strategy was optimal. The gap edges are sloped, which can be attributed to redeposition, typical for lithography of narrow spaces. Furthermore, the antennas suffer from the high roughness of the bismuth layer.

bismuth layer. The layer thickness obtained from the thickness maps of the three antennas is (30 ± 5) nm, which is within the uncertainty interval of the thickness obtained from the lamella in Section 3.2.1.

Based on the thickness maps and profiles, I expect significant damping of plasmon peaks in the studied bismuth antennas caused by the high surface roughness of the antennas. In conclusion, for fabrication of bismuth antennas, the FIB lithography is an ideal technique and the quality of fabricated antennas is limited primarily by the morphology of the bismuth layer.

3.3 Plasmonic properties of fabricated bismuth antennas

The EELS measurement of the fabricated bismuth plasmonic antennas was done by Ing. Michal Horák, Ph.D. on the previously used FEI Titan (S)TEM microscope [67]. We used a monochromated electron beam with an energy of 120 keV [105]. For measuring the electron energy losses, we used the GIF Quantum spectroscope. The output of a typical EELS

measurement is the number of electrons which lost a certain energy at a certain position in the analysed area. I normalised the spectra by the intensity of the zero-loss-peak (ZLP). This way, the spectra are interpreted as a probability of certain energy loss. I subtracted the normalised background (loss probability spectra from the area of exposed SiN_x membrane) from the spectra of the analysed nanostructure. Upon this data processing, a loss probability of various excitations in the nanostructure is revealed, without any contributions from the supporting SiN_x membrane. To evaluate and compare the measured EEL spectra of the antennas, I fitted the observed loss probability peaks corresponding to individual plasmon resonances with Gaussian curves. To identify the measured EEL peaks and to match them to a corresponding plasmon mode, I made loss probability maps. Since the loss probability is proportional to the out-of-plane electric field, which is tied to the accumulated charge in the antenna, I can identify individual plasmon modes based on the spatial distribution of the loss probability. It should be noted, that in this chapter, when discussing the antenna length, I am referring to the actual length of the antenna obtained from STEM-HAADF micrographs of individual antennas and not the length planned during the FIB lithography.

3.3.1 Plasmonic properties of 40 nm bar antennas

First, I analysed the plasmonic behaviour of 40 nm bar antennas. I was able to observe and easily identify the longitudinal dipole mode in all 40 nm bar antennas. Further on, I observed a loss probability peak at higher energy as well. Although the energy of the peak was near the expected energy of a longitudinal quadrupole (LQ) mode, the loss probability map did not fit the typical pattern characteristic for the LQ mode. Probably, the second observed peak corresponds to a mix of LQ and higher-order modes, which are not distinguishable within the spectrum. For this reason, I compare and evaluate the plasmonic properties of 40 nm bar antennas only based on the clearly observable LD mode. The measured EEL spectrum, fitted curves along with the loss probability maps of both the LD plasmon mode and the multimodal assembly (MA) plasmon found in a 40 nm bar antenna with a length of 193 nm are in Figure 28.

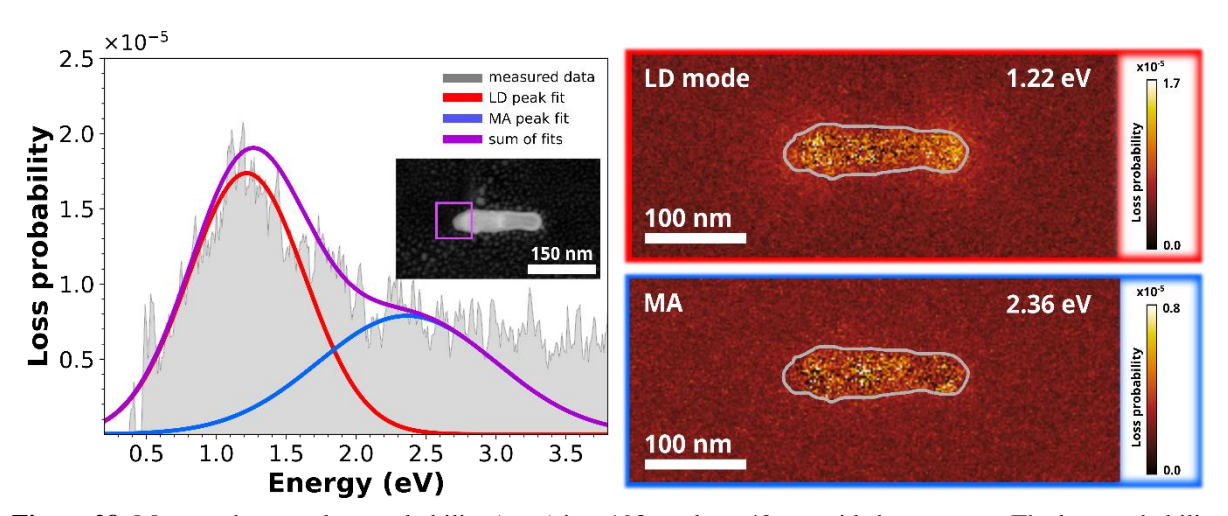


Figure 28: Measured energy loss probability (grey) in a 193 nm long 40 nm wide bar antenna. The loss probability map at energy of 1.22 eV reveals that the observed peak fitted by the red curve corresponds to the LD mode. The nature of the loss probability peak at 2.36 eV fitted with a blue curve is uncertain. The loss probability map at the energy of 2.36 eV shows a pattern which differs from a typical spatial distribution typical for LQ modes in bar antennas. The area of spectra integration is marked by the violet rectangle in the STEM-ADF micrograph of the antenna.

The measured loss probability spectra, along with the fitting curves corresponding to the LD plasmon mode and STEM-ADF micrographs of all investigated 40 nm bar antennas are in

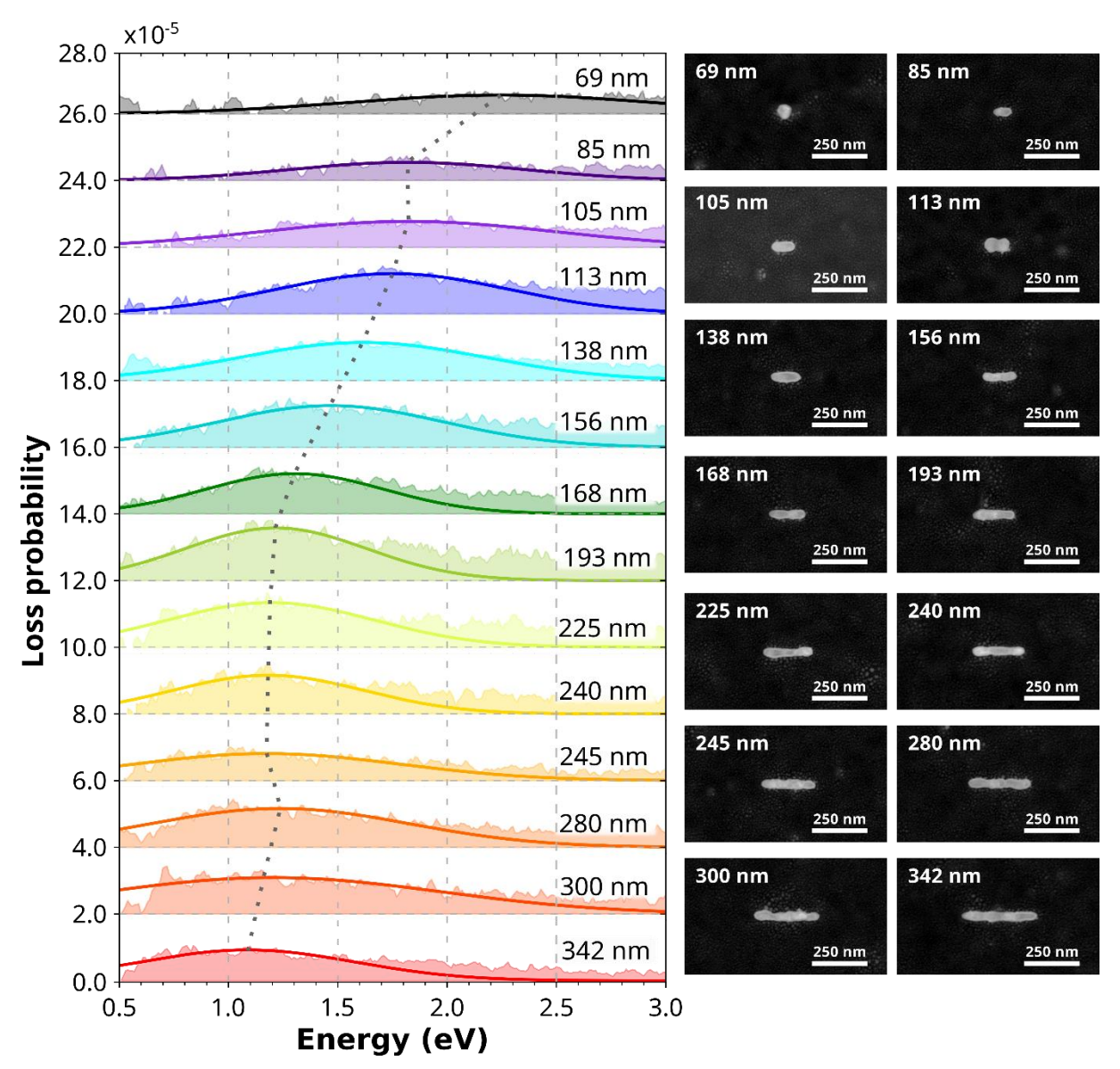


Figure 29: Measured loss probability spectra of 40 nm bar antennas (coloured) along with the fitting curves corresponding to the LD plasmon mode. The grey dotted line connects the maxima of curves fitted to LD plasmon peaks. On the right are STEM-ADF micrographs of all analysed antennas.

Figure 29. The observed plasmon peaks in 40 nm wide antennas are relatively wide. This is likely caused by the damping of the plasmon resonances connected to the shape imperfections and roughness of edges and antennas' surface. The energy of LD plasmon mode in 40 nm bar antennas spans from 1.09 eV in the case of an antenna with a real length of 342 nm, up to the energy of 2.24 eV for the shortest antenna with a length of 69 nm. The dependence of LD mode energy on the antenna length can be seen in Figure 30.

The loss probability of the LD mode is lowest for the antennas with a length below 110 nm, where the loss probability is below 10⁻⁵. The highest loss probability of the LD mode was observed for antennas with lengths from 110 nm to 240 nm (Figure 31). For longer antennas, the loss probabilities slowly start to drop again. Based on these observations, I believe that while the lower loss probabilities in smaller antennas are caused by the smaller volume of the antenna itself, for longer antennas, the positive impact of larger antenna volume is surpassed

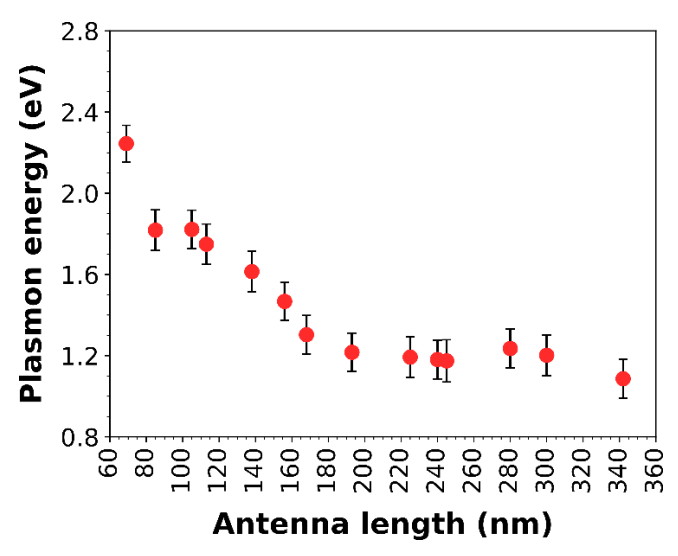


Figure 30: Energy of LD plasmons in 40 nm wide bar antennas. The highest LD plasmon energy found in the shortest 69 nm long antenna is 2.24 eV, which corresponds to the wavelength of 553 nm. The lowest LD plasmon energy of 1.09 eV found in the longest antenna corresponds to a wavelength of 1137 nm. Therefore, the 40 nm bar antennas are suitable for applications from near-IR to the visible part of the spectrum.

by the negative influence of damping of the resonance by a mix of ohmic losses and scatterings on the shape imperfections and on the rough edges and surface of the antennas.

Another parameter which can be used to evaluate the plasmonic behaviour of individual antennas is the Q factor, which is defined as the energy of the plasmon divided by the FWHM of the plasmon peak. The higher the Q factor, the less damped the system usually is. The Q factors of LD modes in studied 40 nm bar antennas are in Figure 31. For all antennas with length below 240 nm, the Q factor is similar. However, for longer antennas, the Q factor is slightly reduced.

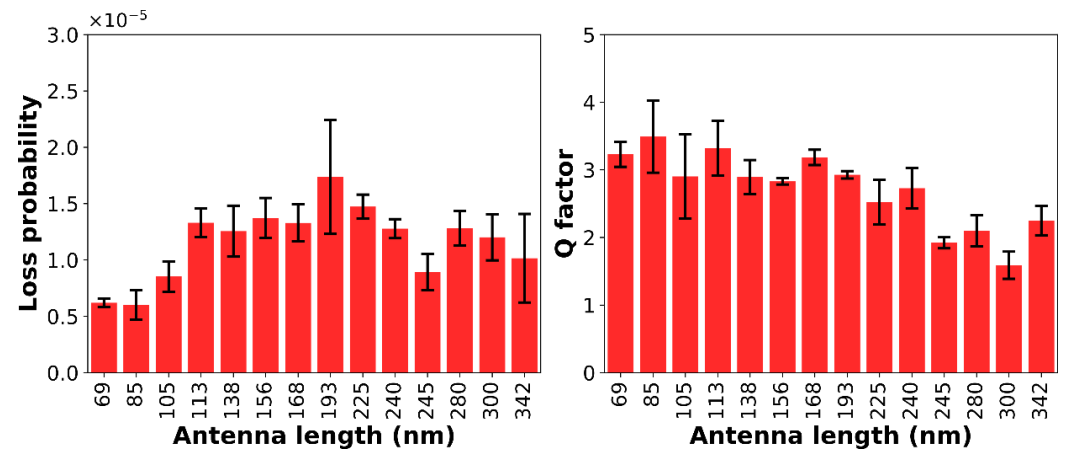


Figure 31: Loss probability maxima of LD plasmon resonant mode in 40 nm bar antennas along with their respective Q factors. Based on these graphs, the optimal antenna lengths are between 100 and 240 nm, for which the loss probability maxima are the highest. The Q factors are also among the highest for these antenna lengths as well.

In conclusion, the 40 nm bismuth bar antennas can be comfortably utilised in plasmonics. Ideally, the length of the antenna should be kept smaller, as the loss probability values, and Q factors tend to be higher for these dimensions. The best results were achieved for antennas

with lengths between 100 and 240 nm in length. For these antenna lengths, the LD plasmon mode energies span from 1.17 eV (wavelength of 1060 nm) to 1.82 eV (wavelength of 680 nm).

3.3.2 Plasmonic properties of 80 nm bar antennas

We further analysed the 80 nm wide bar antennas with lengths from 103 nm to 503 nm. When analysing the 80 nm bar antennas, I encountered a problem, where the background subtractions and removal of ZLP were not always ideal, and a narrow residual loss probability peak was present at energies below 0.5 eV. This peak does not correspond to any excitation in bismuth. To ease the fitting of the loss probability peaks at higher energies, I simply fitted the artefact peak with a gaussian curve and subtracted it from the measured EEL spectra. As long as the artefact is at significantly lower energies than the studied loss probability peak and does not interfere with the maxima of loss probability peaks, such subtraction does not affect the analysis of the data. For example, the measured EEL spectrum of the 459 nm long 80 nm bar antenna in Figure 32 contains an artefact. I subtracted the artefact peak and plotted both the raw data and data with the subtracted artefact. Since they fully overlap, the fitting and analysis of the loss probability peaks should not be affected by such artefact subtraction. Finally, based on the loss probability maps at energies of 0.85 eV and 1.72 eV in Figure 32, the loss probability peaks clearly correspond to the LD and LQ plasmon modes.

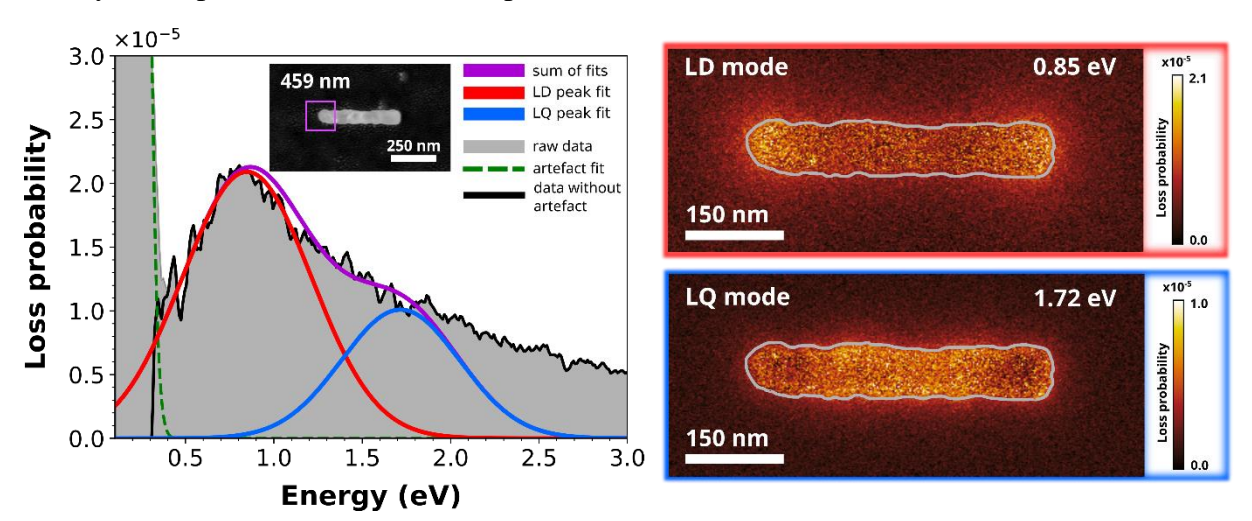


Figure 32: Measured EEL spectrum of a 459 nm long 80 nm wide bismuth bar antenna (coloured in gray). The loss probability spectrum contains an artefact peak at low energy. The dashed green line marks the subtracted curve fitted to the artefact peak. The red and blue curves fitted to the artefact-free loss spectrum (black line) correspond to the LD and LQ plasmon modes at energies of 0.85 and 1.72 eV. The loss probability maps mark the accumulated surface charge in the antenna for both plasmon modes. The area of spectra integration is marked by the violet rectangle in STEM-ADF micrograph of the antenna . Clearly, based on the perfect overlap of data after subtraction of artefact (black) and the raw data (grey), the removal of the artefact from raw data does not affect the loss probability of observed peaks, as long as the artefact does not directly overlap with the maximum of the loss probability peak.

In 80 nm bar antennas, I evaluate the plasmonic properties of the antennas based on both the LD and LQ modes. Measured EELS spectra with the curves fitted to the LD and LQ plasmon peaks, along with the STEM-ADF micrographs of all analysed 80 nm bar antennas are in Figure 33. The energy of the LD plasmons is between 0.80 eV for the 503 nm long antenna and 2.04 eV for the 103 nm long antenna. These energies correspond to the wavelength range from 1550 nm to 608 nm. The energy of the LQ plasmon mode goes from 1.41 eV for the longest antenna to 3.13 eV for the shortest analysed antenna. The corresponding wavelengths are from 879 nm to 396 nm. Therefore, only the LQ mode in the shortest analysed antenna was

in the UV region of the spectrum. The plasmon energies of both analysed modes plotted as a function of the antenna length are in Figure 34.

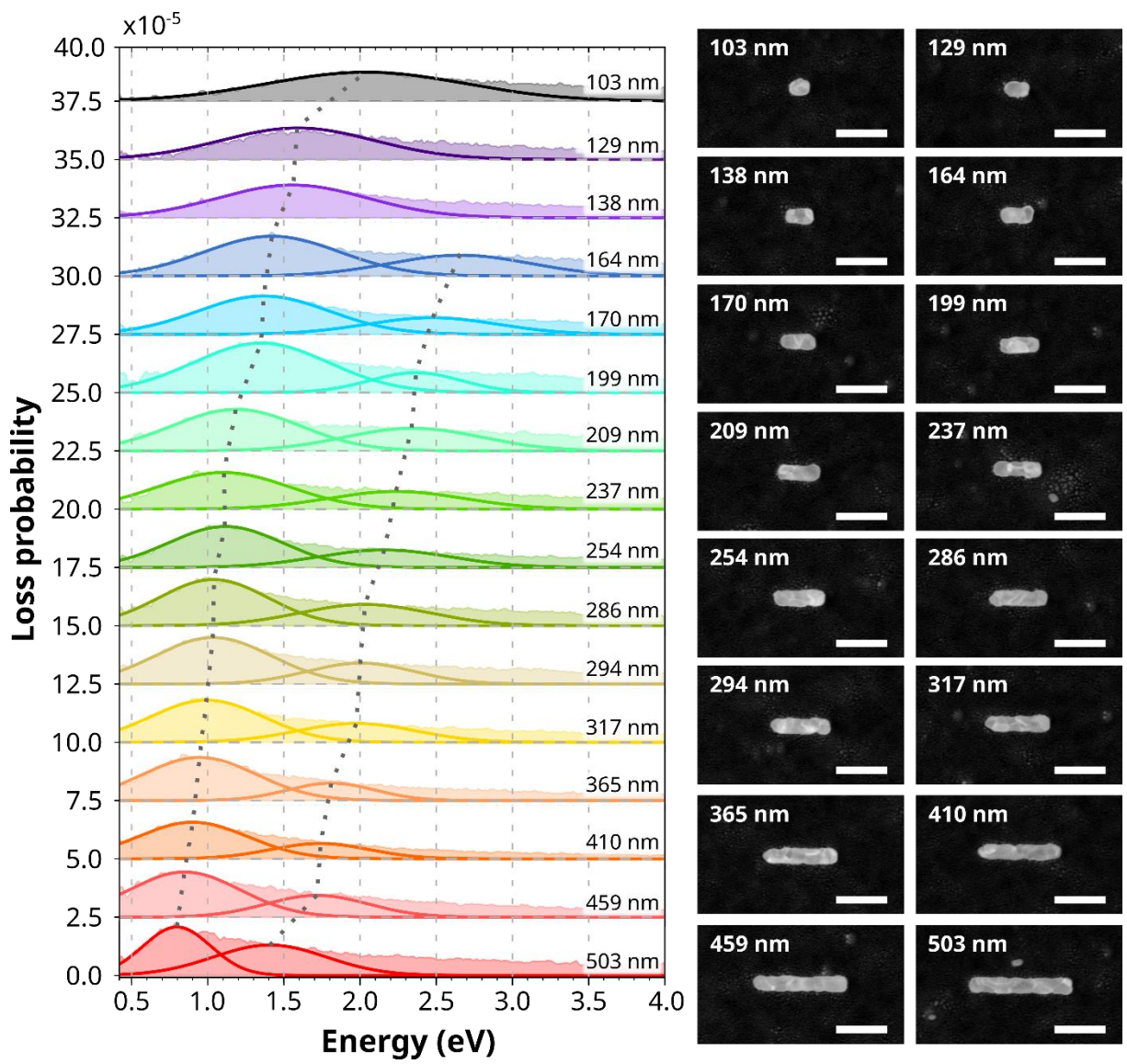


Figure 33: Measured loss probability spectra of 80 nm bar antennas (coloured) along with the fitting curves corresponding to the LD plasmon mode (at lower energies) and LQ plasmon mode (at higher energies). The two grey dotted lines connect maxima of curves fitted to the loss probability peaks of the two plasmon modes. On the right are STEM-ADF micrographs of all analysed antennas.

As expected, both plasmon resonant modes in 80 nm bar antennas have a higher loss probability compared to the loss probabilities of modes found in the 40 nm bar antennas. Although the exact values differ, the trends remain similar (Figure 35). For shorter antennas, the loss probabilities of LD modes are among the lowest. However, for antenna lengths above approximately 160 nm, the loss probability increases and remains similar for all the higher antenna lengths. For this reason, any antenna length above 160 nm can be considered optimal. The loss probabilities of the LQ modes follow a similar pattern.

The Q factors of the LD mode in 80 nm bar antennas are relatively constant for all antenna lengths and do not differ much (Figure 36). This is likely caused by the decreasing width of the

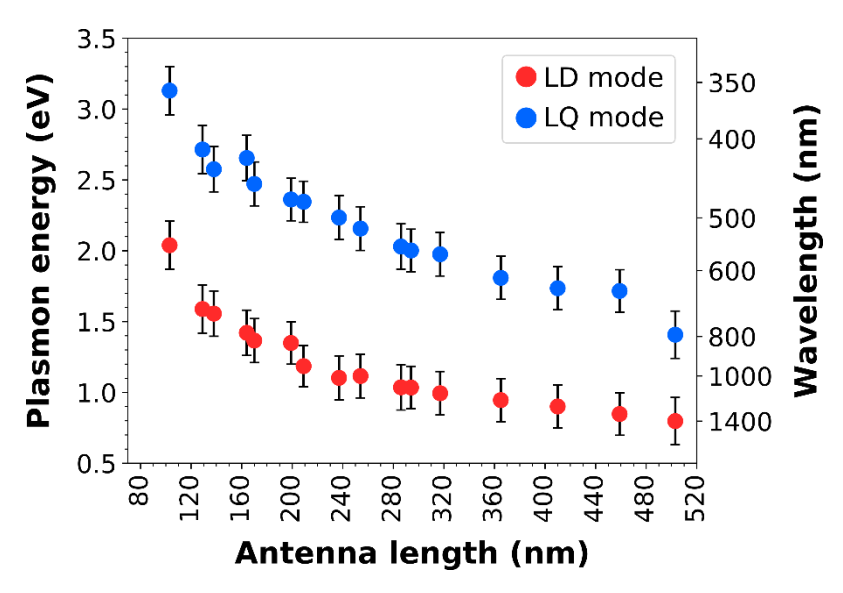


Figure 34: The energy of LD plasmons (red) and LQ plasmons (blue) in 80 nm bar antennas. The LD mode covers the wavelengths from 1400 nm to 607 nm. The LQ plasmon modes extend over the wavelength window from 879 nm to 396 nm. Based on the curve of the energy-antenna length dependence, the 80 nm bar antennas could be tuned to cover the entire visible region, as well as part of the near-IR region.

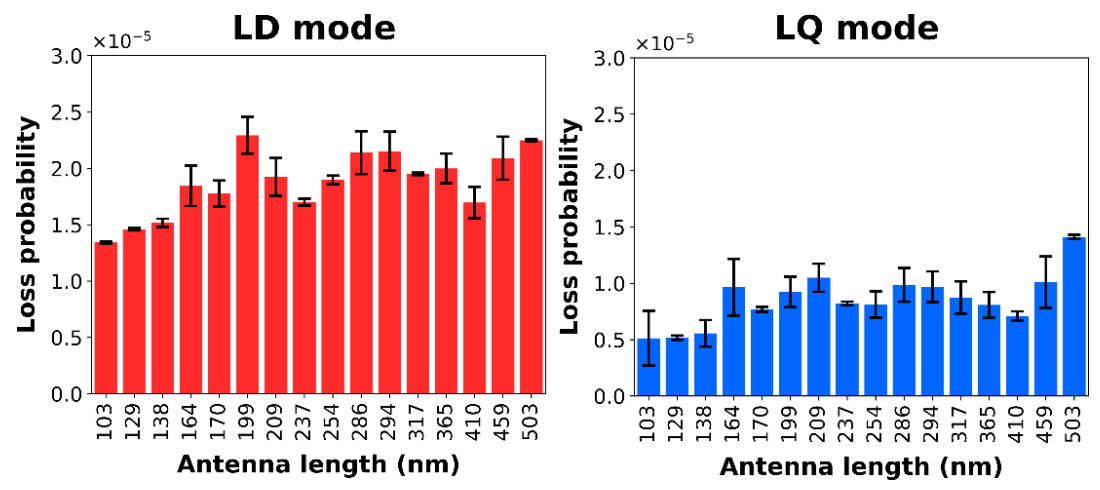


Figure 35: Loss probability maxima of LD plasmons (red) and LQ plasmons (blue) in 80 nm bar antennas. The loss probabilities of both modes remain similar for all antenna lengths above 160 nm.

plasmon peaks as the plasmon energy redshifts. For example, the FWHM of the LD mode peak in a 103 nm long antenna is approximately 1.3 eV, while for the 459 nm long antenna, the FWHM is only 0.72 eV. However, the Q factors of the LQ modes follow completely different trend. While for shorter antenna lengths, the Q factor is high, it lowers with increasing antenna length. Such behaviour is caused by the decreasing plasmon energy, while the peak width attributed to the damping of the plasmon resonances remains similar (around 0.7 eV) for all antenna lengths.

The bismuth 80 nm bar antennas prove to be viable for applications in plasmonics. While the tunability of the antennas allows us to cover the same wavelength window as the 40 nm bar antennas, the constant Q factors and higher loss probabilities across all antenna lengths make

the 80 nm bar antennas a better choice, especially when we take their easier fabrication into the consideration.

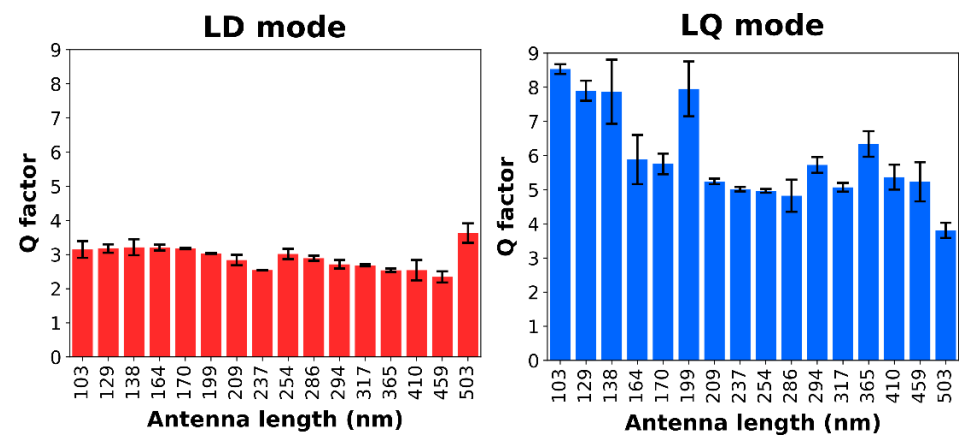


Figure 36: The Q factors of the LD plasmon modes (red) and LQ plasmon modes (blue) in 80 nm bar antennas. Although the LD mode Q factors are similarly high as those in 40 nm bar antennas, their more or less constant value for all antenna lengths means all antenna lengths are optimal. In the case of the LQ modes, the Q factors decrease as the antenna length increases. This is caused by the lower plasmon energy in longer antennas.

3.3.3 Plasmonic properties of bowtie antennas

We analysed the bowtie antennas with wing widths between 134 and 620 nm. For bowtie antennas, I evaluate the plasmonic properties based on the transverse dipole (TD) mode and the longitudinal dipole antibonding (LDA) mode. The measured loss probability maps along with the measured EEL spectra and curves fitted to the TD and LDA plasmon peaks in a bowtie antenna with a wing width of 436 nm are in Figure 37.

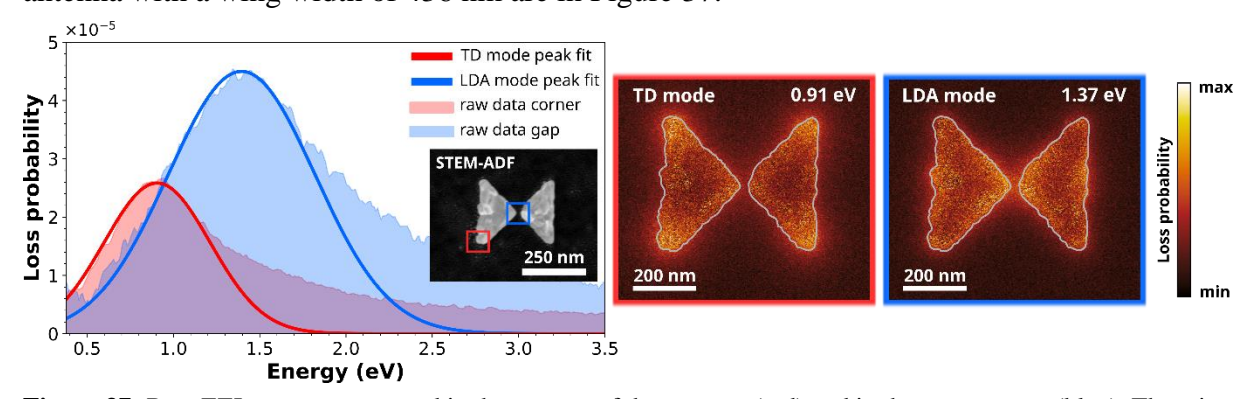


Figure 37: Raw EEL spectra measured in the corners of the antenna (red) and in the antenna gap (blue). The wing width of the antenna is 436 nm. The fitted red curve corresponds to the TD mode. The fitted blue curve corresponds to the LDA mode. The loss probability maps on the right mark the accumulated surface charge in the antenna for both plasmon modes. The loss probability maps prove both observed peaks to be the two plasmon modes typically observed in bowtie antennas. The antenna edges are marked by a grey line.

The measured EEL spectra along with the fitted curves corresponding to the TD and LDA plasmon modes of individual bowtie antennas with wing widths from 134 nm to 620 nm are in Figure 38. The LDA modes yield higher loss probability than the TD modes. Once again, the plasmon peaks of both modes are quite wide. Since the peak widths are similar in all antenna types and sizes, I believe the peak broadening is caused by the physical properties of the bismuth layer and not by irregularities of the bowtie antenna's shape.

The lowest observed energy of the TD plasmon mode is 0.76 eV in an antenna with a wing width of 620 nm. As the wing width of the antenna decreases, the energy of the TD plasmon

grows, ultimately reaching 1.63 eV for an antenna with a wing width of 134 nm. The energy window of the LDA mode is from 0.97 eV for the biggest antenna to 2.26 eV for the smallest, 134 nm antenna. The energies of both modes for each antenna size are in Figure 39.

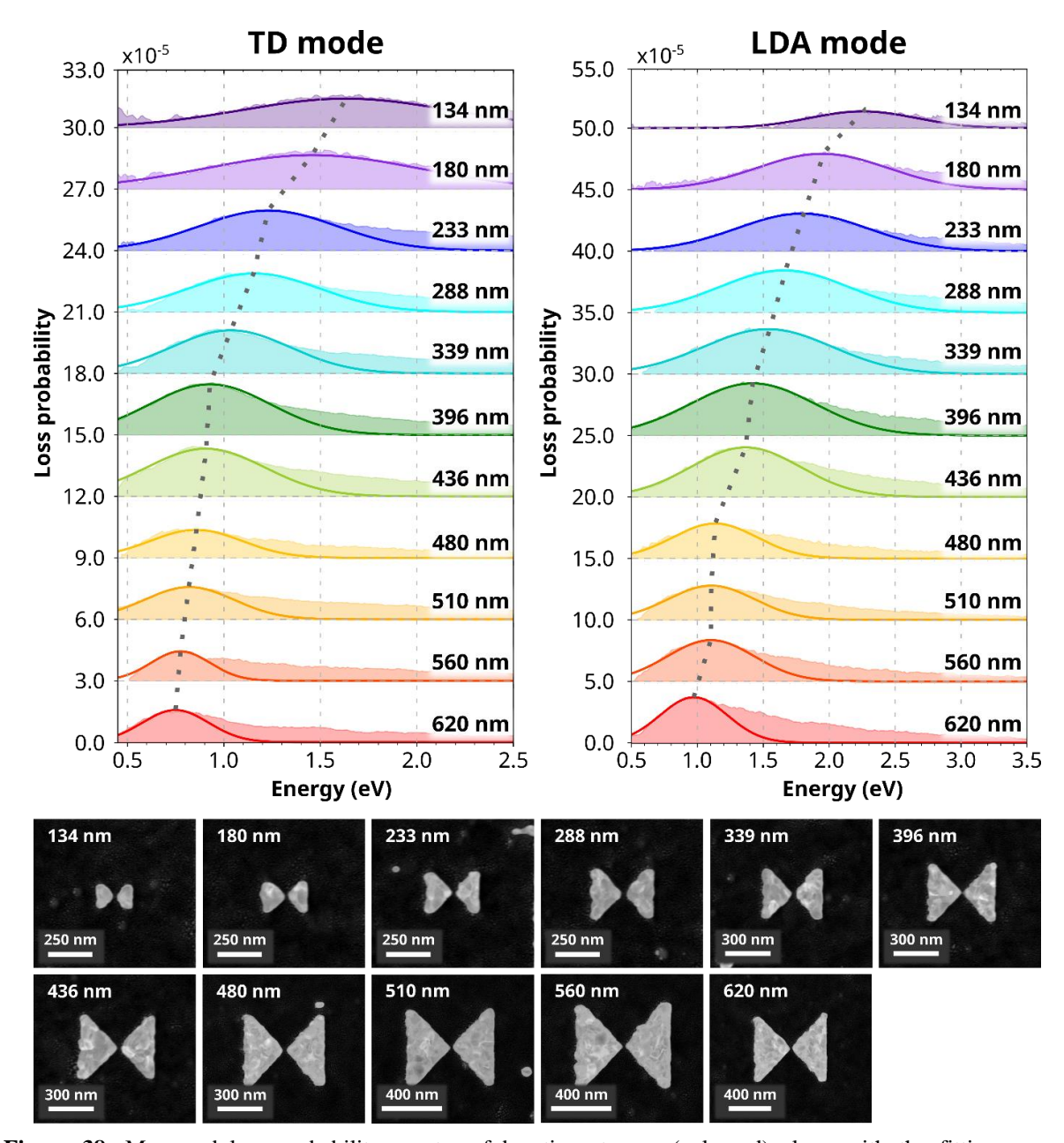


Figure 38: Measured loss probability spectra of bowtie antennas (coloured) along with the fitting curves corresponding to the TD plasmon mode (left) and LDA mode (right). The grey dotted line connects the maxima of curves fitted to LD plasmon peaks. Below the measured spectra are STEM-ADF micrographs of all analysed bowtie antennas.

The loss probabilities of the LDA plasmon modes in bowtie antennas were higher than the loss probabilities found in both the 40 nm and 80 nm bar antennas. Contrary to my expectations, the TD modes in bowtie antennas yield nearly identical loss probabilities as the LD modes in 80 nm bar antennas. The loss probabilities of both plasmon modes in bowtie antennas are in Figure 40.

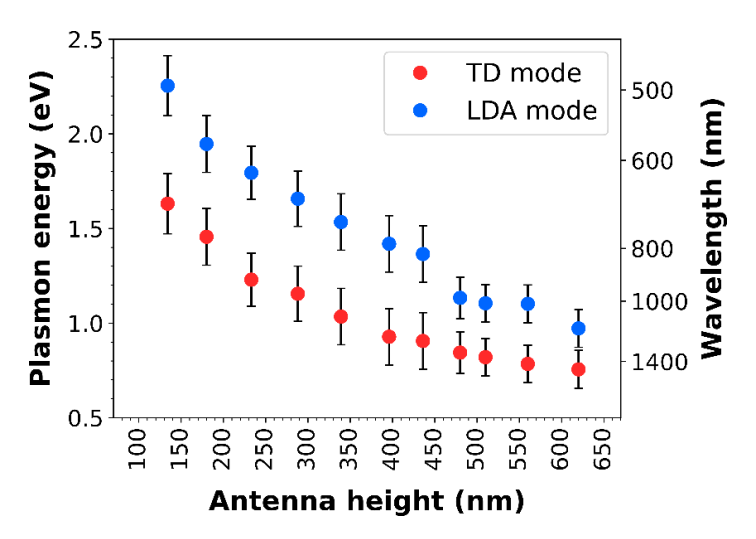


Figure 39: The energy of TD plasmons (red) and LDA plasmons (blue) in bowtie antennas. The TD mode covers the wavelengths from 1630 nm to 760 nm. The energy of LDA mode covers the wavelength window from 1280 nm to 548 nm. Based on these findings, the bismuth bowtie antennas are most suitable for applications in near-IR to visible part of electromagnetic spectrum.

A closer inspection of the loss probability trends in Figure 40 reveals that the loss probability of both the TD and LDA modes drops for bowtie antennas with wing widths larger than 480 nm. These antennas were planned to have a wing width above 500 nm. As noted in Section 3.2.2, the antennas in question were fabricated and analysed by STEM-EELS after the fabrication of smaller antennas (with a delay of approximately half a month). A possible cause behind their lower loss probability might be a partial oxidation of the bismuth layer in between the two fabrication processes, consequently leading to less conductive antennas. However, the plasmon peaks of antennas above 480 nm have lower peak width than the plasmon peaks found in antennas from the first fabrication attempt.

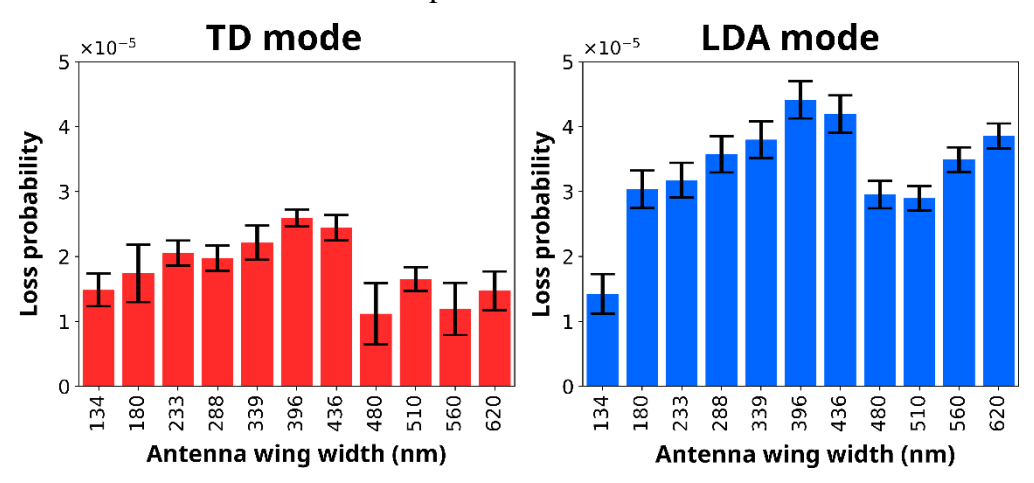


Figure 40: Loss probability of the TD (red) and LDA (blue) plasmon modes in bowtie antennas. Similarly to the bar antennas, the smaller antenna size leads to a smaller loss probability achieved. The loss probability of both the TD and LDA modes in bowties with wing width above 480 nm is smaller than that of the preceding smaller antennas.

In Figure 41, the Q factors of the TD mode in antennas with the wing width above 480 nm also exceed those of the smaller antennas. The Q factors of the LDA mode are slightly higher as well.

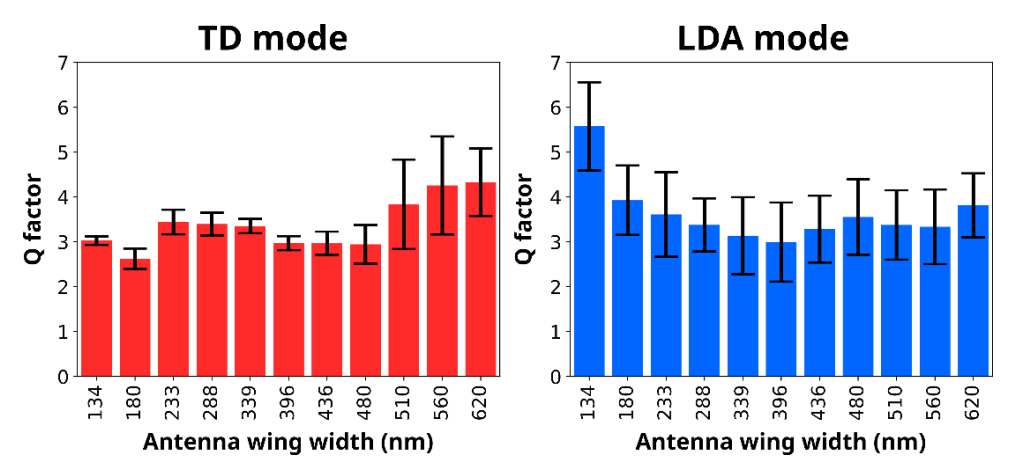


Figure 41: The Q factors of the TD plasmon (red) and LDA plasmon (blue) modes in bowtie antennas. With the exception of the antennas with wing width above 480 nm in the case of the TD modes and just the 134 nm antenna in the case of the LDA mode, the Q factors remain similar for all antenna lengths.

3.3.4 Comparison of bismuth and gold bowtie antennas

Based on the results discussed above, I can confidently conclude that bismuth nanoantennas exhibit plasmon resonances. However, to fully evaluate bismuth's suitability for possible plasmonic applications, a comparison with the most frequently used plasmonic material, gold, is needed. I compared the observed plasmon peaks of the bismuth bowtie antenna to those found in a gold bowtie antenna fabricated within my bachelor thesis [53]. The gold bowtie antenna was fabricated from a gold polycrystalline layer deposited by ion-beam-assisted sputtering at the deposition rate of 1 Ås⁻¹. The thickness of the gold layer was approximately 33 nm. The gold antenna has a wing width of 439 nm and a gap width of 39.5 nm. I compared it to a bismuth antenna with a wing width of 436 nm and a gap width of 24 nm. The nearly identical dimensions of the two antennas should eliminate the influence of the antenna size on the plasmon resonances in the two materials. The wider gap of the gold antenna should affect only the LDA mode and cause a blue-shift. The measured loss probability peaks and fitted curves corresponding to the TD and LDA plasmon peaks found in the bismuth and gold antenna are in

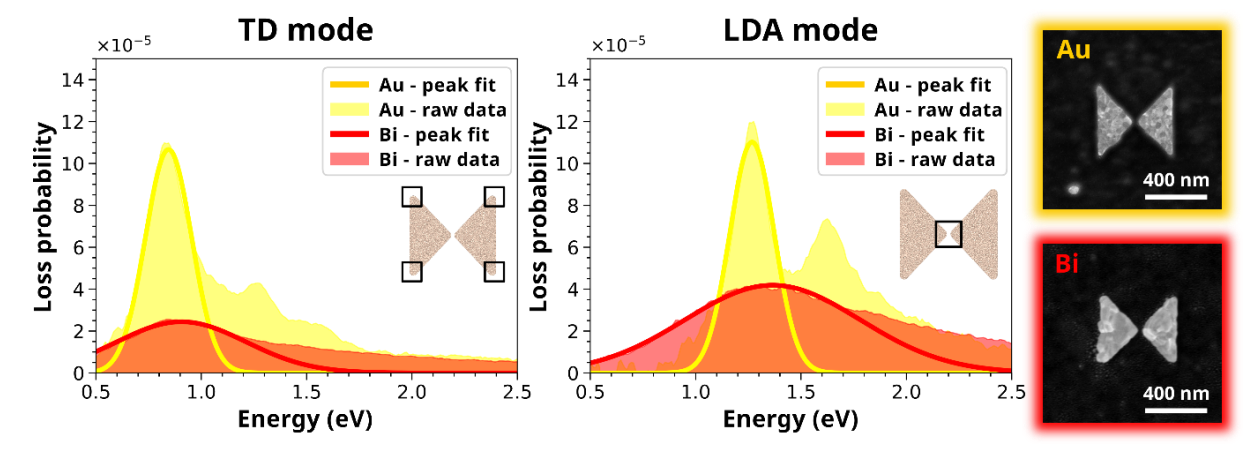


Figure 42: The measured loss probability peaks and fitted curves corresponding to the TD and LDA plasmon modes in gold (yellow) and bismuth (red) bowtie antennas. The wing width of the bismuth antenna is 436 nm and the gap is 24 nm wide. The wing width of the gold antenna is 439 nm and the gap is 39.5 nm wide. The STEM-ADF micrographs of both antennas are on the right. Both plasmon peaks in bismuth antennas are wider and yield a lower loss probability compared to plasmon peaks of the gold antenna. These findings are in agreement with theoretically calculated EEL spectra in Figure 8.

Figure 42. The energy of both the TD and LDA plasmon modes in the bismuth bowtie antennas appear to be similar to those found in the gold antenna. In agreement with the EELS spectra theoretically calculated in Figure 8, the bismuth TD and LDA plasmon peaks exhibit a 77% and 62% reduction in loss probability, respectively, compared to those of gold. Furthermore, the loss probability peaks are broader as well.

The similar plasmon energies in the bismuth antenna might mean the plasmon energies for other bowtie wing widths fabricated from bismuth and gold layers might be comparable as well. To analyse the possible similar plasmonic properties of the two materials, I compared the dependence of the plasmon energy on the reciprocal wing width of bismuth bowtie antennas to the dependence of gold bowtie antennas fabricated by Ing. Michal Horák, Ph.D. in his dissertation thesis [4]. The dependencies of the plasmon energy on the reciprocal antenna wing width of gold and bismuth bowties in Figure 43 overlap, therefore, in plasmonic applications, bismuth can be a cost-effective alternative to gold. Furthermore, the energy limit of gold for plasmonic applications is around 2.3 eV. At energies above 2.3 eV, a strong damping of plasmon resonances appears. The damping induced by strong interband transitions limits the use of gold for plasmonic applications at higher energies [108]. Based on the observed Q factors and plasmon peaks in Section 3.3.3, bismuth is not exhibiting such damping. Furthermore, band transitions in a material are manifested by peaks in the imaginary part of the dielectric function. Since there are not any peaks in the imaginary part of the bismuth dielectric function above 2.3 eV, bismuth is a safe choice for plasmonics at higher energies [63].

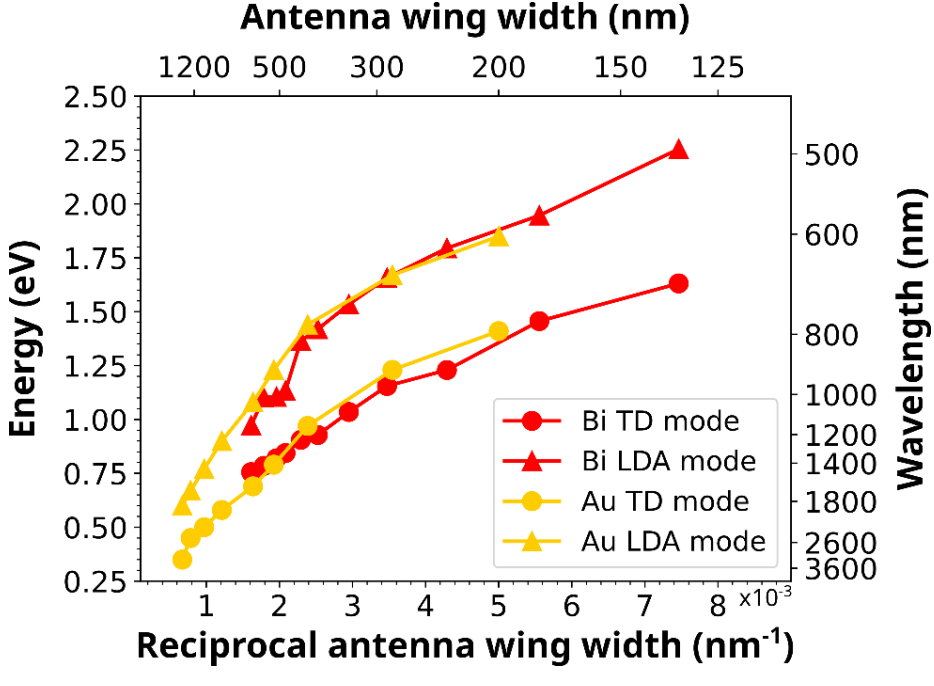


Figure 43: The dependence of the TD plasmon (circles) and LDA plasmon (triangles) energy on the reciprocal antenna wing width in bismuth (red) and gold (yellow) bowtie antennas. The dependence for gold was taken from [4]. The overlapping dependencies marks that gold can be replaced by far cheaper bismuth antennas.

In conclusion, bismuth appears to be a significantly cheaper alternative to gold. The range of plasmon energies in bismuth antennas can be extended below 0.6 eV with larger bismuth nanostructures. Although reaching the higher plasmon energies above 2.25 eV is not limited by the optical properties of bismuth itself, it is conditioned by the minimal fabricable size of bismuth nanostructures.

3.3.5 Influence of temperature on plasmon resonances in bismuth

The changes in the relative concentrations of electrons and holes along with an increase of their mobilities in bismuth monocrystalline layers [106] and polycrystalline bismuth nanowires [107] observed at low temperatures, awakened my curiosity. The temperature-induced changes in conductivity might affect the plasmon resonances in bismuth plasmonic antennas as well. For this reason, we measured the EEL spectra of a bowtie antenna with a wing width of 339 nm in-situ at temperatures of 293 K and 100 K. The STEM-ADF micrographs of the antenna at both temperatures, along with the measured ZLP and fitting curves corresponding to the TD and LDA plasmons are in Figure 44.

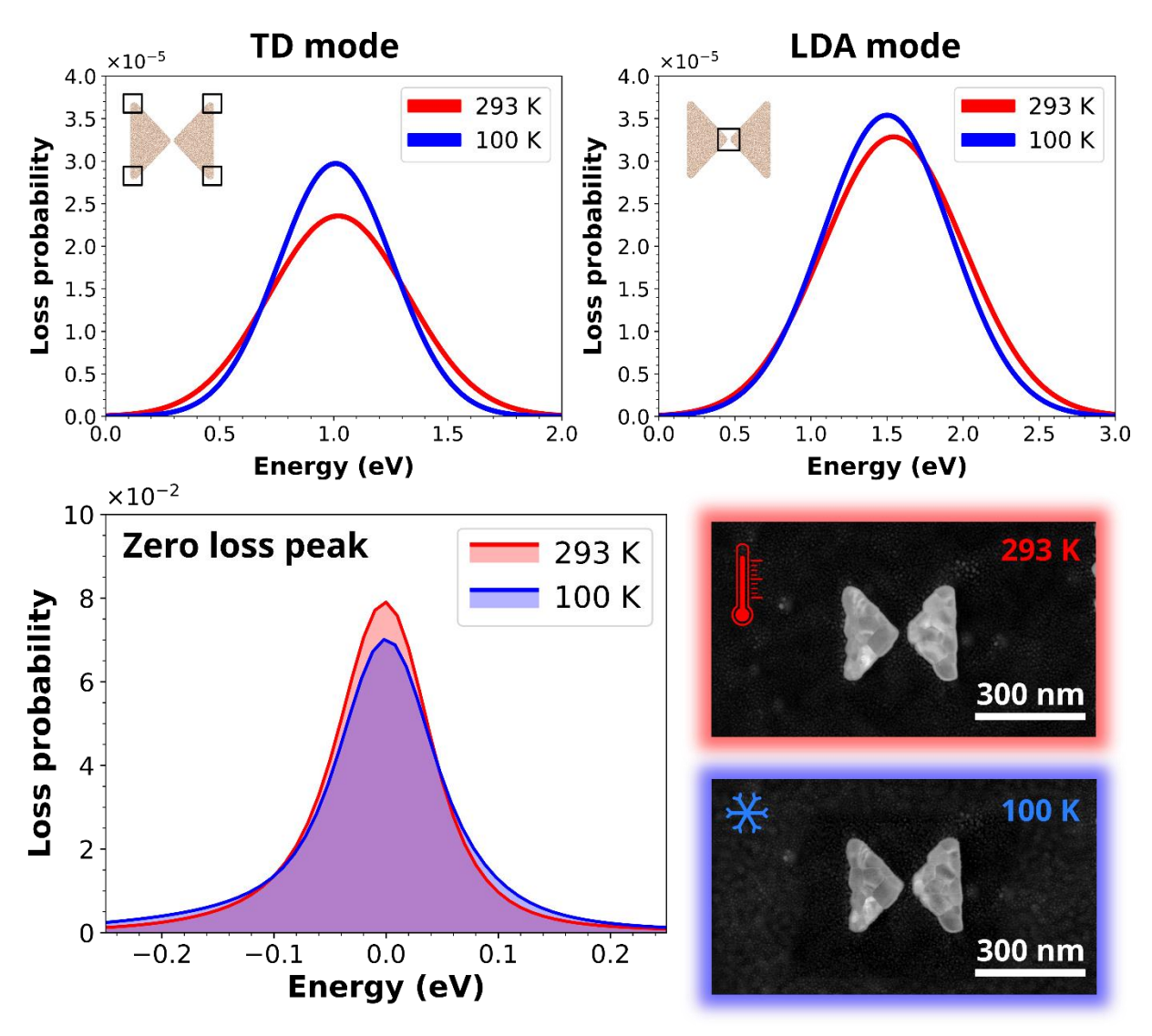


Figure 44: At the top are fitted curves corresponding to the TD and LDA plasmon modes at 100 K (blue) and 293 K (red). The areas from which were integrated the EEL spectra are marked on the antenna miniature. The lower temperature increased the loss probability of both plasmon peaks and reduced the peak width. At the bottom are ZLPs for both temperatures measured from the same area on the SiN_x membrane. The ZLP measured at 100 K is wider than the ZLP measured at 293 K. In the right bottom corner are the STEM-ADF micrographs of the antenna obtained at both temperatures. A slight change in contrast in the antenna grains is visible at 100 K.

Both the TD and LDA plasmon peaks in Figure 44 measured at 100 K had a higher loss probability. In the case of the TD mode, the loss probability increased from 2.36·10⁻⁰⁵

at 293 K to $2.97\cdot10^{-05}$ at 100 K. For the LDA mode, the loss probability increased less significantly from $3.29\cdot10^{-05}$ at 293 K to $3.54\cdot10^{-05}$ at 100 K. Further on, the lower temperature led to a reduced peak width. In the case of the TD mode, the peak width lowered by 0.1 eV, while for the LDA mode, the peak width decreased by 0.08 eV. The reduction of plasmon peak width at the lower temperature is not caused by an instability or inaccuracy of the instrument, since the ZLP measured at 100 K is broader than the ZLP at room temperature measured at the same area on the SiN_x membrane. At room temperature, the FWHM of ZLP was (0.08 ± 0.01) eV and at 100 K, the FWHM of ZLP was (0.10 ± 0.01) eV.

The increased loss probability and reduced width of plasmon peaks at the lower temperature are in disagreement with both aforementioned studies, which reported an increased resistivity at low temperatures, typical for semimetals like bismuth. Our findings suggest a different behaviour, typical for regular metals, where the decreasing temperature leads to a lower resistivity, and consequently to a smaller plasmon damping. Therefore, based on this experiment, it appears that our bismuth layer retains the metallic character and supports plasmon resonances even at lower temperatures (in our case at 100 K).

Nevertheless, a deeper study of the plasmonic behaviour of multiple antennas, ideally at even lower temperatures, would be needed before drawing more conclusions. However, such a detailed study is beyond the scope of this work.

3.4 Preparation of bismuth nanoparticles

3.4.1 Chemical synthesis

Based on the findings in chapter 2.6, I decided to synthesise bismuth nanoparticles by pyrolysis of Bi(CH₃COO)₃ (bismuth acetate) in a solution of tetra ethylene glycol (TEG) with added polyvinylpyrrolidone (PVP) acting as a surfactant, as described in [100]. The TEG serves primarily as a medium allowing heat transfer. I used a PVP with molecular weight $M_w = 40$.

The chemical reactions during the pyrolysis are schematically depicted in Figure 45. During the pyrolysis, first, the bismuth acetate undergoes a thermal decomposition, where it decomposes into a Bi³⁺ ion and three acetic groups. The positive bismuth ion then bonds with the oxygen atom in the amide group of PVP. The bismuth atoms with attached ligands start to form bismuth clusters through coalescence with other bismuth-ligand groups. When a sufficiently high temperature is achieved, the bismuth melts and liquid bismuth nanodroplets with protective ligand shells are formed in the solution. If the solution is suddenly cooled down, the nanodroplets remain spherical and solidify into monocrystalline nanoparticles.

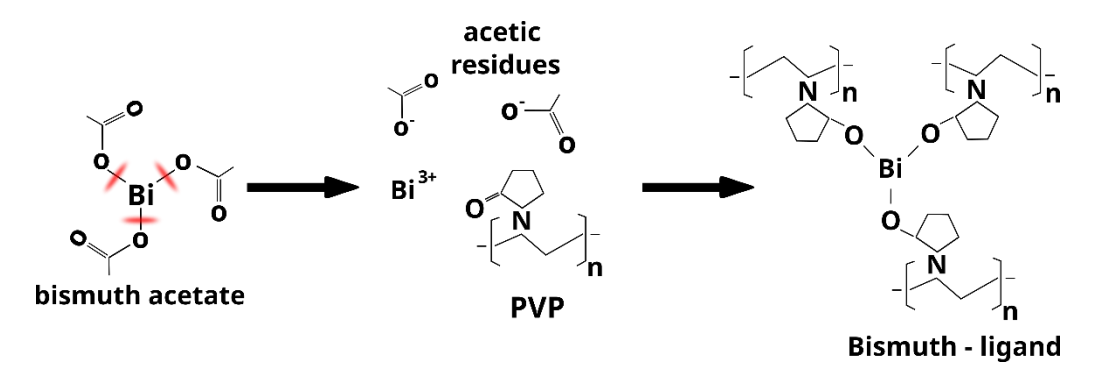
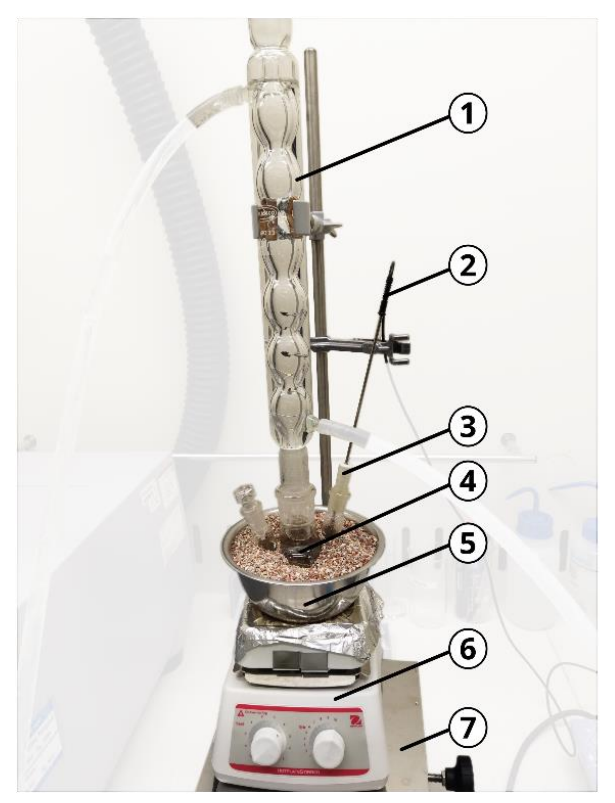


Figure 45: Schema of chemical reactions during the pyrolysis. The bismuth acetate thermally decomposes into Bi³⁺ ion and three acetic groups. The bismuth ion then bonds with the oxygen atom in the amide group of PVP. These bismuth-ligand groups then form clusters which then further grow into nanoparticles.

The apparatus used for the synthesis is shown in Figure 46. It consists of an adjustable stand, which allows fast removal of the reactor vial at the end of the pyrolysis. A magnetic stirring hotplate, generously lent to me by Ing. Ivana Pilátová, CSc., was placed on top of the stand. On the hotplate was a steel bowl with a reactor vial buried in a sand bath. The sand bath is crucial for increasing the maximum achievable temperature. Without it, the temperature needed for the melting of bismuth would not be achieved. A thermometer was inserted into the reactor through a makeshift rubber bushing and a reflux tube was connected to the reactor. The vapours created during the pyrolysis condense on the water-cooled sides of the reflux and are returned into the reaction vial, keeping the concentrations of reagents moreless the same throughout the synthesis.



- 1 Reflux with constant water flow
- (2) Thermometer
- 3 Makeshift rubber bushing
- (4) Reactor vial
- (5) Steel bowl with a sand bath
- 6 Hotplate with magnetic stirrer
- 7 Adjustable stand

Figure 46: The apparatus used for the synthesis. The reflux allows condensation of created vapours and returns them back into the reactor vial. The temperature of the solution was measured by a thermometer inserted into the reactor vial through a rubber bushing. The sand bath increases the thermal conduction and allows for reaching higher temperatures. The magnetic stirring hotplate stirred the solution and heated the reactor vial. The rotary knobs controlling the stirring rate and heating temperature are marked by unitless scales from 0 to 10 and do not allow accurate control of the synthesis parameters.

A typical synthesis consisted of the following steps: I poured 30 ml of TEG into a reactor glass vial and added an appropriate amount of bismuth acetate along with 0.3 g PVP. I used the magnetic stirrer to dissolve the PVP and bismuth acetate in the solvent before continuing with the synthesis. It should be noted, that both the bismuth acetate and PVP are hygroscopic. Therefore, their exposure to air should be limited as much as possible. After the PVP and bismuth acetate were dissolved, I started heating and stirring the solution until a temperature of 290 °C was achieved. Upon reaching the temperature, I maintained the temperature constant and kept stirring the solution for another 10 minutes. After that, I quickly removed the reactor vial from the hot sand bath and poured the solution into a vial with 125 ml of 4°C methanol.

The abrupt drop in temperature ensures that the liquid bismuth droplets solidify into round monocrystalline nanoparticles [100].

During the synthesis, the colour of the solution changes significantly. The colour change can be attributed to the reaction events in the mixture. In the beginning, the solution was transparent. When the temperature of the solution reaches 160 °C, the mixture becomes yellow and continually darkens. It necessarily means that the thermal decomposition of bismuth acetate starts when the temperature is approximately 160 °C. At 180 °C, the solution becomes suddenly orange and with increasing temperature slowly turns dark brown, ultimately becoming dark black at temperatures above 220 °C. I believe that the first liquid bismuth nanodroplets start to form at temperatures above 180 °C. This would mean, that the melting temperature of bismuth nanoparticles is significantly lower than the temperature of bulk bismuth. The decrease in melting temperature caused by the smaller nanoparticle diameter is a well-studied phenomenon and for bismuth nanoparticles, the melting temperature was theoretically predicted to be higher than 200 °C [109]. However, I managed to synthesise spherical bismuth nanoparticles using ethylene glycol (EG) instead of TEG. The nanoparticles synthesised in EG are in Figure 47. Ethylene glycol has a boiling temperature of 196 °C, which means the solution cannot reach a temperature higher than that. Since the nanoparticles synthesised in EG were spherical, the bismuth in the solution was in the form of liquid nanodroplets and solidified only after cooling the solution in cold methanol. Therefore, the melting temperature of the bismuth nanoparticles is below 196 °C, contrary to the claims in the literature. Beside the nanoparticles, large bismuth polycrystals with size in the order of micrometres were present as well, meaning that the lower achieved temperature, along with the EG as the solvent resulted in a lower yield of nanoparticles. For this reason, all the following syntheses were conducted using TEG as the solvent.

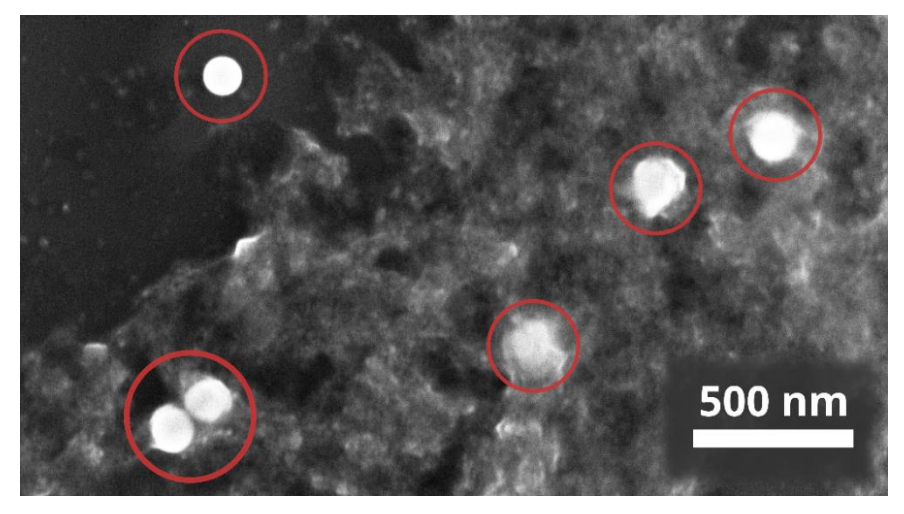


Figure 47: SEM micrograph (the collected signal comes from secondary electrons) of bismuth nanoparticles synthesised in EG. The nanoparticles are marked by red circles. Unfortunately, most of them were covered by a thick layer of polymeric residues created during the synthesis. These residues were present in the solutions of TEG as well. These residue films can be partially removed by cleaning the sample in oxygen-argon plasma.

To obtain nanoparticles with different sizes, I synthesised four batches of nanoparticles, with different amounts of bismuth acetate ($m_{\rm Bi}$) and different stirring rates listed in Table 1. A higher stirring rate and a smaller amount of bismuth acetate should result in smaller nanoparticles [100]. Unfortunately, the stirring rate could not be controlled directly on the hotplate because the rotary buttons have a unitless scale from 0 to 10, meaning that the stirring rate cannot be quantified.

Table 1: The mass of bismuth acetate and stirring rates used for the synthesis of four synthesised colloids. The stirring rate could be set by a rotary button with a unitless scale from 0 to 10.

Batch name	$m_{\mathrm{Bi}}\left(\mathbf{g}\right)$	Stirring rate
#1	0.150	10.0
#2	0.300	5.0
#3	0.225	7.5
#4	0.375	2.5

The size distributions of each synthesised batch of nanoparticles are in Figure 48. The size distribution depends on how fast the solution is cooled down after the synthesis. For example, after synthesising batch #3, I managed to pour the solution into the cold methanol within one minute. For the other batches, it took me several minutes before I could pour the hot solution into the methanol. All of the affected batches have a wider distribution of their size. Furthermore, it appears that the mean nanoparticle diameter is around 40 nm for all different tested amounts of bismuth acetate and stirring rates used.

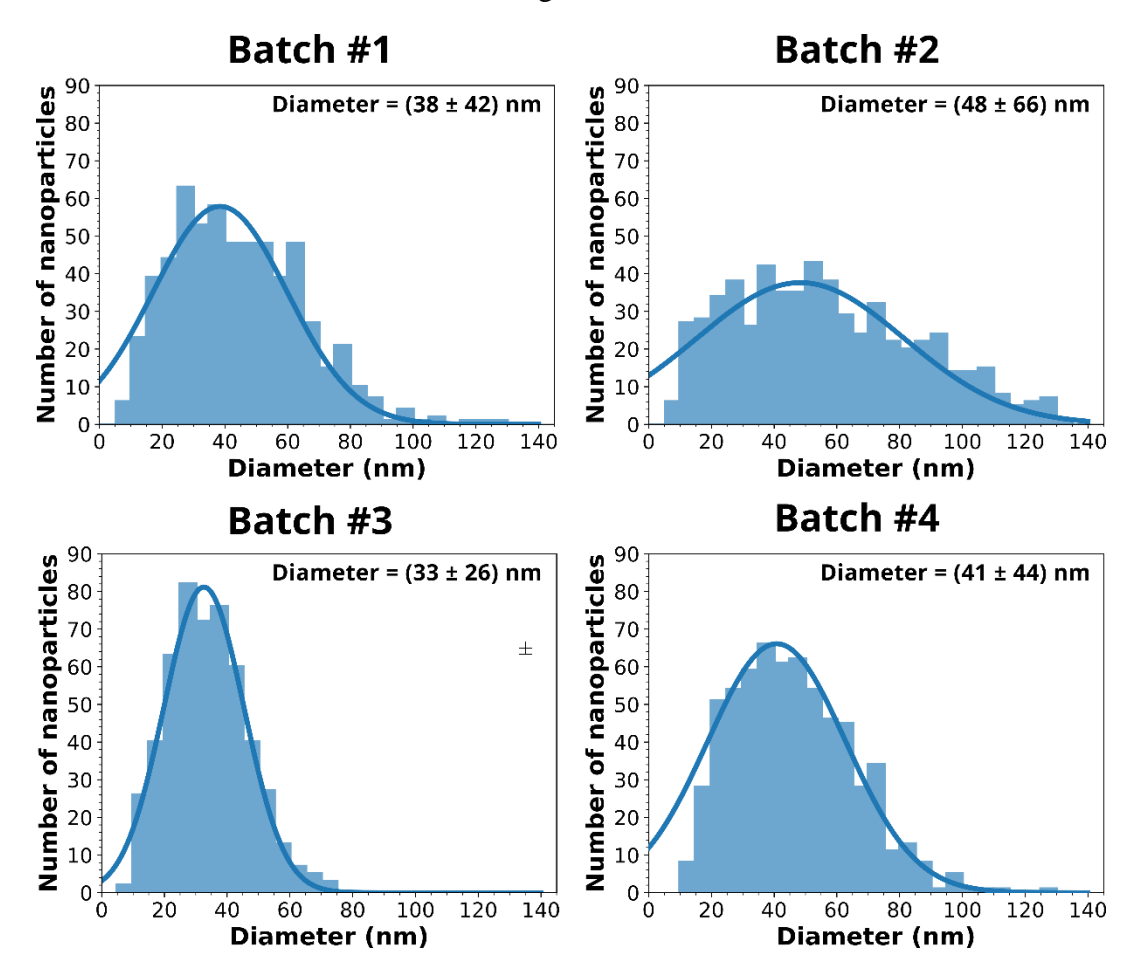


Figure 48: Distributions of the nanoparticles' diameters for each synthesised batch along with the fitted gaussian curves used for the evaluation of the mean diameter and its deviation. It appears that the mean nanoparticle size is around 40 nm for all amounts of bismuth acetate and the stirring rates used. However, the distribution spread is heavily affected by how fast the solution was cooled down. The batch #3, cooled within only one minute after the synthesis, exhibits the narrowest size distribution with a diameter deviation below 30 nm.

To verify that the nanoparticles are made of bismuth I used STEM-EDX. The elemental maps of bismuth nanoparticles are in Figure 49. The edges of nanoparticles are covered by an oxygen layer. This oxygen layer is not a bismuth oxide, as one would expect, but a layer of ligands held on the nanoparticle's surface by covalent oxygen-bismuth bonds. This is verified by the presence of nitrogen, which is a part of the amide group in PVP-based ligands.

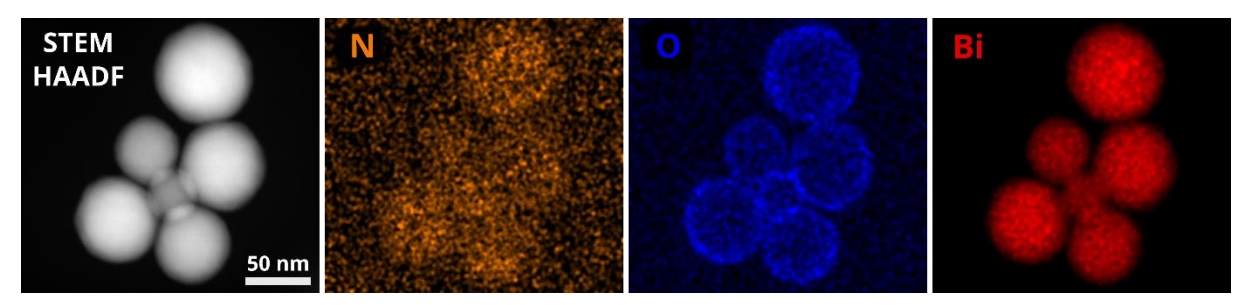


Figure 49: A STEM-HAADF micrograph and elemental maps of bismuth nanoparticles on carbon membrane TEM grid. The bismuth nanoparticles are covered by a layer of ligands, which contain oxygen and nitrogen in the amide group. We can rule out the possibility that the nanoparticle is made of bismuth oxide based on the overlap of the oxygen and nitrogen maps.

I studied the crystallography of synthesised nanoparticles by selected-area electron diffraction (SAED) and high-resolution transmission electron microscopy (HR TEM). Based on the diffraction pattern and HR TEM micrograph in Figure 50, the bismuth nanoparticles are monocrystalline. The amorphous rings in the diffraction pattern originate from the supporting carbon membrane and the ligands and chemical residues in the vicinity of the nanoparticle. The ligands are also visible in the HR TEM micrograph, as a darker amorphous layer between the ordered area of the bismuth nanoparticle and the brighter amorphous carbon membrane.

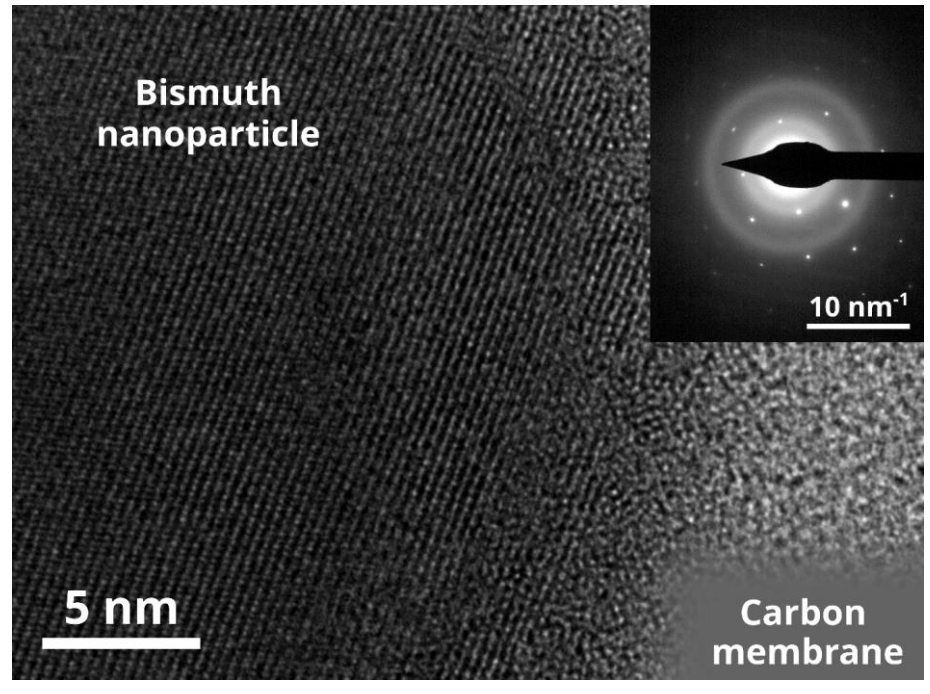


Figure 50: Diffraction pattern and HR TEM micrograph of a bismuth nanoparticle. From the ordering of the atomic planes and from the diffraction pattern is apparent the monocrystalline nature of synthesised nanoparticles. A darker-appearing amorphous ligand layer can be seen between the ordered bismuth and brighter amorphous carbon membrane.

3.4.2 Removal of ligands

In order to study the plasmonic properties of bismuth nanoparticles, the chemical residues and ligand layers should be removed. Otherwise, the build-up of conductive carbon contamination would make the EELS analysis of plasmon resonances in the bismuth nanoparticles impossible. Although the sources of contamination can usually be removed by plasma cleaning the sample, in this case, the amount of contamination was so large, that plasma cleaning proved to be insufficient and required to be combined with other cleaning processes. The following section is dedicated to my experimental findings on the removal of chemical residues and ligand chains from the surface of bismuth nanoparticles.

Every wet chemical synthesis of nanoparticle solutions culminates with the washing and removal of unwanted chemical residues. Most frequently, this is done by diluting the raw solution with a solvent which dissolves the chemical residues. The diluted solution is then centrifuged and the solvent with the dissolved chemical residues is poured out. However, during this process, part of the nanoparticles can be lost, depending on their size and shape [110]. Although this method usually removes the chemical residues floating in the solution, the removal of surfactants on the nanoparticle surface is extremely slow and requires numerous iterations of this process [111]. Furthermore, the success of centrifugation depends heavily on the viscosity of the solution. In viscous solutions, the smaller and lighter nanoparticles remain in the entire volume of the solution and are subsequently lost during the removal of the top liquid phase. Such is the case of TEG solutions.

In my attempts, I centrifuged the synthesised solutions for 60 minutes at 30,000 rpm. After the centrifugation, I removed half of the solution's volume and refilled it with methanol to the original volume. As expected, the centrifugation and washing of the solution resulted in a loss of smaller nanoparticles. Figure 51 shows STEM-HAADF micrographs of equally sized areas, one dripped with the centrifuged and replenished solution and the other dripped with the raw solution. The centrifuged solution contains far fewer nanoparticles and the missing small nanoparticles were lost during the centrifugation. Despite testing different combinations of centrifugation times and speeds, the process always resulted in a significant loss of nanoparticles. Furthermore, although the chemical residues were removed, the ligand shells on the nanoparticles remained. For these reasons, centrifugation is not an optimal technique for cleaning synthesised solutions.

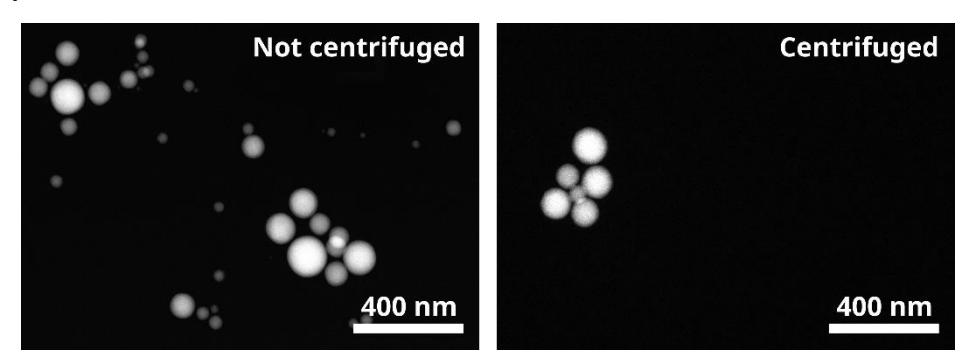


Figure 51: STEM-HAADF micrographs of equally large areas of sample dripped with the same volume of centrifuged-replenished solution and a raw solution from synthesised batch #4. The sample dripped with the centrifuged solution has lower concentrations of nanoparticles and the smallest nanoparticles are completely missing. This verifies that for more viscous solutions, even after centrifugation, small nanoparticles tend to float at the top and are consequently lost during washing of the centrifuged solution.

Another method, frequently used for cleaning the nanoparticle solutions, is the reduction by sodium borohydride (NaBH₄) [112]. Although the sodium borohydride should not be able to reduce amides and therefore does not react with PVP (which is used in various syntheses), other studies consider the NaBH₄ reduction a suitable technique for removal of a wide variety of surfactants, including the PVP [113], [114]. Because of the reported successful removal of PVP-based ligands, I decided to try this method on the synthesised nanoparticle solutions. I simply mixed 10 ml of the raw solution #3 with 0.1 g of NaBH₄. Immediately after adding the sodium borohydride, the solution started bubbling violently, releasing hydrogen gas. I stirred the solution for 15 minutes to allow the sodium borohydride fully dissolve and react. After that, I poured the solution into a vial and closed the lid. A minute later, the vial exploded. Based on the explosion, I believe the sodium borohydride had not yet fully reacted and continued releasing the hydrogen gas, which led to an overpressure in the vial. In my next attempt, I used the same steps and left the solution to react for 60 minutes. After that, I centrifuged and washed the solution to get rid of the chemical residues, mainly the reactive sodium and boron-based compounds. The subsequent analysis of the nanoparticles in STEM revealed, that the nanoparticles were bigger and with different texture. Furthermore, scanning of the electron beam damaged the nanoparticle, basically turning the analysis into an electron lithography. Since radiolysis is a prevalent beam damage type in metal-oxides, I knew the nanoparticle was not metallic. The STEM-EDX analysis presented in Figure 52 revealed it to be a sodium oxide nanoparticle. Although I have found a new way to synthesise sodium oxide nanospheres, the results of the purification approach based on sodium borohydride reduction failed to meet my expectations.

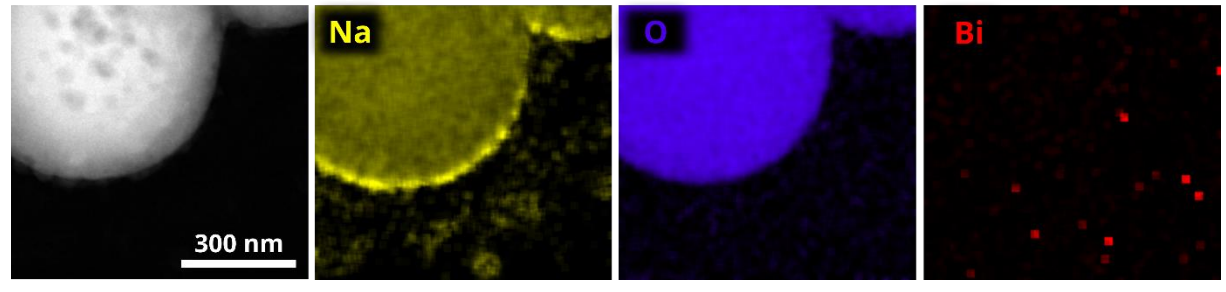


Figure 52: STEM-HAADF micrograph and elemental maps of sodium oxide nanoparticles synthesised during the failed attempt to clean Bi NPs by reduction of surfactants with sodium borohydride. The bismuth nanoparticles were completely missing. Furthermore, no trace of boron and nitrogen was present. The average nanoparticle diameter was in the order of hundreds of nanometres.

Another successful cleaning technique is based on the combined UV-ozone treatment. This cleaning technique is based on the illumination of the sample by light with wavelengths shorter than 250 nm [115]. The UV photons create ozone in the vicinity of the UV light source. The ozone, in combination with the UV photons then breaks down the organic compounds in the sample, creating CO_x , NO_x and other volatile compounds. This method has been used for the removal of PVP-based ligands from various metal nanoparticles [116]. The UV-ozone treatment is a less damaging alternative to regular plasma cleaning. However, compared to plasma cleaning which usually takes no more than a minute, the UV-ozone treatment requires hours to fully clean the sample.

Since the sources of UV light with sufficiently short wavelengths are only sold in the form of discharge tubes with included protective luminophore layer absorbing the most harmful wavelengths below 200 nm, I decided to obtain an alternative UV source from China. I bought LED diodes emitting at the wavelength of 250 nm and a discharge bulb, claimed to be emitting

at wavelengths even below 200 nm. After a short testing of the LEDs using a crafted planar circuit board, I found out that the emitted wavelengths were not sufficiently short to create ozone in the surrounding air. Furthermore, the LED diodes were overheating so much, that the soldered joints melted and the diodes fell off the circuit board. For this reason, I used the discharge bulb instead. The seller of the discharge bulb did not provide any specifications or emission characteristics of the bulb. For this reason, I asked Ing. Martin Konečný, Ph.D. to measure the emission spectrum of the discharge bulb. The obtained emission spectrum of the UV discharge bulb, along with a photo of the bulb are in Figure 53. Based on the strong odour noticeable when the light bulb was on, I can confidently claim that the bulb is capable of generating ozone gas. To clean the samples, I dripped the bismuth NP solution onto 40 nm thick SiO₂ TEM membranes, put the dripped membranes into a glass jar and placed the UV bulb above the samples. I left the samples in the glass jar for 12 hours to clean and after each hour opened the jar and, using a makeshift fan, exchanged the air inside. This was done to remove

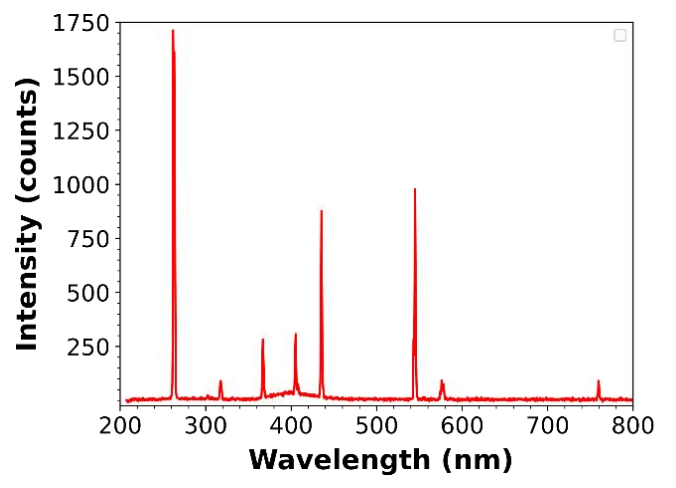




Figure 53: Spectral emission characteristic of the discharge bulb measured by Ing. Martin Konečný, Ph.D. During the measurement, the light bulb was connected to a voltage of 13 V and the current flowing through it was 0.75 A. Unfortunately, the spectrometer is unable to detect wavelengths below 200 nm. The spectroscope dispersion was set to 0.32 nm/px. On the right is a photo of the used discharge bulb.

the volatile gasses created during the treatment and to prevent their possible recombination and alternation of the sample. Before the TEM analysis of the nanoparticles, I plasma cleaned the samples for 10 seconds in an argon-oxygen plasma.

This cleaning approach proved to be more efficient than my previous attempts, as the build-up of contamination during the STEM analysis was negligible. After the treatment, the number of nanoparticles remaining on the membrane was significantly reduced. This is likely caused by the breakage of ligand shells, which usually hold the nanoparticles to the surface of the membrane. The disruption of the ligand shell and subsequent loss in adhesion leads to a significant loss of nanoparticles. Unfortunately, although the disruption of the ligand shell was noticeable, far thinner ligand layers remained. In conclusion, the ozone-treatment, combined with conventional plasma cleaning is a method yielding up to now the best results when it comes to reduction of the contaminants on the sample as well as the ligand shells on nanoparticles. However, a thorough examination of the cleaning approach and an optimisation of the workflow is needed, to minimise the loss of nanoparticles and to fully remove the remaining thinner ligand shells.

3.5 Plasmonic properties of bismuth nanospheres

The experimental setup and instrumentation were identical to those used to analyse polycrystalline bismuth antennas. However, the residual ligand shells on the surface of nanoparticles required a different approach when identifying and measuring the loss probability peaks of plasmon resonances. Usually, the EEL spectra are integrated over the area on the edge of the nanostructure, taking into account the spectra from both the antenna and its vicinity. I tried the same procedure for analysing nanoparticles which underwent the UV-ozone treatment. I chose a nanoparticle with a diameter of 106 nm for the initial EELS analysis. The EEL spectra from the nanoparticle's centre and edge are in Figure 54.

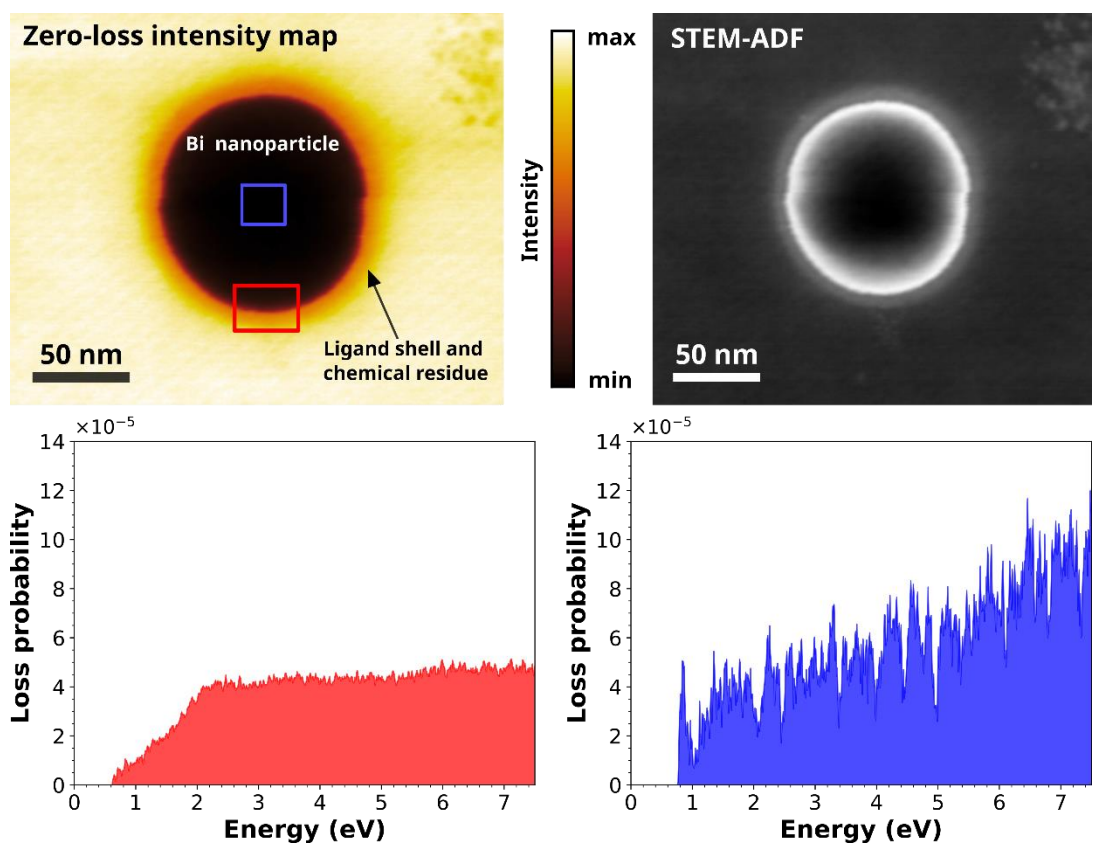


Figure 54: The intensity map of electrons with zero energy loss shows the 106 nm bismuth nanoparticle as the dark area. The orange-yellow ring around it corresponds to the ligand shell and chemical residues left after the UV-ozone treatment. The ligand shell is also visible in the STEM-ADF micrograph. The red and blue rectangles mark the area from which the spectra were integrated. Although no plasmon peak is visible in the spectrum from the nanoparticle's edge (in red), the onset of loss probability at energies from 0.8 eV to 3 eV is similar to onsets visible in low-loss spectra of direct bandgap semiconductors. However, the spectrum from the nanoparticle's centre (in blue) does not exhibit such loss probability onset. Therefore, the bismuth nanoparticle is not semiconducting.

The obtained spectrum does not contain any noticeable peak and the loss probability is relatively constant for energies above 1.8 eV. The onset of the loss probability starting at 0.6 eV appears to be similar to those found in low-loss EEL spectra of semiconductors with a direct band gap [117]. For this reason, I suspected that the loss-probability onset might be caused by the semiconducting behaviour of small bismuth nanoparticles, as has been frequently reported in the recent literature discussed in Section 3.1.3. If the nanoparticle was semiconducting, the characteristic loss probability onset would also be present in spectra collected from the centre

of the nanoparticle. Since the low loss spectrum from the centre of the nanoparticle did not contain any such loss probability onset, I rejected this theory.

Since I ruled out the possibility of the nanosphere being semiconducting, it was very likely, that the plasmon peaks are hidden in the signal corresponding to excitations of the residual ligand shell of the nanoparticle. In another attempt to find the plasmon resonance in the nanoparticle, I made intensity maps of the electrons' energy losses from 0.6 eV to 6 eV with a step of 0.1 eV. Six such maps, corresponding to various energy losses, among them to 2.2 eV and 5.5 eV, are shown in Figure 55.

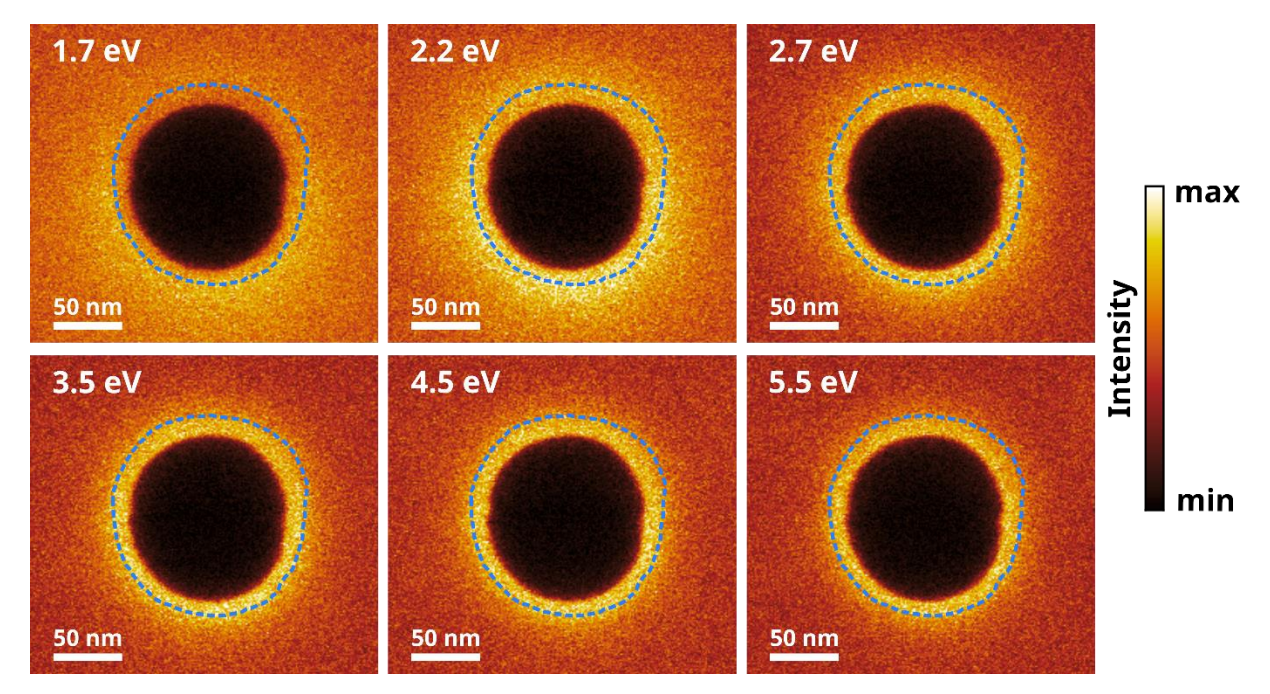


Figure 55: Intensity maps of electrons with various energy losses obtained from the EELS analysis of the 106 nm wide nanoparticle. The outer edge of the ligand shell is marked by the blue dashed line. In the map corresponding to the energy loss of 5.5 eV, the highest intensity is in the area of PVP-based ligand shell. This is caused by the absorption of the amide group at the energy of 5.5 eV. The area of highest intensity in the map at the energy of 2.2 eV reaches far beyond the area of the ligand shell. Therefore, the increased energy losses in that area are likely not related to excitations of ligand chains and instead correspond to the excitation of plasmon resonance in the nanoparticle.

The amide group of the PVP polymer chain absorbs energy of 5.5 eV [118]. Therefore, the map corresponding to this energy loss highlights the PVP-based ligand shell attached to the bismuth nanoparticle. Although the ligand shell absorbs nearly over the entire analysed energy interval, at 5.5 eV, the absorption is slightly higher. However, at energy losses below 2.8 eV, the intensity of electrons is not limited to the area of the ligand shell anymore and instead exceeds far beyond it. The largest area with the highest intensity was visible in the map corresponding to the energy loss of 2.2 eV. This is the plasmon resonance I have been searching for. As I have previously mentioned, EELS is sensitive to the out-of-plane electric field. In the case of plasmon resonances, such an electric field is present near the accumulated surface charge and as observed in the bismuth nanoparticles, the field reaches far beyond the edge of the nanostructure. Therefore, the observed increased intensity in the areas beyond the ligand shell corresponds to an electric field coupled to the localised surface plasmon in the nanosphere around the energy of 2.2 eV.

To obtain the exact energy of plasmon resonances in monocrystalline bismuth nanospheres, I used the zero-loss map to accurately identify the boundaries of the ligand shell. I integrated spectra from the region just outside this ligand shell, normalised them and subtracted the

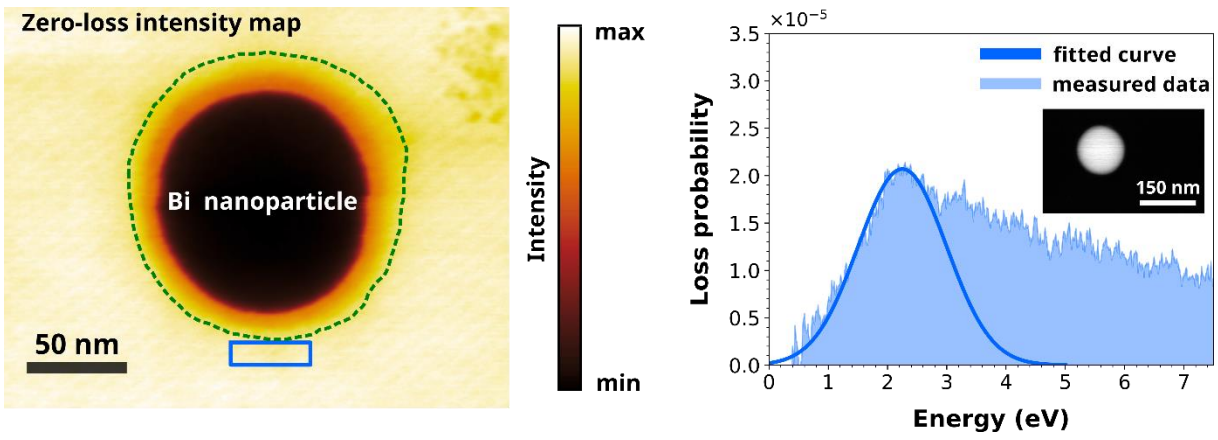


Figure 56: Loss probability measured on the area marked by a blue rectangle in the zero-loss intensity map is on the right. Measuring the EEL spectra from an area just outside the ligand shell (marked by the green dashed line) ensures that the signal is from the plasmon resonance and not from the ligand shell excitations. The loss probability maximum of the curve fitted to the plasmon peak has maximum at the energy of 2.25 eV and a FWHM of approximately 1.5 eV. In the inset is the STEM-HAADF micrograph of the analysed nanoparticle.

background signal from the membrane. The EEL spectrum obtained from the nanosphere using this procedure is shown in Figure 56. The normalised background-free spectrum contains a clear loss probability peak at the energy of 2.25 eV.

To further verify that this peak corresponds to a plasmon resonance, I measured the EEL spectra of nanoparticles with different diameters. If the peak energy shifts as the nanosphere diameter changes, I can assign these loss probability peaks to the localised surface plasmon resonances in bismuth nanospheres. Since the ligand shell thickness varies for different nanoparticle sizes, the spectra are integrated from areas in various distances from the bismuth nanoparticle and since the intensity of the electric field and with it the measured loss probabilities depend on the distance from the nanoparticle, the obtained plasmon loss probabilities of different nanoparticles cannot be compared. Since the loss probability maxima are tied to the peak width, I cannot interpret trends in the changes of peak width for different nanoparticle sizes as well.

I measured the loss probability spectra for nanoparticles with diameters of 100, 106, 114, 116 and 133 nm. I could not obtain EEL spectra of nanoparticles with other diameters because during the cleaning treatment, the majority of nanoparticles had been lost and only large clusters remained, along with occasional solitary nanoparticles, which had diameters around 110 nm. The obtained loss probability spectra are in Figure 57. Although the energy shift of plasmon resonances is not fully consistent for all nanoparticles, when we compare the plasmon energy in nanospheres with diameters of 100 nm and 133 nm, the plasmon energy shifted from 2.34 eV to 1.88 eV. The energy shift proves that the measured loss probability peaks correspond to plasmon resonances and not to excitations of chemical residues or ligand shells. Up to now, I have not specified the mode of the observed plasmon resonances. The symmetry of nanospheres makes a precise identification of the plasmon mode based on the loss probability maps difficult. Because of the symmetry, the loss probability maps of all plasmon modes look like a round halo around the nanosphere. Only once the symmetry is broken, would it be possible to safely identify the plasmon resonance. However, since the lowest mode in nanospheres is a dipole mode, the energy of the LSP resonance should be similar as in the

energy of the LD mode in a bismuth bar antenna with the length equivalent to the diameter of the nanoparticle. In Section the LD mode in the 80 nm bismuth bar antenna with a length of 103 nm has the energy of 2.05 eV. Since this energy is comparable to the plasmon energy of 2.25 eV corresponding to the LSP resonance found in a nanoparticle with a diameter of 106 nm, it is safe to consider the lowest plasmon peak in bismuth nanoparticles a dipole mode.

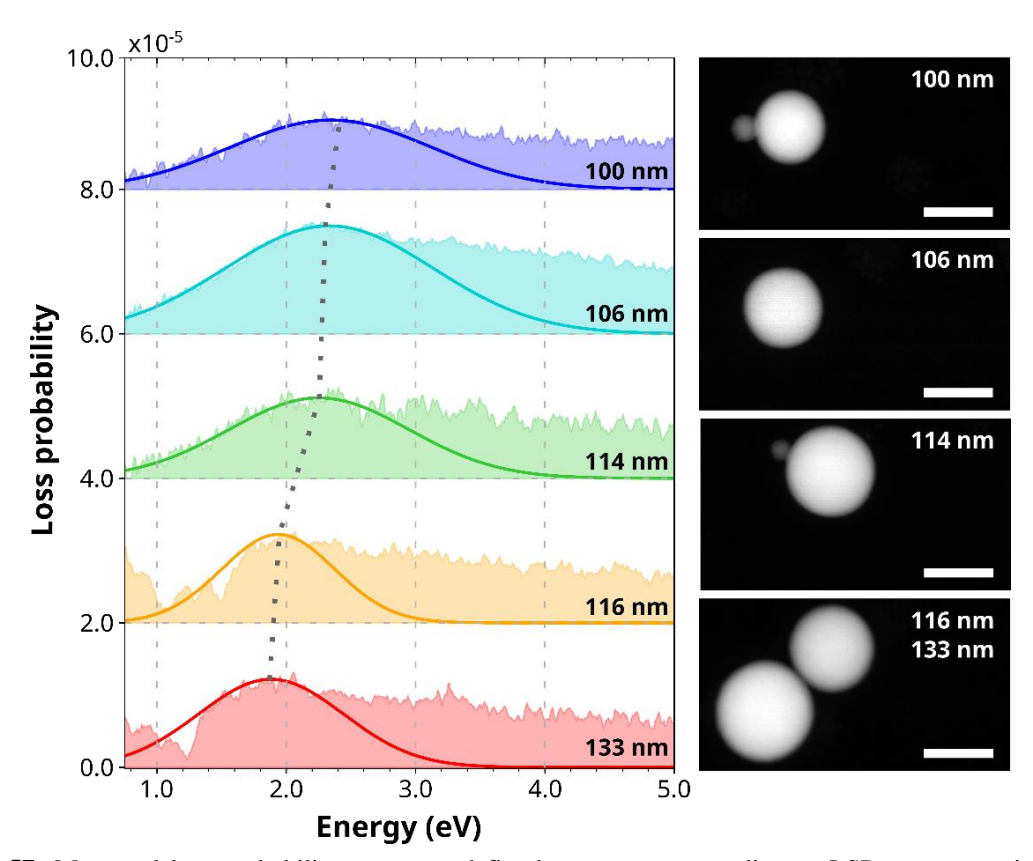


Figure 57: Measured loss probability spectra and fitted curves corresponding to LSP resonances in bismuth nanospheres of various diameters. On the right are the STEM-HAADF micrographs of individual studied nanospheres. The scalebars are 100 nm long. The energy shifts of plasmon peaks are not much noticeable, because the differences in nanosphere's diameters are not sufficiently large. Nevertheless, the energy shift of nanoparticles with diameter difference above 10 nm is already noticeable. The loss spectra of nanospheres with diameters of 133 and 116 nm suffer from artefacts at energies below 1 eV. Since the spectra of both nanospheres come from one measurement, it is likely caused by the instrumentation or insufficient background subtraction.

As I have found an optimal approach for collecting EEL spectra containing the signal from plasmon resonances with only a negligible contribution from excitations of ligand shells, I decided to apply this approach to nanoparticles cleaned only by plasma cleaning. The measured EEL spectrum from such untreated nanoparticle with a diameter of 67 nm is in Figure 58. The untreated nanoparticles are usually covered by a significantly thicker ligand shell. This requires integrating spectra further away from the nanoparticle. Therefore, the EEL spectra measured on these uncleaned nanoparticles suffer from a lower signal-to-noise ratio. However, the plasmon peaks are still easily recognisable. This means that my approach allows for the analysis of plasmon resonances without the need to remove or clean the ligand shells off the nanoparticles before the EELS analysis.

In conclusion, monocrystalline bismuth nanospheres support plasmon resonances. Although it is possible to study the plasmon resonances by EELS even on nanoparticles with thick ligand shells, cleaning the nanoparticles by UV-ozone treatment leads to a better signal-to-noise ratio

of measured EEL spectra and with it, a more reliable interpretation of the plasmon resonance loss probability peaks.

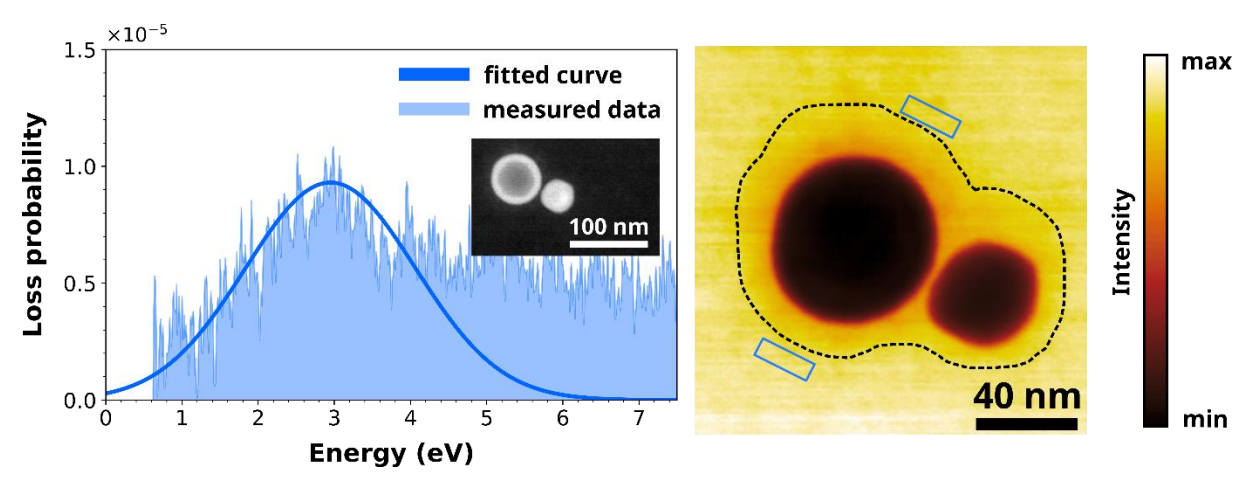


Figure 58: Measured loss probability spectrum and fitted curve corresponding to the plasmon resonance at the energy of 2.95 eV in an untreated nanoparticle with a diameter of 65 nm. The inset shows the STEM-ADF micrograph of the nanoparticle. The blue rectangles in the zero-loss intensity map on the right mark the areas from which was extracted the obtained spectrum. The dark-yellow hue highlighted by the black dashed line around the two nanoparticles marks the ligand shell, much thicker than ligand shells found in nanoparticles treated by the UV-ozone treatment.

4 Conclusion

Within this master thesis I have investigated the possibilities of non-noble metals in the field of plasmonics. First, I have numerically simulated the plasmonic properties of a bowtie antenna made from bismuth, lead, aluminium, and indium. Based on the results I chose bismuth as the material of focus for its expected highest intensity of plasmon resonances.

To study the plasmonic properties of polycrystalline bismuth thin films, I deposited 30 nm thick bismuth layers by magnetron sputtering. The subsequent analysis of the layers revealed their high roughness and high concentration of pores in their volume. I carried out tests regarding the susceptibility of deposited bismuth layers to oxidation and found the deposited bismuth films resistant to oxidation even months after the deposition unless exposed to a plasma cleaning or annealing. Using the focused ion lithography of the deposited layer, I fabricated 40 nm wide bar-shaped antennas with lengths from 80 to 350 nm. Furthermore, I fabricated 80 nm bar antennas with antenna lengths from 80 to 550 nm. Finally, I also fabricated bowtie antennas with a 20 nm gap between its wings and the wing widths from 200 to 700 nm. The focused ion beam lithography of bismuth films proved to be an ideal method for antenna fabrication, offering high fabrication yields.

The plasmon resonances in the fabricated antennas were studied by electron energy loss spectroscopy. The plasmon peaks observed in the electron energy loss spectra are rather wide and exhibit high Q-factors. A broad range of usable wavelengths is similar to gold, and, therefore makes bismuth a viable and cost-effective substitute for gold. A performed in-situ experiment proved, that the already good plasmonic properties of bismuth antennas can be further improved by cooling down the sample to low temperatures, increasing the intensity of plasmon resonance and lowering the damping of plasmon resonances in the antenna.

To analyse the plasmonic properties of monocrystalline bismuth, I synthesised bismuth nanospheres by a pyrolysis of bismuth acetate. Such synthesis proved to be a foolproof method for the fabrication of nanospheres with diameters from 10 to 140 nm. I tested various cleaning methods for removing the surfactant layers off the surface of bismuth nanoparticles. Among these, cleaning by exposing the nanoparticles to UV illumination in an ozone atmosphere proved to be the most functional approach. However, although the UV-ozone treatment disrupts the ligand shells at the surface of nanoparticles, it also reduces the adhesion of the thin membrane, resulting in a significant loss of nanoparticles. I verified the presence of plasmon resonances in the synthesised bismuth nanoparticles and developed a method for collecting electron energy loss spectra from nanoparticles, without the need to remove the present thick layers of contaminants. The used method allows for collecting signals corresponding to plasmon resonances in the nanoparticle, with a minor or almost negligible contribution from excitations of ligand shell and contaminants surrounding the nanosphere.

My work verified the expected extraordinary plasmonic properties of bismuth and thus can serve as a starting point for follow-up research on bismuth as a plasmonic material. Within my PhD study, the plasmonic properties of bismuth antennas can be further improved by an optimisation of the deposition process, primarily to reduce the roughness of deposited layers. Similarly, a study of the plasmonic properties of bismuth antennas at temperatures below 100 K might bring interesting results for applications combining cryogenics and plasmonics. Additionally, the transition from metallic to a semiconducting state of bismuth thin films depending on the layer thickness might be of interest as well. I would also like to continue the study of bismuth nanospheres and include also bismuth nanoparticles with different geometries,

such as nanotriangles, nanocubes and nanowires. Such future studies could profit from improvements in the cleaning processes needed for removal of ligands. An optimisation of the used cleaning treatment is also essential for further studies of other non-noble plasmonic materials such as indium, tin, and lead.

References

- [1] MAIER, S. A., et al.: Plasmonics—A Route to Nanoscale Optical Devices. Advanced Materials. 2001, 13(19), 1501–1505. ISSN 1521-4095. https://doi.org/10.1002/adma.200390134
- [2] SOLER, M., LECHUGA, L. M.: Principles, technologies, and applications of plasmonic biosensors. *J. Appl. Phys.* 2021, 129(11), 111102. ISSN 1089-7550. https://doi.org/10.1063/5.0042811
- [3] ZHANG, J. Z., NOGUEZ, C.: Plasmonic Optical Properties and Applications of Metal Nanostructures. *Plasmonics*. 2008, 3, 127–150. ISSN 1557-1955. https://doi.org/10.1007/s11468-008-9066-y
- [4] HORÁK, M.: *Electron microscopy and spectroscopy in plasmonics*. Brno, 2019. Doctoral thesis. Brno University of Technology, CEITEC BUT. Supervisor of the doctoral thesis prof. RNDr. Tomáš Šikola, CSc. Available online: https://www.vutbr.cz/en/students/final-thesis/detail/122351.
- [5] HORÁK, M., et al.: Comparative study of plasmonic antennas fabricated by electron beam and focused ion beam lithography. *Scientific Reports*. 2018, 8, 9640. ISSN 2045-2322. https://doi.org/10.1038/s41598-018-28037-1
- [6] KEJÍK, L., et al.: Structural and optical properties of monocrystalline and polycrystalline gold plasmonic nanorods. *Optics Express.* 2020, vol. 28, p. 34960. ISSN 1094-4087. https://doi.org/10.1364/OE.409428
- [7] HORÁK, M., et al.: Limit of Babinet's principle for solid and hollow plasmonic antennas. *Scientific Reports*. 2019, 9(1), 4004. ISSN 2045-2322. https://doi.org/10.1038/s41598-019-40500-1
- [8] HRTOŇ, M., et al.: Plasmonic Antennas with Electric, Magnetic, and Electromagnetic Hot Spots Based on Babinet's Principle. *Physical Review Applied*. 2020, 13(5), 1–14. ISSN 2331-7019. https://doi.org/10.1103/PhysRevApplied.13.054045
- [9] BABOCKÝ, J., et al.: Quantitative 3D Phase Imaging of Plasmonic Metasurfaces. *ACS Photonics*. 2017, 4(6), 1389–1397. ISSN 2330-4022. https://doi.org/10.1021/acsphotonics.7b00022
- [10] ROVENSKÁ, K., et al.: Structural color filters with compensated angle-dependent shifts. *Opt. Express*. 2023, 31(26), 43048–43056. ISSN 1094-4087. https://doi.org/10.1364/OE.506069
- [11] HORÁK, M., et al.: Plasmonic Properties of Individual Gallium Nanoparticles. *The Journal of Physical Chemistry Letters.* 14(8), 2012–2019. ISSN 1948-7185. https://doi.org/10.1021/acs.jpclett.3c00094
- [12] SONG, M., et al.: Colors with plasmonic nanostructures: A full-spectrum review. *Applied Physics Review*. 2019, 6(4), 041308. ISSN 1931-9401. https://doi.org/10.1063/1.5110051
- [13] JIANG, N., et al.: Active Plasmonics: Principles, Structures and Applications. Chemical Reviews. 2018, 117(6), 3054–3099. ISSN 0009-2665. https://doi.org/10.1021/acs.chemrev.7b00252

- [14] MAIER, S. A.: *Plasmonics: Fundamentals and Applications*. Springer Science+Business Media LLC New York, 2007. ISBN 978-0387-33150-8.
- [15] DVOŘÁK, P. *Nanofotonika*. Brno, 2018. Brno University of Technology, Faculty of Mechanical Engineering. Doctoral thesis. 134 s. Supervisor of the doctoral theis prof. RNDr. Tomáš Šikola, CSc. Available online: https://www.vut.cz/studenti/zav-prace/detail/113752
- [16] MAYER, K. M., HAFNER, J.H.: Localised Surface Plasmon Resonance Sensors. Chemical Reviews. 2011, 111(6), 3828–3857. ISSN 0009-2665. https://doi.org/10.1021/cr100313v
- [17] STOCKMAN, M.: M. Nanoplasmonics: past, present, and glimpse into future. *Opt. Express.* 2011, 19, 22029–22106. ISSN 1094-4087. https://doi.org/10.1364/OE.19.022029
- [18] LIGMAJER, F., et al.: (2019). Silver Amalgam Nanoparticles and Microparticles: A Novel Plasmonic Platform for Spectroelectrochemistry. *The Journal of Physical Chemistry C*. 2019, 123(27), 16957–16964. ISSN 1932-7455. https://doi.org/10.1021/acs.jpcc.9b04124
- [19] FARRADAY, M.: Experimental Relations of Gold (and Other Metals) to Light. Philosophical Transactions of the Royal Society of London. 1857, 147, 145–181. ISSN 2053-9223. https://doi.org/10.1098/rstl.1857.0011
- [20] BABOCKÝ, J., et al.: Quantitative 3D Phase Imaging of Plasmonic Metasurfaces. *ACS Photonics*. 2017, 4(6), 1389–1397. ISSN 2330-4022. https://doi.org/10.1021/acsphotonics.7b00022
- [21] BOUCHAL, P., et al.: High-Resolution Quantitative Phase Imaging of Plasmonic Metasurfaces with Sensitivity down to a Single Nanoantenna. *Nano Letters*. 2019, 19(2), 1242–1250. ISSN 1530-6984. https://doi.org/10.1021/acs.nanolett.8b04776
- [22] KIM, M. K. Principles and techniques of digital holographic microscopy. *SPIE Reviews*. 2010, 1(1), 1–51. https://doi.org/10.1117/6.0000006
- [23] CAO, W., et al.: Localized surface plasmon resonance of single silver nanoparticles studied by dark-field optical microscopy and spectroscopy. *J. Appl. Phys.* 2011, 109(3), 034310. ISSN 0021-8979. https://doi.org/10.1063/1.3544349
- [24] DVOŘÁK, P., et al.: Imaging of near-field interference patterns by aperture-type SNOM influence of illumination wavelength and polarization state. *Opt. Express.* 2017, 25, 16560-16573. ISSN 1094-4087. https://doi.org/10.1364/OE.25.016560
- [25] QIAN, Q., et al.: Plasmonic focusing of infrared SNOM tip patterned with asymmetric structures. *Opt. Express.* 2015, 23(10), 12923–12934. ISSN 1094-4087. https://doi.org/10.1364/OE.23.012923
- [26] DVOŘÁK, P., et al.: Control and Near-Field Detection of Surface Plasmon Interference Patterns. *Nano Letters*. 2013, 13(6), 2558–2563. ISSN 1530-6984. https://doi.org/10.1021/nl400644r
- [27] STÖGER-POLLACH, M., et al.: Fundamentals of cathodoluminescence in a STEM: The impact of sample geometry and electron beam energy on light

- emission of semiconductors. *Ultramicroscopy*. 2019, 200, 111–124. ISSN 0304-3991. https://doi.org/10.1016/j.ultramic.2019.03.001
- [28] CHAO-YU, L., ZHONG-QUN, T.: Sixty years of electrochemical optical spectroscopy: a retrospective. *Chem. Soc. Rev.* 2024. ISSN 0306-0012. http://dx.doi.org/10.1039/D3CS00734K
- [29] VOBORNIK, D., VOBORNIK, S.: Scanning Near-Field Optical Microscopy. *Biomol Biomed.* 2008, 8(1), 63-71. ISSN 1840-4812. https://doi.org/10.17305/bjbms.2008.3000
- [30] WILLIAMS, D. B., CARTER, C. B.: Transmission Electron Microscopy. Springer New York, NY, 2009. ISBN 978-0-387-76500-6. https://doi.org/10.1007/978-0-387-76501-3
- [31] DE BACKER, A., et al.: A decade of atom-counting in STEM: From the first results toward reliable 3D atomic models from a single projection. *Ultramicroscopy*. 2023, 247, 113702. ISSN 0304-3991. https://doi.org/10.1016/j.ultramic.2023.113702
- [32] GRIEB, T., et al.: Angle-resolved STEM using an iris aperture: Scattering contributions and sources of error for the quantitative analysis in Si. *Ultramicroscopy*. 2021, 221, 113175. ISSN 0304-3991. https://doi.org/10.1016/j.ultramic.2020.113175
- [33] EELS info. *Collection Angle Considerations* [online]. [cit. 2024-04-22]. Available from: https://eels.info/how/getting-started/collection-angle-considerations
- [34] EGERTON, R.F.: *Physical Principles of Electron Microscopy*. Springer, Boston, 2005. ISBN: 978-0-387-25800-3
- [35] CHEN, Z., et al.: Energy dispersive X-ray analysis on an absolute scale in scanning transmission electron microscopy. *Ultramicroscopy*. 2015,157, 21-26. ISSN 0304-3991. https://doi.org/10.1016/j.ultramic.2015.05.010
- [36] EGERTON, R. F.: *Electron Energy-Loss Spectroscopy in the Electron Microscope*. Springer, New York, 2011. ISBN 978-1-4419-9583-4. https://doi.org/10.1007/978-1-4419-9583-4
- [37] BRYDSON, R.: *Electron Energy Loss Spectroscopy*. Garland Science, London, 2001. ISBN 9781003076858. https://doi.org/10.1201/9781003076858
- [38] REIMER, L.: *Energy-Filtering Transmission Electron Microscopy*. Springer Berlin, Heidelberg, 1995. ISBN 978-3-662-14055-0. https://doi.org/10.1007/978-3-540-48995-5
- [39] FELDMAN, M.: *Nanolithography: The art of fabricating nanoelectronic and nanophotonic devices and systems.* Woodhead Publishing, Oxford, 2014. ISBN 978-0-85709-500-8.
- [40] JAMKHANDE, P. G., et al.: Metal nanoparticles synthesis: An overview on methods of preparation, advantages and disadvantages, and applications. Journal of Drug Delivery Science and Technology. 2019, 53, 101174. ISSN 1773-2247. https://doi.org/10.1016/j.jddst.2019.101174

- [41] DE OLIVEIRA, P. F. M., et al.: Challenges and opportunities in the bottom-up mechanochemical synthesis of noble metal nanoparticles. *J. Mater. Chem. A.* 2020, 8(32), 16114–16141. ISSN 0169-409X. https://doi.org/10.1039/D0TA05183G
- [42] ABID, N., et al.: Synthesis of nanomaterials using various top-down and bottom-up approaches, influencing factors, advantages, and disadvantages: A review. *Advances in Colloid and Interface Science*. 2020, 300, 102597. ISSN 0001-8686. https://doi.org/10.1016/j.cis.2021.102597
- [43] EL-ESKANDARANY, M. S., et al.: Mechanical Milling: A Superior Nanotechnological Tool for Fabrication of Nanocrystalline and Nanocomposite Materials. *Nanomaterials*. 2021, 11, 2484. ISSN 2079-4991. https://doi.org/10.3390/nano11102484
- [44] MYUNGJOON, K., et al.: Synthesis of Nanoparticles by Laser Ablation: A Review. *KONA Powder Part. J.* 2017, 34, 80-90. ISSN 2187-5537. https://doi.org/10.14356/kona.2017009
- [45] POVARNITSYN, M. E., et al.: Mechanisms of nanoparticle formation by ultrashort laser ablation of metals in liquid environment. *Phys. Chem. Chem. Phys.* 2013, 15, 3108-3114. ISSN 1463-9084. https://doi.org/10.1039/C2CP42650A
- [46] MANZOOR, U., et al.: Effect of Synthesis Temperature, Nucleation Time, and Postsynthesis Heat Treatment of ZnO Nanoparticles and Its Sensing Properties. *Journal of Nanomaterials*. 2015, 2015, 1687. ISSN 1687-4129. https://doi.org/10.1155/2015/189058
- [47] RUBANOV, S., MUNROE, P. FIB-induced damage in silicon. *Journal of Microscopy*. 2004, 214, 213–221. ISSN 1365-2818. https://doi.org/10.1111/j.0022-2720.2004.01327.x
- [48] JAMALUDIN, F., et al.: Controlling parameters of focused ion beam (FIB) on high aspect ratio micro holes milling. *Microsystem Technologies*. 2013, 19(12), 1873–1888. ISSN 1432-1858. https://doi.org/10.1007/s00542-013-1912-y
- [49] TU Wien. *A Simple Sputter Yield Calculator* [online]. [cit. 2024-02-17]. Dostupné také z: https://www.tuwien.at/en/phy/iap/tools/sputter-yield-calculator
- [50] KIENER, D., et al.: FIB Damage of Cu and Possible Consequences for Miniaturized Mechanical Tests. Materials Science and Engineering A. 2007, 459(1-2), 262–272. ISSN 0921-5093. https://doi.org/10.1016/j.msea.2007.01.046
- [51] PREISS, E. I., et al.: Applicability of focused Ion beam (FIB) milling with gallium, neon, and xenon to the fracture toughness characterization of gold thin films. Journal of Materials Research. 2021, 36(12), 2505–2514. ISSN 2044-5326. https://doi.org/10.1557/s43578-020-00045-w
- [52] NAM, HS., SROLOVITZ, D.J.: Effect of material properties on liquid metal embrittlement in the Al-Ga system. Acta Materialia. 2009, 57, 1546-1553. ISSN 1359-6454. http://dx.doi.org/10.1016/j.actamat.2008.11.041
- [53] FOLTÝN, M.: *Příprava plazmonických antén pro analytickou transmisní elektronovou mikroskopii pomocí iontové litografie*. Brno, 2022. Bachelor thesis. Brno University of Technology, Faculty of Mechanical Engineering, Institute of

- Physical Engineering. Supervisor of the bachelor thesis Ing. Michal Horák, Ph.D. Available online: https://www.vutbr.cz/studenti/zav-prace/detail/139474.
- [54] SAFO, I. A., et al.: The role of polyvinylpyrrolidone (PVP) as a capping and structure-directing agent in the formation of Pt nanocubes.

 Nanoscale Advances. 2019, 1, 3095-3106. ISSN 2516-0230. https://doi.org/10.1039/C9NA00186G
- [55] BAKSHI, M. S.: How Surfactants Control Crystal Growth of Nanomaterials. *Cryst. Growth Des.* 2016, 16(2), 1104-1133. ISSN 1528-7505. https://doi.org/10.1021/acs.cgd.5b01465
- [56] GHARIBSHAHI, L., et al.: Influence of Poly(vinylpyrrolidone) concentration on properties of silver nanoparticles manufactured by modified thermal treatment method. *PLoS One*. 2017,12(10), 186094. ISSN 1544-9173. https://doi.org/10.1371%2Fjournal.pone.0186094
- [57] JIANG, XC., et al.: Role of Temperature in the Growth of Silver Nanoparticles Through a Synergetic Reduction Approach. *Nanoscale Res Lett.* 2011, 6(1), 32. ISSN 1556-276X. https://doi.org/10.1007%2Fs11671-010-9780-1
- [58] SOMODI, F., et al.: Effects of the Synthesis Parameters on the Size and Composition of Pt–Sn Nanoparticles Prepared by the Polyalcohol Reduction Method. *J. Phys. Chem. C.* 2011, 115(39), 19084-19090. ISSN 1932-7455. https://doi.org/10.1021/jp206482y
- [59] MOUNTRICHAS, G.: Effect of Temperature on the Direct Synthesis of Gold Nanoparticles Mediated by Poly(dimethylaminoethyl methacrylate)
 Homopolymer. *J. Phys. Chem. C.* 2014, 118(39), 22754-22759. ISSN 1932-7455. https://doi.org/10.1021/jp505725v
- [60] BALVANDY, S. K., et al.: Stirring time effect of silver nanoparticles prepared in glutathione mediated by green method. *Chemistry Central Journal*. 2014, 8(11). ISSN 1752-153X. https://doi.org/10.1186/1752-153X-8-11
- [61] MASCARETTI, L., et al.: Plasmon-Enhanced Photoelectrochemical Water Splitting for Efficient Renewable Energy Storage. *Advanced Materials*. 2019, 31(31). 1805513. ISSN 1521-4095. http://dx.doi.org/10.1002/adma.201805513
- [62] SANZ, J. M., et al.: UV Plasmonic Behavior of Various Metal Nanoparticles in the Near- and Far-Field Regimes: Geometry and Substrate Effects. *The Journal of Physical Chemistry C.* 2013, 117 (38), 19606–19615. ISSN 1932-7455. https://doi.org/10.1021/jp405773p
- [63] McMAHON, J. M., et al.: Plasmonics in the ultraviolet with the poor metals Al, Ga, In, Sn, Tl, Pb and Bi. *Phys. Chem. Chem. Phys.* 2015, 17(29), 19670–19671. ISSN 1463-9084. https://doi.org/10.1039/C3CP43856B
- [64] RINGE, E.: Shapes, Plasmonic Properties, and Reactivity of Magnesium Nanoparticles. *The Journal of Physical Chemistry C*. 2020, 124(29), 15665–15679. ISSN 1932-7455. https://doi.org/10.1021/acs.jpcc.0c03871
- [65] CASTILLA, M., et al.: Colloidal Synthesis of Crystalline Aluminum Nanoparticles for UV Plasmonics. *ACS Photonics*. 2022 ,9(3), 880–887. ISSN 2330-4022. https://doi.org/10.1021/acsphotonics.1c01615

- [66] HOHENESTER, U., TRÜGLER, A.: MNPBEM A Matlab toolbox for the simulation of plasmonic nanoparticles. *Computer Physics Communications*. 2012, 183(2), 370–381. ISSN 0010-4655. https://doi.org/10.1016/j.cpc.2011.09.009
- [67] CEITEC Nano. *High-resolution (scanning) Transmission Electron Microscope FEI Titan Themis 60-300 cubed (TITAN)* [online]. [cit. 2024-03-16]. Available from: https://nano.ceitec.cz/high-resolution-scanning-transmission-electron-microscope-fei-titan-themis-60-300-cubed-titan/
- [68] GOLOVASHKIN, A. I., MOTULEVICH, G. P.: Optical and electrical properties of tin. *Journal of Experimental Theoretical Physics*. 1964, 46(19), 460–470. ISSN 1063-7761. http://jetp.ras.ru/cgi-bin/dn/e 019 02 0310.pdf
- [69] WERNER, W., et al.: Optical Constants and Inelastic Electron-Scattering Data for 17 Elemental Metals. J. Phys. Chem. Ref. Data. 2009, 38(4), 1013–1092. ISSN 0047-2689. http://dx.doi.org/10.1063/1.3243762
- [70] MATHEWSON, A. G., MYERS, H. P.: Absolute Values of the Optical Constants of Some Pure Metals. Phys. Scr. 1971, 4(6), 291–292. ISSN 1402-4896. https://doi.org/10.1088/0031-8949/4/6/009
- [71] ROSENBLATT, G., et al.: Nonmodal Plasmonics: Controlling the Forced Optical Response of Nanostructures. *Phys. Rev. X.* 2020, 10(1), 11071–11092. ISSN 2160-3308. https://doi.org/10.1103/PhysRevX.10.011071
- [72] McPEAK, K. M., et al.: Plasmonic films can easily be better: Rules and recipes. *ACS Photonics*. 2015, 2(3), 326–333. ISSN 2330-4022. https://doi.org/10.1021/ph5004237
- [73] COLLETTE, R., et al.: Near field excited state imaging via stimulated electron energy gain spectroscopy of localized surface plasmon resonances in plasmonic nanorod antennas. *Sci Rep.* 2020,10, 12537. https://doi.org/10.1038/s41598-020-69066-z
- [74] KŘÁPEK, V., et al.: Independent engineering of individual plasmon modes in plasmonic dimers with conductive and capacitive coupling. *Nanophotonics*. 2020, 9(3), 623-632. ISSN 2192-8614. https://doi.org/10.1515/nanoph-2019-0326
- [75] KOH, A.L., et al.: Electron Energy-Loss Spectroscopy (EELS) of Surface Plasmons in Single Silver Nanoparticles and Dimers: Influence of Beam Damage and Mapping of Dark Modes. *ACS Nano*. 2009, 3(10), 3015–3022. ISSN 1936-086X. https://doi.org/10.1021/nn900922z
- [76] DE MARCILLAC, P., et al.: Experimental detection of α-particles from the radioactive decay of natural bismuth. *Nature*. 2003, 422, 876–878. ISSN 1476-4687. https://doi.org/10.1038/nature01541
- [77] LIAO, A. D., et al.: Induced electronic anisotropy in bismuth thin films. *Applied Physics Letters*. 2014, 105(6), 063114. ISSN 0003-6951. https://doi.org/10.1063/1.4893140
- [78] CHUDZINSKI, P., GIAMARCHI, T.: Collective excitations and low-temperature transport properties of bismuth. *Phys. Rev. B.* 2011, 84(12), 125105. ISSN 2469-9969. https://doi.org/10.1103/PhysRevB.84.125105

- [79] LIU, Y., ALLEN, R. E. Electronic structure of the semimetals Bi and Sb. *Phys. Rev. B.* 1995, 52(3), 1566. ISSN 2469-9969. https://doi.org/10.1103/PhysRevB.52.1566
- [80] BIAN, G. et al.: Survey of electronic structure of Bi and Sb thin films by first-principles calculations and photoemission measurements. *Journal of Physics and Chemistry of Solids*. 2019, 128, 109–117. ISSN 0022-3697. https://doi.org/10.1016/j.jpcs.2017.07.027
- [81] HOFFMAN, PH.: The surfaces of bismuth: Structural and electronic properties. *Progress in Surface Science*. 2006, 81(5), 191–245. ISSN 0079-6818. https://doi.org/10.1016/j.progsurf.2006.03.001
- [82] WANG, N., et al.: Investigation of growth characteristics and semimetal—semiconductor transition of polycrystalline bismuth thin films. International Union of Crystallography Journal. 2020, 7(1), 49–57. ISSN 2052-2525. https://doi.org/10.1107/S2052252519015458
- [83] CAMPS, E., et al.: A Detailed Study of the Synthesis of Bismuth Thin Films by PVD-Methods and their Structural Characterization. *MRS Online Proceedings Library*. 2012, 1477, 21–27. https://doi.org/10.1557/opl.2012.1703
- [84] VANDAMME, L. K. J., KEDZIA, J.: Concentration, mobility, and 1/f noise of electrons and holes in thin bismuth films. *Thin Solid Films*. 1980, 65(3), 283–292. ISSN 0040-6090. https://doi.org/10.1016/0040-6090(80)90238-2
- [85] XIUFANG, Q., et al.: Influence of substrate temperature on the morphology and structure of bismuth thin films deposited by magnetron sputtering. *Vacuum*. 2019, 166, 316–322. ISSN 0042-207X. https://doi.org/10.1016/j.vacuum.2019.05.026
- [86] DONG-HO, K., et al.: Structure and electrical transport properties of bismuth thin films prepared by RF magnetron sputtering. *Applied Surface Science*. 2006, 252(10), 3525–3531. ISSN 0169-4332. https://doi.org/10.1016/j.apsusc.2005.05.046
- [87] CHANG, J., et al.: Microstructure and magnetoresistance of sputtered bismuth thin films upon annealing. *Journal of Applied Physics*. 2005, 98(2), 023906. ISSN 1089-7550. https://doi.org/10.1063/1.1989433
- [88] OKSANEN, Mika. *Annealing Study of Bismuth Thin Films*. Jyväskylä, 2010. Master's thesis. University of Jyväskylä, Department of Physics, Nanoscience Center. Supervisor of the master's thesis prof. Ilari Maasilta. Available online: https://jyx.jyu.fi/bitstream/handle/123456789/24486/1/URN%3ANBN%3Afi%3Ajyu-201006232140.pdf
- [89] KOCHOWSKI, S., OPILSKI, A.: Concentration and mobility of charge carriers in thin polycrystalline films of bismuth. *Thin Solid Films*. 1978, 48, 345–351. ISSN 0040-6090. https://doi.org/10.1016/0040-6090%2878%2990014-7
- [90] KUMAR, A., KATYAL, O. P.: Electrical resistivity of thin bismuth films. *Journal of Materials Science: Materials in Electronics*. 1990, 1, 51–56. ISSN 1573-482X. https://doi.org/10.1007/BF00716018

- [91] RAMADAN, A. A., et al.: Size-dependent structural characteristics of thin bismuth films. Thin Solid Films. 1992, 209(1), 32–37. ISSN 0040-6090. https://doi.org/10.1016/0040-6090(92)90006-W
- [92] XIANGCHAO, M., et al.: Electronic and optical properties of strained noble metals: Implications for applications based on LSPR. Nano Energy. 2018, 53, 932–939. ISSN 2211-2855. https://doi.org/10.1016/j.nanoen.2018.09.042
- [93] SHAHBAZI-GAHROUEI, D., et al.: A review of bismuth-based nanoparticles and their applications in radiosensitising and dose enhancement for cancer radiation therapy. *IET Nanobiotechnology*. 2023, 17(4), 302–311. ISSN 1751-875X. https://doi.org/10.1049%2Fnbt2.12134
- [94] OSHIMA, Y., et al.: Structural anomaly of fine bismuth particles observed by ultra-high-vacuum TEM. *Z Phys D Atoms, Molecules and Clusters*. 1997, 40, 534–538. ISSN 0178-7683. https://doi.org/10.1007/s004600050271
- [95] CAROTENUTO, G., et al.: Synthesis and thermoelectric characterisation of bismuth nanoparticles. *Journal of Nanoparticle Research*. 2009, 11(7), 1729–1738. ISSN 1998-0000. http://dx.doi.org/10.1007/s11051-008-9541-6
- [96] WANG. J.: Giant positive magnetoresistance in non-magnetic bismuth nanoparticles. *Materials Research Bulletin*. 2003, 38. ISSN 0025-5408. http://dx.doi.org/10.1016/S0378-7788(03)00077-X
- [97] MARCHAK, D., et al.: Large anisotropic conductance and band gap fluctuations in nearly round-shape bismuth nanoparticles. *Nano Lett.* 2012, 12(2), 1087–1091. ISSN 1530-6992. https://doi.org/10.1021/nl204460y
- [98] STOKES, K. L., et al.: Synthesis and properties of bismuth nanocrystals. *Eighteenth International Conference on Thermoelectrics Proceedings, ICT'99* (*Cat. No.99TH8407*). 1999, 374–377. ISSN 1094-2734. https://doi.org/10.1109/ICT.1999.843408
- [99] HASSAN, S. S., et al.: Temperature effects on the optical properties of bismuth nanoparticles prepared by PLAL for antibacterial activity. International Journal of Nanoelectronics and Materials. 2023, 16(1), 81–91. ISSN 1997-4434. http://dspace.unimap.edu.my/xmlui/handle/123456789/78122
- [100] WANG, Y., XIA, Y.: Bottom-Up and Top-Down Approaches to the Synthesis of Monodispersed Spherical Colloids of Low Melting-Point Metals. *Nano Letters*. 2004, 4(10), 2047–2050. ISSN1530-6992. https://doi.org/10.1021/nl048689j
- [101] CEITEC Nano. *Magnetron sputtering system BESTEC* [online]. [cit. 2024-02-27]. Available from: https://www.ceitec.eu/magnetron-sputtering-system-bestec/e1264
- [102] CEITEC Nano. Focused Ion Beam/Scanning Electron Microscope FEI Helios NanoLab 660 [cit. 2024-03-17]. Available from: https://www.ceitec.eu/focused-ion-beam-scanning-electron-microscope-fei-helios-nanolab-660/e1152
- [103] IAKOUBOVSKII, K., et al.: Mean free path of inelastic electron scattering in elemental solids and oxides using transmission electron microscopy: Atomic number dependent oscillatory behavior. *Physical Review B.* 2008, 77(10), 104102. ISSN 2469-9969. https://doi.org/10.1103/PhysRevB.77.104102

- [104] BAGLIN, J. E. E.: Ion beam nanoscale fabrication and lithography A review. *Applied Surface Scienece*. 2012, 258(9), 4103–4332. ISSN 0169-4332. https://doi.org/10.1016/j.apsusc.2011.11.074
- [105] HORÁK, M., ŠIKOLA, T. Influence of experimental conditions on localized surface plasmon resonances measurement by electron energy loss spectroscopy. *Ultramicroscopy*. 2020, 216, 113044. ISSN 0304-3991. https://doi.org/10.1016/j.ultramic.2020.113044
- [106] HOFFMAN, C. A., et al.: Semimetal-to-semiconductor transition in bismuth thin films. *Phys. Rev. B.* 1993, 48(15), 11431–11434. ISSN 2469-9969. https://doi.org/10.1103/PhysRevB.48.11431
- [107] CORNELIUS, T., TOIMIL-MOLARES, M. E.: Finite- and Quantum-Size Effects of Bismuth Nanowires. *Nanowires*. 2010, 414. ISBN 978-953-7619-79-4. http://dx.doi.org/10.5772/39516
- [108] BORAH, R., et al.: Plasmon resonance of gold and silver nanoparticle arrays in the Kretschmann (attenuated total reflectance) vs. direct incidence configuration. *Sci. Rep.* 2022, 12, 15738. ISSN 2045-2322. https://doi.org/10.1038/s41598-022-20117-7
- [109] ZOU, C. D., et al.: Melting and undercooling of bismuth nanocrystals by solvothermal synthesis. Physica B: Condensed Matter. 2009, 404(21), 4045–4050. ISSN 0921-4526. https://doi.org/10.1016/j.physb.2009.07.158
- [110] SHARMA, V., et al.: Shape separation of gold nanorods using centrifugation. *Proceedings of National Academy of Sciences USA*. 2009, 106(13), 4981–4985. ISSN 0027-8424. https://doi.org/10.1073/pnas.0800599106
- [111] SONG, T, et al.: A review of the role and mechanism of surfactants in the morphology control of metal nanoparticles. Nanoscale. 2021, 13(7), 3895–3910. ISSN 2040-3372. http://dx.doi.org/10.1039/D0NR07339C
- [112] ANSAR, S. M., et al.: Removal of molecular adsorbates on gold nanoparticles using sodium borohydride in water. *Nano letters*. 2013, 13(3), 1226–1229. ISSN 1530-6984. https://doi.org/10.1021/nl304703w
- [113] NALAJALA. N., et al.: Sodium borohydride treatment: a simple and effective process for the removal of stabilizer and capping agents from shape-controlled palladium nanoparticles. *Chemical Communication*. 2014, 50(66), 9365–9368. ISSN 1359-7345. http://dx.doi.org/10.1039/c4cc02747g
- [114] OSEGHALE, CH. I., et al.: Gold-based carbon-supported bimetallic catalysts for energy storage and biomedical applications. *Microchemical Journal*. 2019, 149. ISSN 0026-265X. https://doi.org/10.1016/j.microc.2019.05.018
- [115] HOYLE, D., et al.: UV Treatment of TEM/STEM Samples for Reduced Hydrocarbon Contamination. *Microscopy and Microanalysis*. 2011, 17(S2), 1026–1027. ISSN 1435-8115. https://doi.org/10.1017/S1431927611006003
- [116] ZHONG, R., et al.: Removal of Residual Polyvinylpyrrolidone (PVP) from Au Nanoparticles Immobilized in SiO₂ by Ultraviolet-Ozone Treatment. *ACS Applied Nano Materials*. 2019, 2(9), 5720–5729. ISSN 2574-0970. https://doi.org/10.1021/acsanm.9b01197

- [117] STÖGER-POLLACH, M.: Optical properties and bandgaps from low loss EELS: Pitfalls and solutions. *Micron.* 2008, 39(8), 1092–1110. ISSN 0968-4328. https://doi.org/10.1016/j.micron.2008.01.023
- [118] BORJA-URBY, R., et al.: Confined volume plasmon spatial distribution by low-loss EELS on self-assemble bismuth nanoparticles. *Journal of Electron Spectroscopy and Related Phenomena*. 2019, 237, 146891. ISSN 0368-2048. https://doi.org/10.1016/j.elspec.2019.146891

List of abbreviations

ABF annular bright field
ADF annular dark field

AFM atomic force microscopy

a-SNOM aperture scanning near field optical microscopy

BEM boundary element method

BF bright field

EBL electron beam lithography

EDX electron energy dispersive X-ray spectroscopy

EELS electron energy loss spectroscopy

EG ethylene glycol FIB focused ion beam

HAADF high angle annular dark field

LD longitudinal dipole

LDA longitudinal dipole antibonding

LME liquid metal embrittlement localised surface plasmon

LSPR localised surface plasmon resonance

LQ longitudinal quadrupole MA multimodal assembly

PVD physical vapour deposition

PVP polyvinylpyrrolidone

RMS Squared mean surface roughness

SE secondary electrons

SEM scanning electron microscopy

SNOM scanning near field optical microscopy

s-SNOM scattering scanning near field optical microscopy

SPP surface plasmon polariton

STEM scanning transmission electron microscopy

TD transverse dipole

TEG tetra ethylene glycol